Improving large-basin river routing using a differentiable Muskingum-Cunge model and physics-informed machine learning

Tadd Bindas[1], Wen-Ping Tsai[2], Jiangtao Liu[1], Farshid Rahmani[1], Dapeng Feng[1], Yuchen Bian[3], Kathryn Lawson[1], and Chaopeng Shen[1]
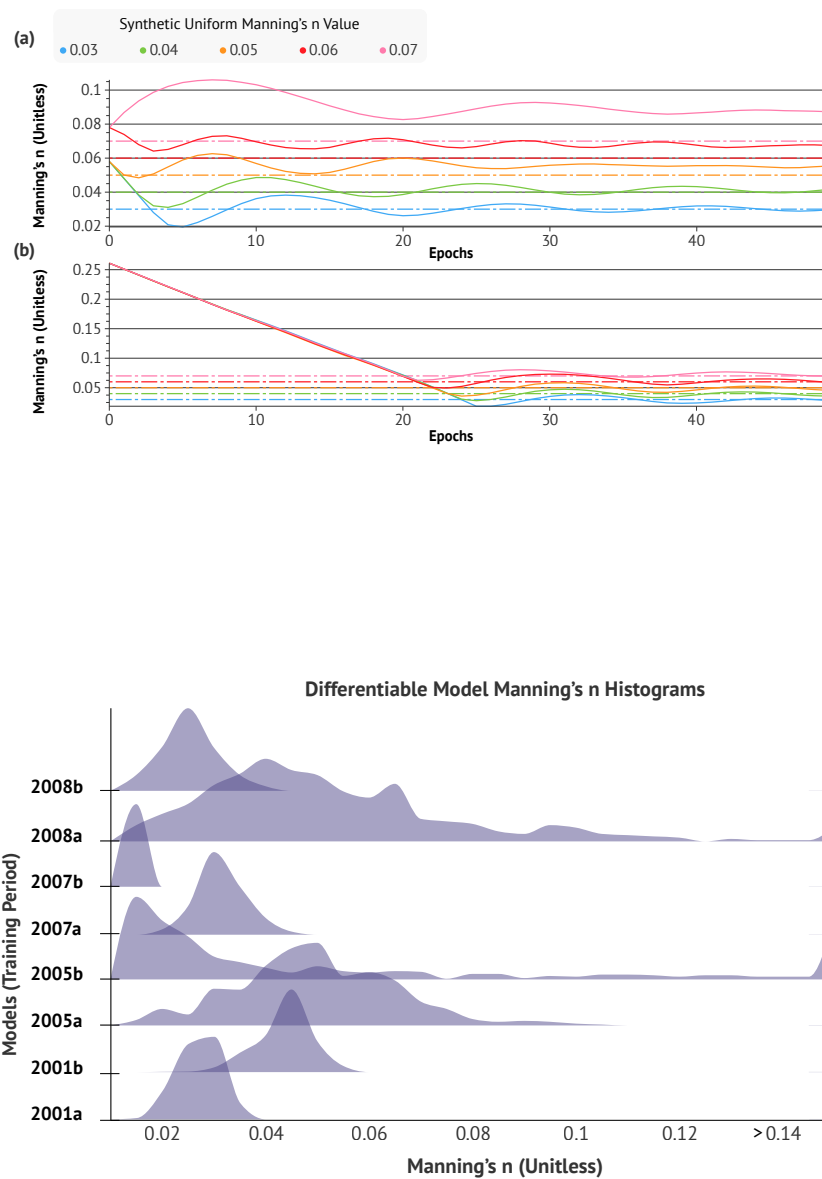
[1]Pennsylvania State University
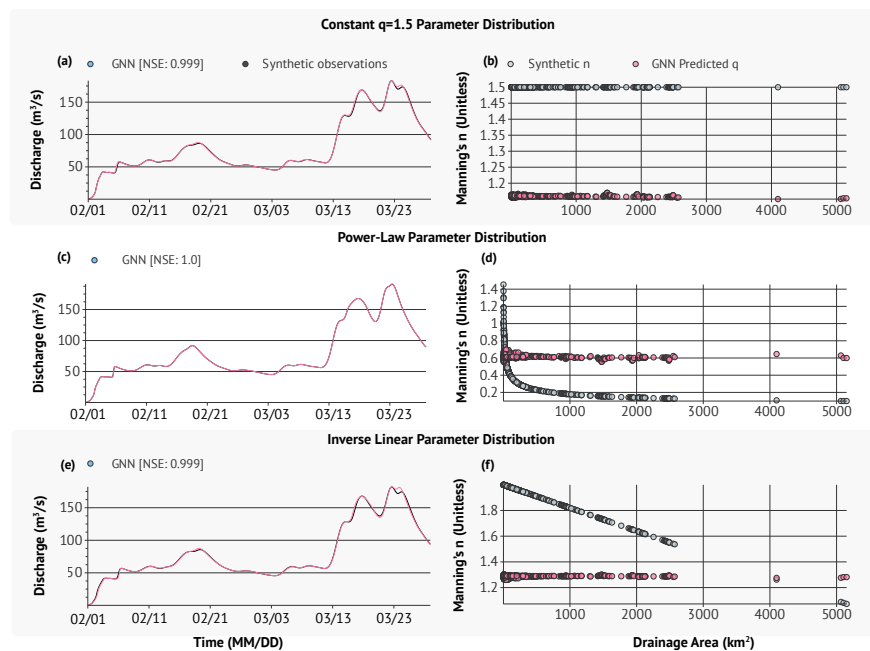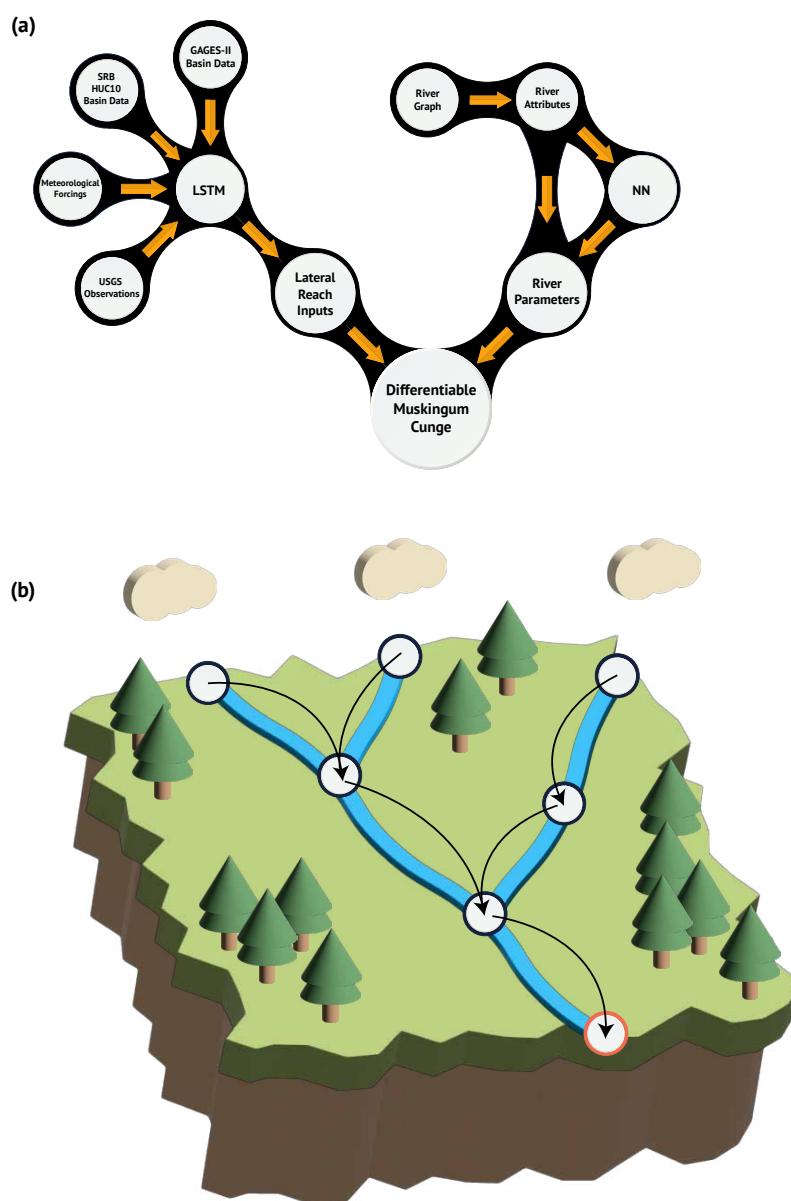[2]National Cheng Kung University
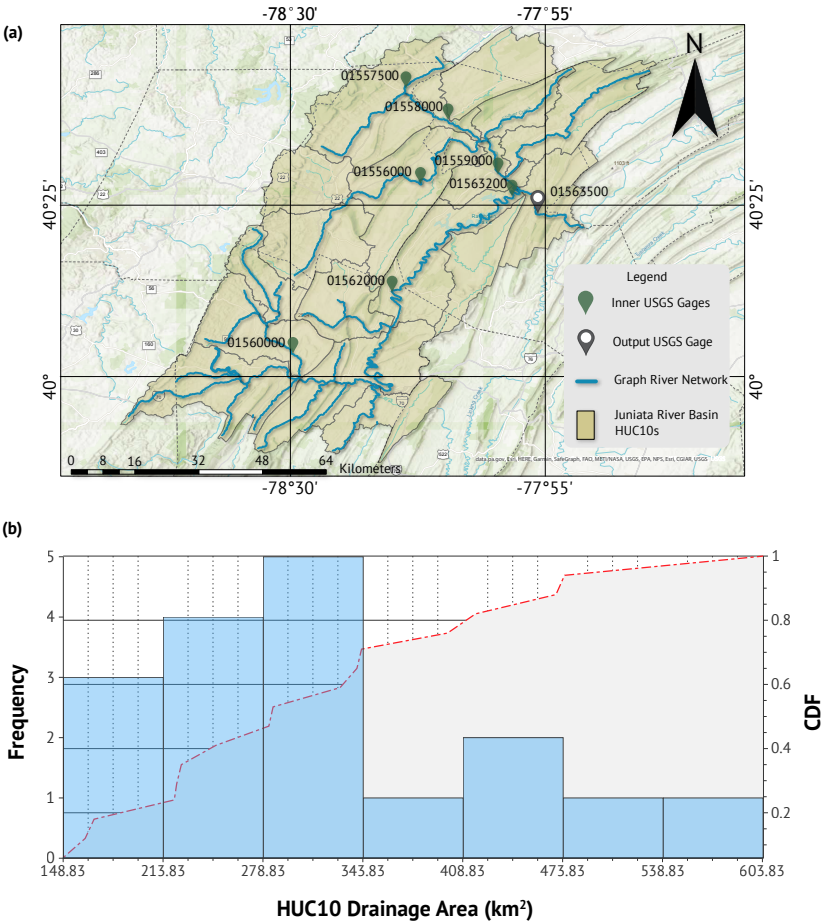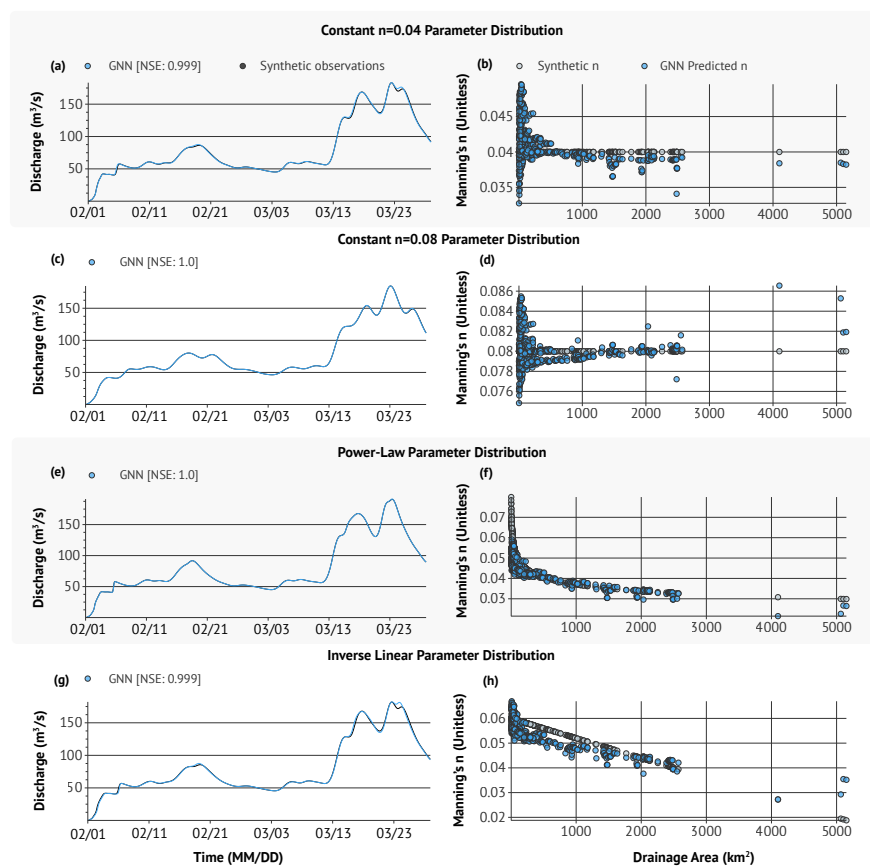[3]Amazon Search

May 25, 2023

Abstract

Recently, rainfall-runoff simulations in small headwater basins have been improved by methodological advances such as deep neural networks (NNs) and hybrid physics-NN models — particularly, a genre called differentiable modeling that intermingles NNs with physics to learn relationships between variables. However, hydrologic routing, necessary for simulating floods in stem rivers downstream of large heterogeneous basins, had not yet benefited from these advances and it was unclear if the routing process can be improved via coupled NNs. We present a novel differentiable routing model that mimics the classical Muskingum-Cunge routing model over a river network but embeds an NN to infer parameterizations for Manning's roughness (n) and channel geometries from raw reach-scale attributes like catchment areas and sinuosity. The NN was trained solely on downstream hydrographs. Synthetic experiments show that while the channel geometry parameter was unidentifiable, n can be identified with moderate precision. With real-world data, the trained differentiable routing model produced more accurate long-term routing results for both the training gage and untrained inner gages for larger subbasins ($>$2,000 km2) than either a machine learning model assuming homogeneity, or simply using the sum of runoff from subbasins. The n parameterization trained on short periods gave high performance in other periods, despite significant errors in runoff inputs. The learned n pattern was consistent with literature expectations, demonstrating the framework's potential for knowledge discovery, but the absolute values can vary depending on training periods. The trained n parameterization can be coupled with traditional models to improve national-scale flood simulations.

1

Differentiable Model Manning's n Histograms

(a)

(b)

(a)

(b)

Constant n=0.04 Parameter Distribution

(a) ○ GNN [NSE: 0.999] ● Synthetic observations

(b) ○ Synthetic n ● GNN Predicted n

Constant n=0.08 Parameter Distribution

(c) ○ GNN [NSE: 1.0]

(d)

Power-Law Parameter Distribution

(e) ○ GNN [NSE: 1.0]

(f)

Inverse Linear Parameter Distribution

(g) ○ GNN [NSE: 0.999]

(h)

Model Training

(a)

● Observations   ● GNN [NSE: 0.832]   ● Q` [NSE: 0.596]

Model Testing

(b)

● Observations   ● GNN [NSE: 0.856]   ● Q` [NSE: 0.756]

(a)

● River Segment

(b)

(a) 2005 and 2007 Model Training Periods

Testing Period Model Comparison

- Observations
- Model 2005b Percent Error
- Model 2007b Percent Error

(b) 2001 Period Comparison

- Model 2005b [NSE: 0.853]
- Model 2007b [NSE: 0.831]

(d) 2007 Period Comparison

- Model 2005b [NSE: 0.827]
- Model 2007b [NSE: 0.774]

(c) 2005 Period Comparison

- Model 2005b [NSE: 0.870]
- Model 2007b [NSE: 0.713]

(e) 2008 Period Comparison

- Model 2005b [NSE: 0.762]
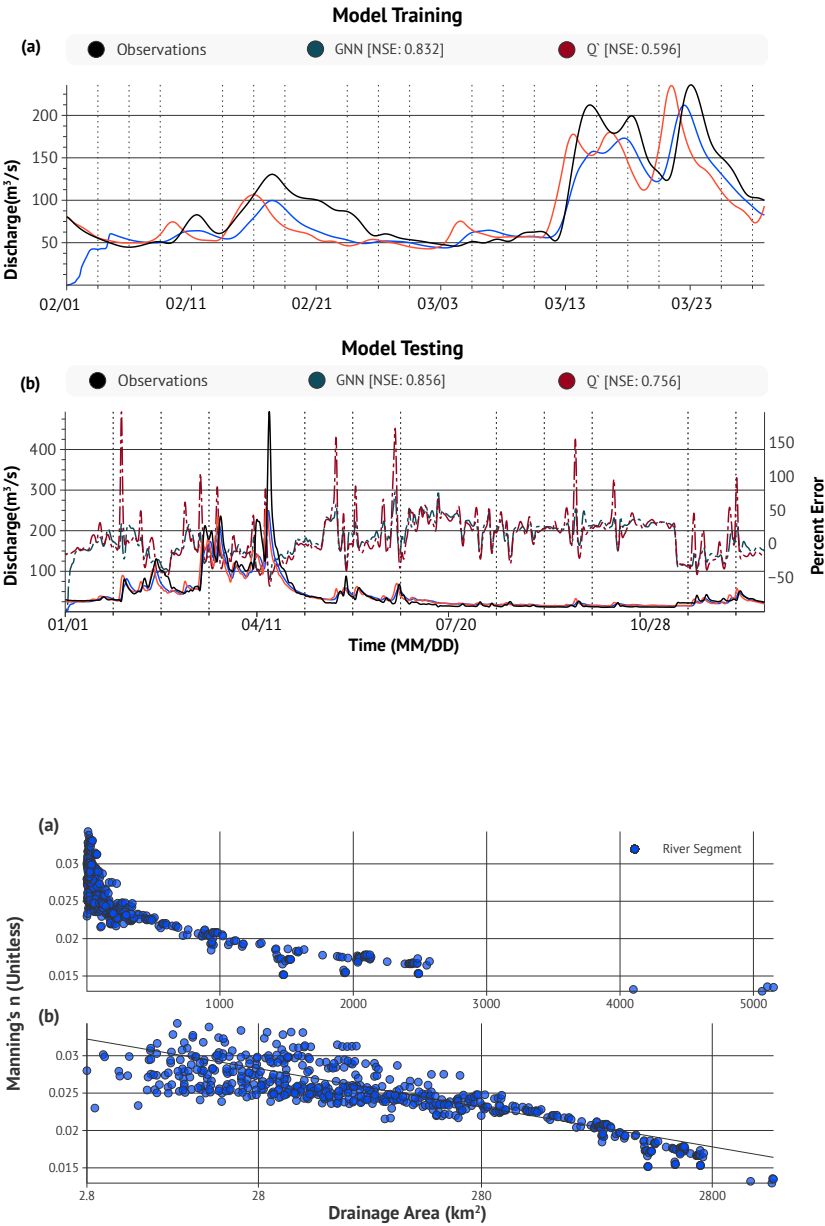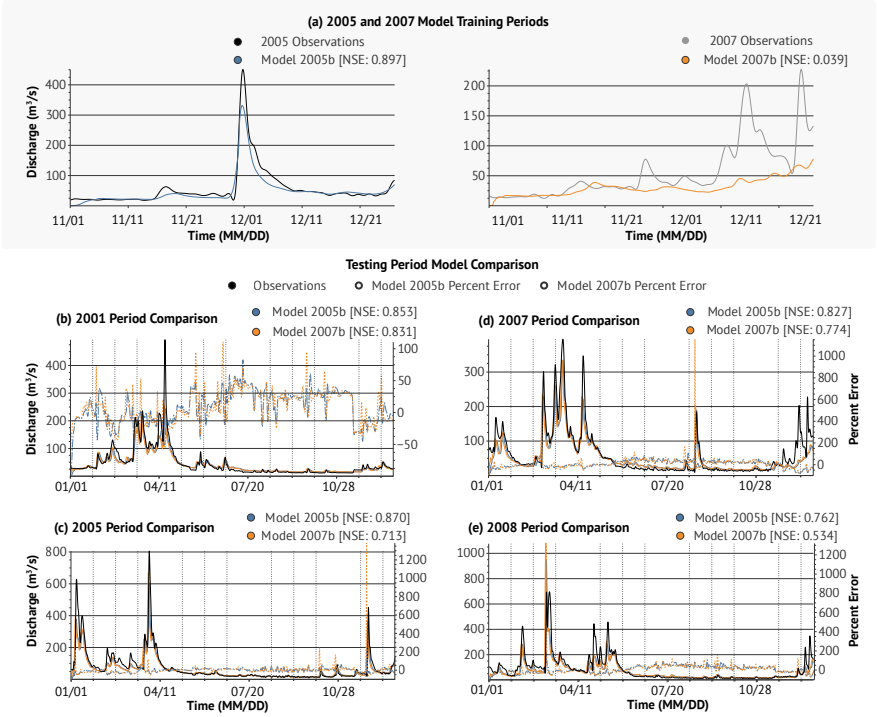- Model 2007b [NSE: 0.534]

Improving large-basin river routing using a differentiable Muskingum-Cunge model and physics-informed machine learning

Tadd Bindas[1], Wen-Ping Tsai[2], Jiangtao Liu[1], Farshid Rahmani[1], Dapeng Feng[1], Yuchen Bian[3], Kathryn Lawson[1], Chaopeng Shen*[,1]

[1] Civil and Environmental Engineering, The Pennsylvania State University, PA
[2] Hydraulic and Ocean Engineering, National Cheng Kung University, Tainan City
[3] Amazon Search, Palo Alto, CA

* Corresponding author: Chaopeng Shen, cshen@engr.psu.edu

Abstract

Recently, rainfall-runoff simulations in small headwater basins have been improved by methodological advances such as deep neural networks (NNs) and hybrid physics-NN models --- particularly, a genre called differentiable modeling that intermingles NNs with physics to learn relationships between variables. However, hydrologic routing, necessary for simulating floods in stem rivers downstream of large heterogeneous basins, had not yet benefited from these advances and it was unclear if the routing process can be improved via coupled NNs. We present a novel differentiable routing model that mimics the classical Muskingum-Cunge routing model over a river network but embeds an NN to infer parameterizations for Manning's roughness (n) and channel geometries from raw reach-scale attributes like catchment areas and sinuosity. The NN was trained solely on downstream hydrographs. Synthetic experiments show that while the channel geometry parameter was unidentifiable, n can be identified with moderate precision. With real-world data, the trained differentiable routing model produced more accurate long-term routing results for both the training gage and untrained inner gages for larger subbasins (>2,000 km^2) than either a machine learning model assuming homogeneity, or simply using the sum of runoff from subbasins. The n parameterization trained on short periods gave high performance in other periods, despite significant errors in runoff inputs. The learned n pattern was consistent with literature expectations, demonstrating the framework's potential for knowledge discovery, but the absolute values can vary depending on training periods. The trained n parameterization can be coupled with traditional models to improve national-scale flood simulations.

Main points:
1. A novel differentiable routing model can learn effective river routing parameterization, recovering channel roughness in synthetic runs.
2. With short periods of real training data, we can improve streamflow in large rivers compared to models not considering routing.
3. For basins >2,000 km^2, our framework outperformed deep learning models that assume homogeneity, despite bias in the runoff forcings.

41   **1. Introduction**

42

43   Riverine floods pose a major risk to human safety and infrastructure (Douben, 2006; François et al.,

44   2019; International Panel on Climate Change (IPCC), 2012; Koks & Thissen, 2016) and are linked to

45   stream channel characteristics. Riverine floods along large stem rivers occur when the peak flow rate

46   exceeds the stem river conveyance capacity. The timing of flood convergence and peak flood rates are

47   influenced by the channel's geometries and flow resistance properties (Candela et al., 2005; Kalyanapu

48   et al., 2009). In recent years, we have witnessed many deadly riverine floods, e.g., in the Mississippi

49   River, USA (Rice, 2019) and India (France-Presse, 2022), with such disasters expected to rise significantly

50   based on future climate projections (Dottori et al., 2018; Prein et al., 2017; Winsemius et al., 2016). The

51   ability to better account for flood convergence and streamflow processes is urgently needed to help us

52   better inform society of stem river flood magnitudes and timing.

53

54   In hydrologic modeling, routing describes how the stream network conveys runoff downstream while

55   accounting for mass balances and the speed of flood wave propagation (Mays, 2010). Most routing

56   models are based on the principle of continuity (or mass conservation) but they differ in how the

57   momentum equation or flow velocity is calculated. For example, the widely-applied Muskingum-Cunge

58   (MC) (Cunge, 1969) routing method is a center-in-space center-in-time finite difference solution to the

59   continuity equation, assuming a prismatic flood wave as the constitutive relationship to simplify the

60   momentum equation. In some other cases, the momentum equation is solved in conjunction with the

61   continuity equation (Ji et al., 2019) with a range of simplifying assumptions, e.g., ignoring inertia (Shen &

62   Phanikumar, 2010), ignoring both inertia and pressure gradient (only slope remaining) (Mizukami et al.,

63   2016), or including additional formulations to handle effects of scale, e.g., Li et al. (2013). In each case,

64   these models have parameters that need to be determined from lookup tables or calibration, e.g.,

65   roughness parameters that serve as resistance to flow.

66

67   Although routing parameters often rank among the important ones for discharge simulation (Khorashadi

68   Zadeh et al., 2017; L. Liu et al., 2022), they been difficult to parameterize at large scales, especially in a

69   way to both sensibly represent basin-internal spatial heterogeneity and adapt to discharge data. Using

70   traditional roughness values tabulated for various land covers (Arcement & Schneider, 1989) requires in-

71   situ scouting, e.g., to determine if channels have pools, weeds, grass, etc., which is currently impractical

72   for large-scale applications. Many calibration exercises (Khorashadi Zadeh et al., 2017; L. Liu et al., 2022;

73   Mizukami et al., 2016) have used only one set of parameters for an entire basin, neglecting fine-scale

74   spatial heterogeneity in river-reach characteristics. Some studies have employed Manning's roughness,

75   *n* (a coefficient representing a channel's resistance to flow), as a linear function of river depth or other

76   characteristics (Getirana et al., 2012; H.-Y. Li et al., 2022), but it is unclear if these relationships

77   accurately represent the available data.

78

79   While the accuracy of basin rainfall-runoff models has improved substantially in recent years with

80   machine learning (ML) (Adnan et al., 2021; Feng et al., 2020; Kratzert et al., 2019; Sun et al., 2022; Xiang

81   et al., 2020), these methods have not been applied to routing modules in order to benefit the simulation

82   of stem river floods. Neural networks (NNs) like long short-term memory (LSTM), GraphWaveNet (Sun et

83   al., 2021), or convolutional networks (Duan et al., 2020) have demonstrated their prowess in learning

84   hydrologic dynamics from big data. They are applicable not only to streamflow hydrology but also to

85   variables across the entire hydrologic cycle (Shen, Chen, et al., 2021; Shen & Lawson, 2021) such as soil

86   moisture (Fang et al., 2017, 2019; J. Liu et al., 2022; O & Orth, 2021), groundwater (Wunsch et al., 2022),

87   snow (Meyal et al., 2020), longwave radiation (Zhu et al., 2021), and water quality parameters like water

88   temperature, dissolved oxygen and nitrogen (He et al., 2022; Hrnjica et al., 2021; Lin et al., 2022;

89   Rahmani, Lawson, et al., 2021; Saha et al., 2023; Zhi et al., 2021). However, these approaches are mostly

90   suitable for relatively homogeneous headwater basins; spatial heterogeneities in forcings and basin

91   characteristics are generally not well represented in these approaches. In our previous studies we

92   observed that large basins often turned out to have poorer performance for LSTM models. The routing

93   module is the key component that allows us to consider how runoff from heterogeneous subbasins

94   converge and contribute to the stem river floods, and could be extended to support reactive transport

95   modeling in the river network.

96

97   A recent development in integrating ML with physical understanding is the use of differentiable, physics-

98   informed machine learning models, which can approach the performance of purely data-driven ML

99   models but also provide interpretable fluxes and states (Feng, Liu, et al., 2022). "Differentiable" models

100   can rapidly and accurately compute the gradients of the model outputs with respect to any input,

101   enabling the combined training of NNs to approximate complex or unknown functions from big data

102   while keeping physical priors. Such models can be simply supported by automatic differentiation (AD),

103   which tracks each elementary operation of tensors through the use of a computational graph, then uses

104   derivative rules to compute the gradient of each tensor operation (Baydin et al., 2018). This enables

105 hybrid frameworks to learn and incorporate complex and potentially unknown functions from big data

106 while retaining physical formulations. By connecting deep networks to reimplemented process-based

107 models (or their NN surrogates), Tsai et al. (2021) developed a NN-based parameterization pipeline that

108 infers physical parameters for process-based models. Differentiable models can also extrapolate better

109 in space and time than purely data-driven deep networks (Feng, Beck, et al., 2022). These methods are

110 also applicable to estimating parameters in ecosystem modeling (Aboelyazeed et al., 2022), and allow us

111 to flexibly discover variable relationships within the model based on big data, enabling improved

112 transparency compared to standard deep learning models.

113

114 Nevertheless, it was unclear if differentiable modeling could effectively learn relationships in a highly

115 complex river network, which convolves and integrates processes over large scales and thus render

116 small-scale processes unidentifiable. The river network forms a hierarchical graph, which is not unlike

117 the graph networks for applications like social recommendations (Fan et al., 2019), but with a

118 predefined spatial topology (due to a fixed river network) and a converging cascade. A complex river

119 graph can have many nodes, which, when coupled with many time steps, could potentially lead to a

120 training issue known as the vanishing gradient (Hochreiter, 1998), where the gradients with respect to

121 the parameters are vanishingly small and the system becomes very difficult to train. Moreover, runoff

122 data (required as an input for routing) are generally not available seamlessly for all subbasins and must

123 be estimated by models, but models for runoff could incur substantial errors. It was unclear if the

124 routing parameters could be learned, given such errors. It was further unclear if downstream discharge

125 data alone has enough information to enable learning of reach-scale relationships. In other words, a

126 reach-scale relationship may or may not be identifiable using downstream observations which integrate

127 the signals from the entire catchment area.

128

129 In this work, we developed a novel differentiable modeling framework to perform routing and to learn a

130 "parameterization scheme" (a systematic way of inferring parameters from more rudimentary

131 information) for routing flows on the river network. Such a physically-based routing method has never

132 been combined with NNs before. A NN-based parameterization scheme for Manning's n and river

133 bathymetry shape (q) is integrated with MC routing and is applied throughout the river network to

134 provide improved understanding of both the model and the modeled system. We designed synthetic

135 and real data experiments to answer the following research questions:

136　　　　1.　*Given substantial errors with estimated runoff as inputs to the routing module, can we learn*

137　　　　　　*effective routing parameterization schemes that can produce reliable results for long-term*

138　　　　　　*simulations in large river networks?*

139　　　　2.　*Does the learned parameterization perform well for both trained and untrained internal gages*

140　　　　　　*and how does the performance vary as a function of basin area?*

141　　　　3.　*Do short periods of downstream discharge contain sufficient information to train a reliable*

142　　　　　　*parameterization scheme or to identify the parameterization for channel roughness and*

143　　　　　　*hydraulic geometries?*

144

145　　**2. Data and Methods**

146　　*2.1 Overview*

147　　As an overview, we describe a differentiable model that routes runoff through a river network (or

148　　"graph" in the ML terminology) similar to the traditional Muskingum-Cunge (MC) method. But unlike the

149　　traditional MC, our differentiable model is able to incorporate and train neural networks to provide

150　　reach-scale parameterization. This new routing model can be perceived as a physics-informed graph

151　　neural network (GNN) from an ML perspective. The nodes of the graph are spaced ~2000 m apart to

152　　ensure stability. We trained an embedded a Multilayer Perceptron (MLP) NN to generate spatially-

153　　distributed river parameters for each reach (or "edge" in the GNN terminology) in the river network

154　　(Figure 1b). The loss function (the model's goal is to minimize the output of this) was calculated at the

155　　furthest downstream node of the graph. To disentangle rainfall-runoff (required information for routing)

156　　from the routing processes, lateral inflow of combined overland and groundwater flow was obtained

157　　from a pre-trained LSTM streamflow prediction model (reported in previous work). The runoff values

158　　were then disaggregated to hourly time steps via interpolation and routed throughout the river network

159　　using the proposed differentiable routing model (Figure 1a). We provide the details in the subsections

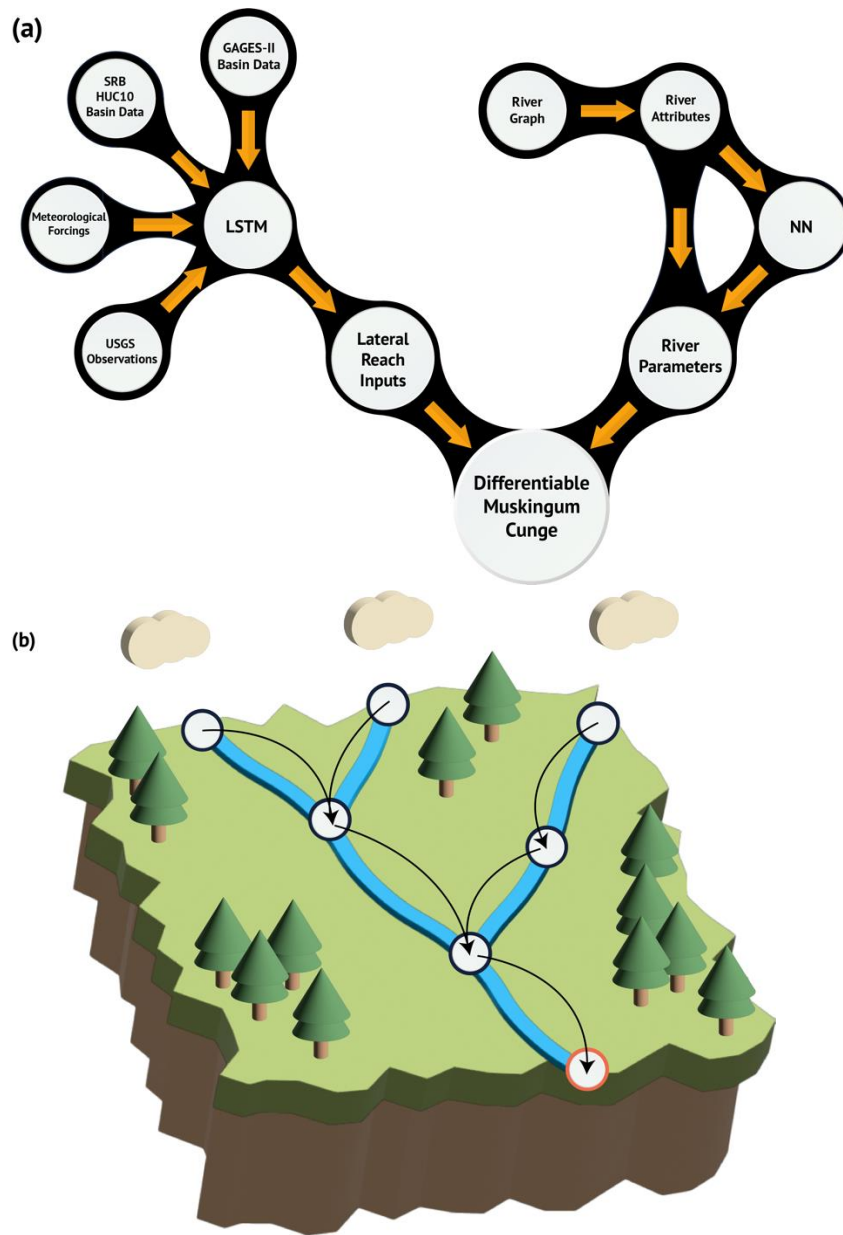160　　that follow.

161

162

163
164

Figure 1: (a) An abstract overview of how inputs move through our workflow to eventually be run

through the differentiable MC function. MC utilizes lateral flow inputs based on LSTM predictions, NN

predicted river parameters n and q, and other river attributes to generate predictions. (b) An illustration

of how we traverse the graph (dark blue circles) using MC to make a discharge prediction for the final

node (orange circle).

170

171   *2.2 The River Graph*

172   We constructed a river network (or graph) for the Juniata River Basin (JRB) in the northeastern United

173   States (Figure 2), by processing the United States Geological Survey's (USGS's) National Hydrography

174   Dataset (NHDplus v2) (HorizonSystems, 2016; Moore & Dewald, 2016) which provide topology and some

175   attributes of the river reaches such as upstream catchment area. We ensured stability of the MC scheme

176   by discretizing the river network into approximately 2-km reaches, resulting in 544 junction points (or

177   nodes) and 582 river reaches (or edges). These reaches are where the physical parameters like

178   Manning's roughness and channel shape coefficients are defined. To reduce computational demand, we

179   selected a subset of NHDplus v2 river reaches based on a stream density threshold (total stream

180   length/watershed area), choosing rivers with the longest length until a stream density of 0.2 km/km^2

181   was reached. We then calculated slope and sinuosity for the reaches by overlaying NHDplus v2 with 10-

182   m resolution digital elevation data (USGS ScienceBase-Catalog, 2022). Prior work describes the bulk of

183   the extraction procedure that prepares input data for a physically-based surface-subsurface processes

184   model (Ji et al., 2019; Shen et al., 2013, 2014, 2016; Shen & Phanikumar, 2010).

185

186   The hydrograph at the furthest downstream JRB gage, USGS gage 01563500 (node 4809 in our graph) on

187   the Juniata River at Mapleton Depot, PA, was chosen as the training target (Figure 2a). This gage has a

188   catchment area of 5,212 km^2 contributed from the 582 simulated reaches upstream. Seven USGS gages

189   are located upstream of this node which enables further validation of the simulations.
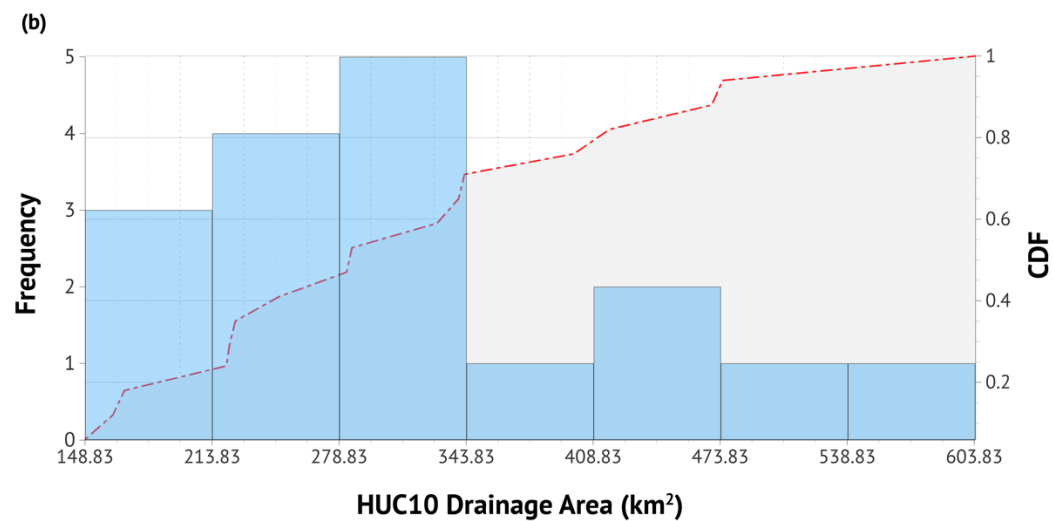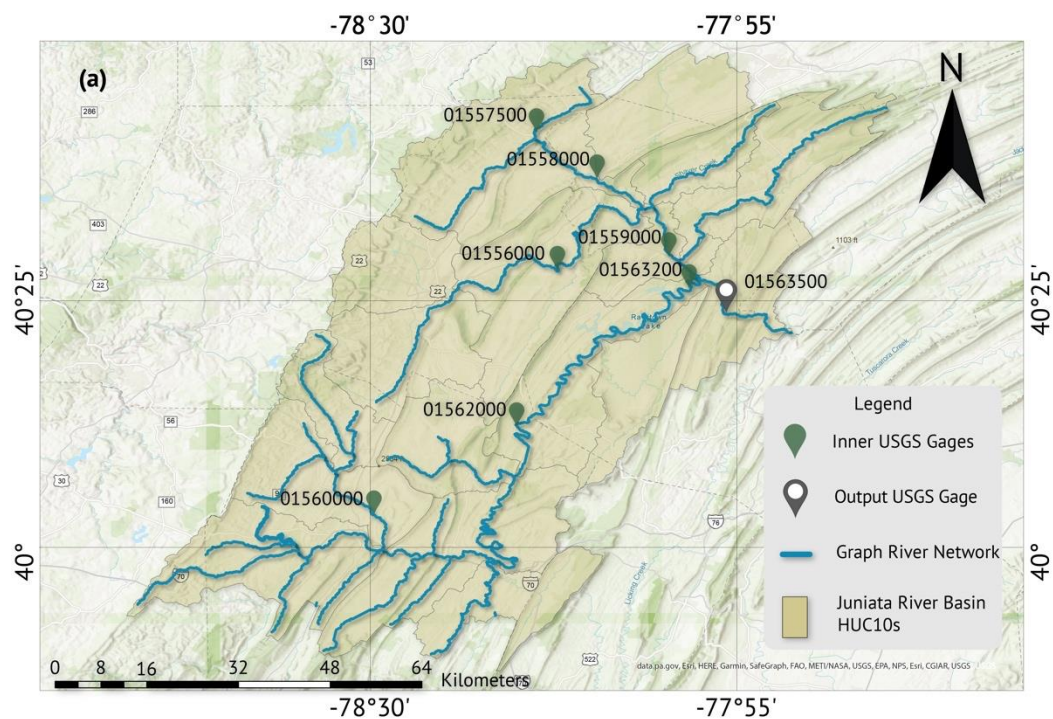
190

191

192
193
194
195 *Figure 2: (a) A map of the Juniata River Basin's (JRB's) river network and HUC10 watersheds. Each eight-*
196 *digit number corresponds to a USGS gage. (b) A histogram showing the distribution of HUC10*
197 *watersheds in the JRB. The x-axis shows the distribution of the HUC10 watershed area in square*
198 *kilometers. The left y-axis shows the number of HUC10s that fall within the area ranges (corresponding*
199 *with the blue bars), and the right y-axis shows a cumulative density function (CDF) distribution of the*
200 *areas, corresponding with the red dashed line.*
201

202 *2.3 Implementing River Routing with Muskingum-Cunge*

203 *2.3.1 Muskingum-Cunge*

204 The Muskingum-Cunge (MC) method is a widely-used flood routing technique that combines the

205 Muskingum storage routing concept with the continuity and momentum equation for a river reach

206 (Cunge, 1969), solved using a center-in-space, center-in-time finite difference scheme for each reach, at

207 time steps *t* and *t+1:*

$$Q_{t+1} = c_1 I_{t+1} + c_2 I_t + c_3 Q_t + c_4 Q' \tag{1}$$

$$c_1 = \frac{\Delta t - 2KX}{2K(1-X) + \Delta t} \tag{2}$$

$$c_2 = \frac{\Delta t + 2KX}{2K(1-X) + \Delta t} \tag{3}$$

$$c_3 = \frac{2K(1-X) - \Delta t}{2K(1-X) + \Delta t} \tag{4}$$

$$c_4 = \frac{2\Delta t}{2K(1-X) + \Delta t} \tag{5}$$

208 Where I_t and Q_t are the inflow and outflow of the reach at time step t, respectively, and I_{t+1} and Q_{t+1}

209 are the inflow and outflow at the next time step, *t+1*. *K* represents travel time based on reach length

210 and wave celerity, *X* is a dimensionless inflow/outflow weighing parameter, and *Q'* represents lateral

211 inflow of the incremental catchment area of the reach, and can also include tributary inflows. We

212 adopted the simple linear form of the Muskingum equation: X is constant and K= $\Delta x / v$ where Δx is

213 length of the reach and v is the discharge velocity (m/s) of the current time step. More complex

214 nonlinear forms of the MC equation could be tested in the future (Mays, 2019). To simulate a river

215 network, we divide the network into a series of reaches to route the flow of water from upstream to

216 downstream. The outflow from a reach is the inflow of the next downstream reach.

217

218 *2.3.2 MC parameter values and variable channel dimensions*

219 To implement MC, we chose an hourly time step (*Δt*) and a weighing coefficient (*X)* of 0.3, which was

220 based on regional expectations, for Equations 2-5. Since discharge velocity *v* and stream top width *w*

221 vary over time, they need to be updated in each time step with respect to discharge Q, which was done

222 here with the help of a constitutive relationship used to close the equations. For this, because at-a-site

223 hydraulic geometries (Gleason, 2015; Leopold & Maddock, 1953) leads to a power-law relation between

224 top width (w [m]) and depth (d [m]), we can assume such a relationship:

$$w = pd^q \qquad (6)$$

225 where p [m] and q [-] are linear and exponential parameters, respectively, that are potentially spatially

226 heterogeneous and represent the shape of the channel's cross-sectional area. For a rectangular channel,

227 q=0, and for a triangular channel, q=1. The cross-sectional area A_{CS} is the integral of w with respect to d

228 (Equation 7). To simplify the task (and because it is not sensitive based on our observations), we

229 assumed p=21 based on preliminary data fitting to USGS hydraulic geometries from field surveys of

230 gages in the JRB. Note that even though we make this assumption here for model completeness, we do

231 not posit that q is invertible from available data because it may not be that significant for the

232 downstream discharge. Moving forward with these assumptions, we can write these relationships as

233 Equation 7:

$$A_{CS} = \int_0^d w \, \partial d = \int_0^d pd^q \, \partial d = \frac{pd^{q+1}}{q+1} \qquad (7)$$

234 Combining Equation 7 with Manning's n Equation, we come up with Equation 8a. Reorganizing, we

235 derive a function that estimates d from Q (Equation 8b). With d, p, and q, we can estimate v and K using

236 the linear form of Muskingum equation as in Equations 7, 8c, and 8d which close the equations.

$$Q = vA_{CS} = \frac{1}{n}R^{2/3}S_0^{\frac{1}{2}}\frac{pd^{q+1}}{q+1} = \frac{pd^{q+\frac{5}{3}}S_0^{\frac{1}{2}}}{n(q+1)} \qquad (8a)$$

$$d = \left[\frac{Q_t n(q+1)}{pS_0^{\frac{1}{2}}}\right]^{\frac{3}{5+3q}} \qquad (8b)$$

$$v = \frac{Q_t}{A_{CS}} \qquad (8c)$$

$$K = \frac{\Delta x}{v} \qquad (8d)$$

237 Here, S_0 represents the reach slope, Q_t represents the discharge exiting the reach at time t, and Δx is

238 the reach length.

239

240 *2.3.3 Differentiable modeling*

241   By implementing MC on a differentiable coding platform (PyTorch, Tensorflow, Julia, etc.), we can train a

242   coupled NN in an "online" way to produce physical reach-scale river parameters for the routing model,

243   much like our earlier work in differentiable parameter learning (dPL) (Tsai et al., 2021). Here we include

244   a NN into the MC routing framework to optimize equation parameters based on big data while

245   maintaining physical consistency and mass balances. In this case, a Multilayer Perceptron (MLP) (Leshno

246   et al., 1993) is incorporated. The MLP, featuring two hidden layers and a sigmoid activation function in

247   the output layer, accepts a normalized array of attributes (c) for each reach (Table A2). Based on initial

248   results, we saw no need to add further complexity (additional hidden layers). The network then outputs

249   the Manning's roughness coefficient (n) and channel bathymetry shape coefficient (q):

$$n, q = NN(c) \tag{9}$$

250   where n represents a channel's resistance to flow and q represents the shape of the channel's cross-

251   sectional area. These parameters are inferred for each reach using the attributes of that reach prior to

252   routing, since we assumed n and q to be time-invariant. This produces r number of n and q values

253   specific to each reach for all timesteps where r is the number of river reaches. The weights of the MLP

254   are updated using backpropagation and the Adam optimizer (Kingma & Ba, 2017).

255

256   *2.4 Lateral streamflow inputs*

257   Since spatially-distributed runoff is needed to predict runoff in downstream basins, but there is no such

258   data, we employed a pretrained LSTM (Hochreiter & Schmidhuber, 1997) rainfall-runoff model. This

259   LSTM model was similar to those developed and reported in previous streamflow and water quality

260   studies (Feng et al., 2020; Ouyang et al., 2021; Rahmani, Lawson, et al., 2021; Rahmani, Shen, et al.,

261   2021), and we refer the reader to these publications for a more detailed description of these models.

262   After the initial training was done, we chose not to further update the LSTM in order to disentangle the

263   rainfall-runoff and routing parts of the modeling process, testing the robustness of the methodology in

264   the face of errors with simulated runoff. In addition, the test could tell us if other rainfall-runoff models

265   could be used instead. Updating LSTM further could lead to its co-adaptation with the routing module,

266   making the procedure complex.

267

268   To briefly summarize, the LSTM model used a combination of basin-averaged attributes, daily

269   meteorological forcings, and volumetric streamflow observations as inputs, and output daily basin

270   discharge. Meteorological forcings (total annual precipitation, downward long-wave radiation flux,

271 downward short-wave radiation flux, pressure, temperature) were obtained from the NASA NLDAS-2

272 Forcing Data set (Xia et al., 2009, 2012). We selected 29 basin attributes (Table A1 in the Appendix)

273 similar to those chosen in previous LSTM studies (Ouyang et al., 2021). Consistent with Ouyang et al.

274 (2021), we focused on training the LSTM on 3213 gages selected from the USGS Geospatial Attributes of

275 Gages for Evaluating Streamflow II (GAGES-II) dataset (Falcone, 2011) with input data between

276 1990/01/01 - 1999/12/31. We developed the workflow to obtain forcing data and inputs seamlessly for

277 any small basin in the conterminous United States (CONUS). In this case, we extracted data from HUC8

278 subbasins and HUC10 watersheds to gather inputs to train our LSTM model and predict discharge,

279 respectively.

280

281 When evaluated on the gaging stations in the study area, the model achieved a median daily Nash-

282 Sutcliffe Efficiency (NSE) (Nash & Sutcliffe, 1970) of 0.7849 for the eight gauging stations in the JRB.

283 After training during the period of 1990/01/01 – 1999/12/31, the model was run from 2000/01/01-

284 2009/12/31 to predict discharge for the 17 HUC10 watersheds in the study area:

$$Q' = LSTM(x_{HUC10}, A_{HUC10}) \tag{10}$$

285 where Q' [m^3/s] is the daily runoff for the HUC10 basin, and x_{HUC10} and A_{HUC10} are HUC10-averaged

286 atmospheric forcings and static attribute variables, respectively. Lastly, we computed a mass transfer

287 matrix, which tabulates the fraction of a subbasin draining into a river reach. Each row of the matrix is

288 obtained by dividing the incremental catchment area of reaches inside a subbasin by the total area of

289 that subbasin. Runoff can be distributed to river reaches via a simple matrix multiplication.

290

291 Due to the nature of the data used to train the LSTM, it could produce seamless (having no gaps) runoff

292 estimates for the JRB but only on a daily, not hourly, scale. Because MC routing needs to operate on

293 smaller time steps, we quadratically interpolated (Virtanen et al., 2020) daily data into hourly time steps,

294 where each daily measurement occurs at 12:00 hours. For training and evaluating the routing model, we

295 collected observed discharge data for nodes intersecting USGS GAGES-II monitoring stations. Only some

296 time periods of the most downstream gage station were used for training, and other stations were only

297 used for evaluation. The observed discharge data were similarly disaggregated to hourly data.

298

2.5 Inverse-routing and hyperparameters

There are time zone differences between the forcing data (recorded using UTC) and USGS streamflow
(recorded in UTC-5). To address this, we first shifted the LSTM-produced runoff outputs by 5 hours.
Because LSTM was trained to predict runoff at the outlet of a basin, with catchment area being an
impactful input to the model, it already implicitly considers the time of concentration to the outlet.
However, as our modeled river network extends into the subbasins and contains smaller rivers, the
routing module explicitly simulates the within-basin concentration process. Ideally, we can use an
inverse-routing approach to revert LSTM-predicted runoff to the time before it enters the river network.
However, as inverse-routing methods (Pan & Wood, 2013) can be quite involved and were not the focus
of the study, we opted for a simple approach that shifted the runoff back in time by τ hours. τ is
considered a hyperparameter. To avoid overfitting, we used the same τ value for all the subbasins and
all experiments, and determined this value by manually tuning based on the training period. We found
$\tau = 9$ (hours) to be a good choice. More complicated procedures could be employed in the future, but
this straightforward approach proved to be effective in our case.

Hyperparameters and training period sizes for our differentiable routing model were chosen through
repetitive trial and error based on the training period. These trials led us to choose a hidden size of 6 for
our MLP, and a training size of eight weeks. Parameters were tuned for 50 epochs for synthetic and real
data experiments. Mean Squared Error (MSE) was chosen as our loss function. Since our differentiable
model at t=0 assumes no inflow to the river network and relies exclusively on Q' for flow inputs, a period
of 72 hours is employed to "warm up" the model states in the river network, and the loss function and
NSE are not calculated within this period.

2.6 Experiments

2.6.1 Synthetic Parameter Recovery

We first ran multiple synthetic parameter recovery experiments to check if the dataset and the
framework could indeed recover assumed relationships with small training periods of eight weeks. Our
first experiment tested if we could correctly recover a single, spatially-constant set of assumed values
for both *n* and *q* for the whole river network, resulting in only two degrees of freedom. We assumed
ranges from $0.01 - 0.3$ and 0-3 for the synthetic values of *n* and *q*, respectively, to give a realistic value
range for the MLP to learn parameters. *n* and *q* model parameters were initialized to be at the 90th and
20th percentiles for the first and second set of synthetic experiments, respectfully.

13

331

In our second experiment, we assumed constant *n* throughout the reaches but set the trained model as

n,q = NN(c) (Equation 9) so that the *n, q* values could be different from reach to reach. In this case,

ideally, the NN would learn to output a constant value regardless of the inputs.

335

Our third synthetic experiment examined if we could retrieve simple assumed relationships within

realistic literature bounds (inverse-linear or power-law) [Equation 9-10] between *n, q,* and drainage area

(DA), given that the MLP had far more inputs than just DA. The trained model is still utilizing Equation 9,

as we assumed we did not know the functional relationship *a priori.*

$$n = 0.06 - 8 \times 10^{-6}(DA) \tag{11}$$
$$q = 2 - 0.00018(DA)$$

$$n = \frac{0.0915}{(DA)^{0.131}} \tag{12}$$
$$q = \frac{2.1}{(DA)^{0.357}}$$

2.6.2 Observational Data Experiments.

We trained our differentiable model (updating the weights in NN as in equation 6) against observed

USGS data. We utilized eight-week training periods from different years and checked whether the

resulting parameters led to satisfactory routing in other years at both the training gage and untrained,

inner, gages. Training periods were selected based on times when the LSTM had high accuracy and when

there were frequent discharge peaks. Routing frequently fluctuating discharge through a river network

introduces more variance into the MLP, allowing it to perform better when testing over a longer time

period. Additionally, high LSTM accuracy reduces the noise --- we hypothesize the system has some

tolerance to the runoff errors but outsized errors can invalidate the model. Periods of such "high

flashiness" in the JRB occurred during both 02/01-03/29 and 11/01-12/26, while the years 2001, 2005,

2007, and 2008 had high LSTM accuracy, giving us eight time periods on which to train NN models. We

then trained the differentiable routing models on all eight selected time periods to determine the

sensitivity of the model performance to the selected training time period.

353

When interpreting model performance at inner gages, we compared results with the LSTM that modeled

the whole JRB as a uniform basin and a simple summation of the τ-shifted LSTM runoff inputs (Q'). We

also explored whether using a combination of inner gages, along with the furthest downstream gage,

14

357   inside of the loss function would improve model performance on all gages throughout the study area.

358   The gages used were USGS 01560000 (edge 1053) and 01563200 (edge 2689). Internal gages were

359   selected based on NSE metrics when using only the furthest-downstream gage in the loss calculation; we

360   chose basins with middle-level metrics so as to not overfit the model if using highly predictive internal

361   gages.

362

363   **3. Results and Discussion**

364   In the following, we first discuss our synthetic experiments (Section 3.1) which explore our routing

365   framework's potential to retrieve assumed parameters from our differentiable GNN. Next, we show the

366   results of confronting our model with LSTM-simulated runoff as observed streamflow at the furthest

367   downstream gage, expanding the training period to other time ranges, then applying our models to

368   different years for observation (Section 3.2). Furthermore, we discuss the stability of our trained models

369   over several years of testing (Section 3.3). Lastly, we analyze the n parameters recovered for the trained

370   models and discuss their implications (Section 3.4).

371

372   *3.1 Synthetic experiments*

373   Our first synthetic experiment (with constant parameters and only 2 degrees of freedom for the search)

374   recovered the assumed n values with moderate accuracy, but not the channel geometry parameter q

375   (Table 1). Recovered n values were within a small range of the assumed ones, with minor fluctuations,

376   while recovered q values mostly stayed similar the initial guesses, showing slight changes after a number

377   of iterations. This result was consistent across 10 runs, each with different "synthetic truth" values for n

378   and q. The training led n to the assumed values rapidly, typically within 20 epochs (Figure A1). The non-

379   identifiability of q was likely because q has only a small influence on the storage capacity of the stream

380   and the simulated discharge is not sensitive to q, making dL/dq (where L is the loss function) negligible.

381   While it is a pity that hydraulic geometry parameters cannot be estimated, the results also implied that

382   they would not influence the routing results noticeably. Thus, in our efforts, we focused on n.

383   *Table 1: Results from the constant synthetic n and q parameter recovery experiments*

Run	n			q		
	Initial Guess	Synthetic Truth	Recovered Parameter	Initial Guess	Synthetic Truth	Recovered Parameter
1	0.271	0.03	0.028	2.7	2	2.327

2	0.271	0.04	0.035	2.7	2	2.37
3	0.271	0.05	0.046	2.7	2.5	2.390
4	0.271	0.06	0.059	2.7	2.5	2.456
5	0.271	0.07	0.070	2.7	3	2.480
6	0.068	0.03	0.030	0.6	1.0	0.574
7	0.068	0.04	0.042	0.6	1.0	0.592
8	0.068	0.05	0.055	0.6	1.5	0.730
9	0.068	0.06	0.067	0.6	1.5	0.777
10	0.068	0.07	0.087	0.6	2.5	0.690

384

385 Our second synthetic experiment (assuming constant n to be recovered by NN(A)) showed that we were

386 able to recover the constant value that was set using an NN, but there was some scattering for the

387 headwater reaches (Figure 3c, 3f). We noticed trends associated with drainage area (DA), which is

388 correlated with reach positioning in the watershed; small DA often indicates a headwater reach, while

389 large DA often indicates a reach much further downstream. There were some visible differences

390 between the synthetic hydrographs resulting from different assumed n values (comparing Figures 3a

391 and 3c), which allowed the recovered n values to mostly center around the assumed value. However,

392 the scattering of points toward the lower-DA part of Figures 3b and 3d alluded to the fact that the

393 downstream discharge was strong enough to completely constraint on the model. n in different ranges

394 can fluctuate around the mean to generate essentially the same pattern as a constant n value.

395

396 In our third set of synthetic experiments, the simple functions could be roughly recovered for most of

397 the reaches, while there may have been increased uncertainty for the furthest downstream reaches

398 (Figure 3f & 3h). There were again noticeable differences in the hydrographs (Figures 3e & 3g) from

399 previous ones. When the power-law relationship was assumed, the hydrograph matched the synthetic

400 one almost completely (Figure 3e), and the estimated n outputs from the MLP overlapped to a great

401 extent with the value to be retrieved (Figure 3f). The headwater reaches (small-DA) showed a rapid

402 decline in n with respect to increasing DA. In the middle ranges of DA, the curve followed the assumed

403 one almost exactly. Toward the higher range of DA, the recovered values were lower than the assumed

404 relationship, but the deviation was not huge because the power-law formulation became flat in this

405   range. Based on the closeness of hydrographs in all of Figure 3, we do not anticipate that further

406   optimization can bring significant improvement to the estimations. Similar to the two-constant-

407   parameter retrieval experiment, the q parameter was not recoverable and thus is not shown here.

408

409   Based on these simple experiments, it seems training on the river graphs has some promise but also

410   some limitations. It is promising because it is likely that n is related to DA which is, to some extent,

411   recoverable. It is simultaneously challenging because, as a large number of reaches contribute to one

412   gage, it is an underdetermined system. This method was not able to fully reproduce the drastic change

413   in the low-DA range presumably because this sharp slope was inconsistent with the rest of the curve,

414   and NNs generally do not output extreme values. It also ran into difficulty toward the high-DA range

415   because there were simply far fewer reaches with large DA so their roles in routing were relatively

416   minor, making the curve unconstrained in this range. This experiment informed us we should not expect

417   values of reach-scale n, particularly in the high-DA range, to be reliable, but the overall trend may have

418   merit, especially when we also have other constraints. These findings formed the basis for the next

419   stage of the work where we trained n=NN(c) for real-world data. We thus expected to extract the overall

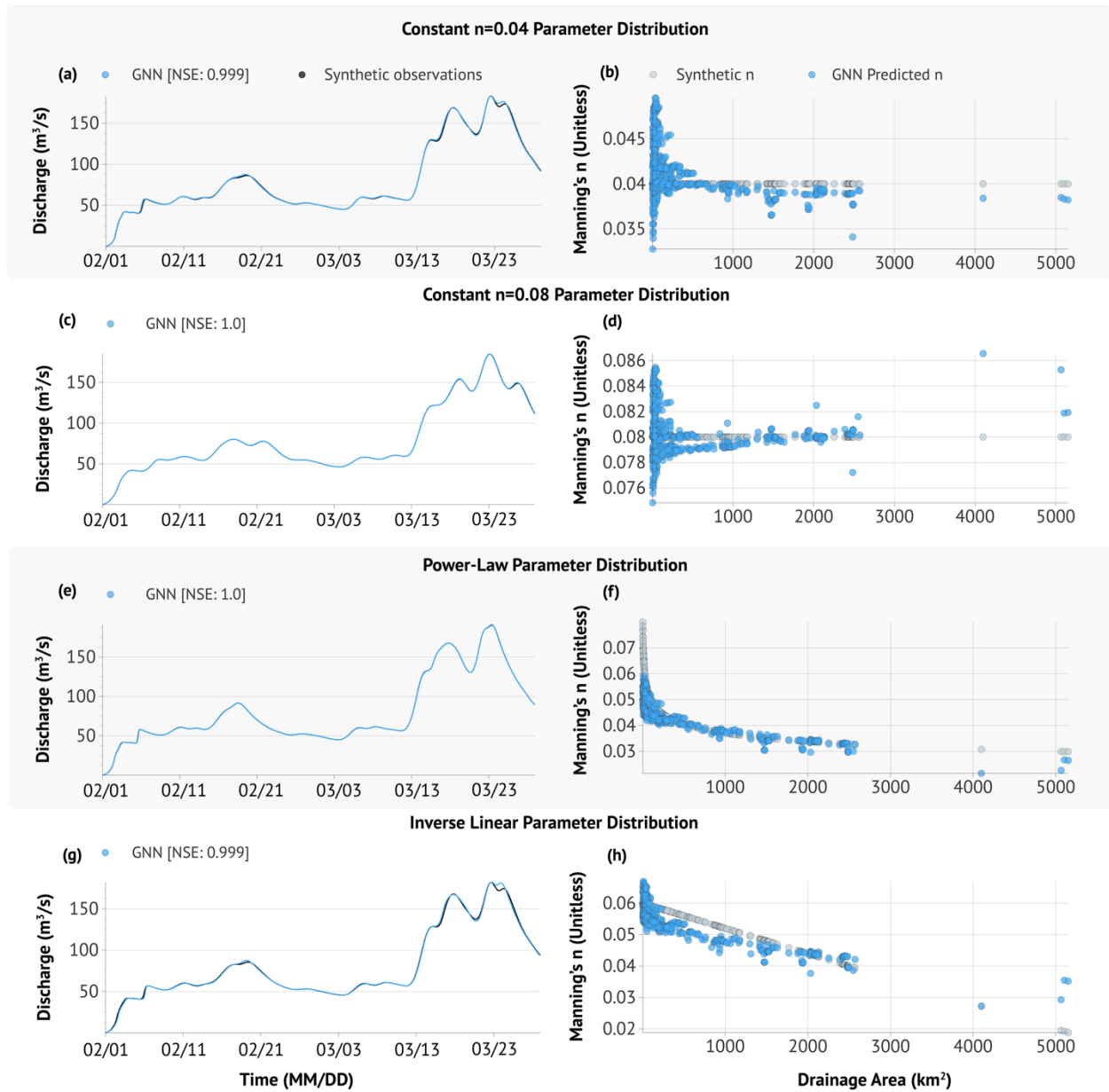420   patterns of n distribution but for the recovered q not to be meaningful.

Figure 3: Synthetic discharge distribution experiments. (a, c, e, g) Synthetic and modeled discharge over time for various assumed relationships between n and drainage area. (b, d, f, h) Synthetic modeled values of n with respect to the reach's total drainage area (km²). The NN can recover the overall pattern but is not accurate near sharp changes or for reaches with large drainage areas. Each dot in the scatter plots represents a 2-km river reach in the river network.

3.2. Training on eight weeks of real data

The real-world data experiment showed satisfactory streamflow routing in the training period, with improvements compared to approaches that did not employ the routing scheme, even though there

432 was significant bias in the rainfall input (Figure 4a). The hydrograph generated by the differentiable

433 routing model is, as expected, smoothed and delayed compared to the summation of runoffs during the

434 training period. Unlike the direct summation of the runoff, which has a timing difference from the

435 observation, the peaks of the routed hydrograph are placed almost exactly under the observed peaks,

436 leading to a high training NSE of 0.834. We noticed a substantial low bias in this training period,

437 witnessed by much lower peaks with the simulated flow compared to the observed flow. This is due to

438 bias in the rainfall-runoff modeling component and the mass-balance dictated by the MC formulation,

439 which prevents the model from adding or removing mass to remove the bias. In traditional hydrologic

440 model calibration, bias can be a significant concern as it can distorts other parameters. In this case, we

441 found the model performed well even with such bias, and appropriately focused on adjusting the timing

442 of the flood waves. This is because the allowable adjustments were limited to routing parameters, which
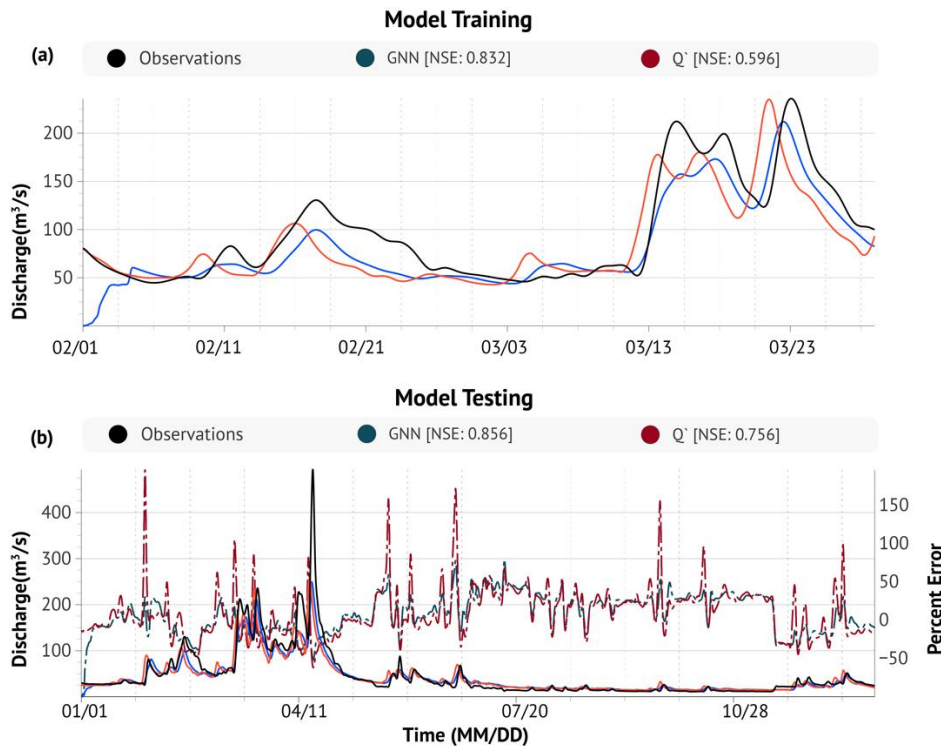
443 blocked the model from distorting other processes.

444

445

446 *Figure 4: (a) Results from training the differentiable model during an eight-week period (2001) against*

447 *USGS observations compared with the summation of lateral inputs (denoted by Q'). (b) Results from*

448 *testing the trained model from Figure 4(a) over a year period (2001) compared with the summation of*

449 *lateral inputs. A percent error has been overlaid to the graph to show how river routing is more stable*

450 *than using a summation of lateral inputs.*

451

452   The year-long test of the differentiable model yielded high metrics compared to the alternatives (Figure

453   4b), suggesting a short calibration period could yield parameterization suitable for long-term

454   simulations. The differentiable model obtained a year-long NSE of 0.857, which is consistent with the

455   median NSE in the JRB. In contrast, the summation of $Q'(\tau = 9)$ and the whole-basin $LSTM$ were at

456   0.756 and 0.801, respectively. This comparison shows that if we merely added the runoffs together

457   (which already resolved spatial heterogeneity in runoff but not the flow process), the error due to timing

458   could reduce NSE at the downstream gage. While the model had success with correctly timing the peak

459   flows, it could not compensate for LSTM's errors, resulting in significant underestimation of the peak

460   events. By design, the routing module should be detached from the errors in the runoff module.

461

462   Interestingly, without specific instructions, the scheme recovered a power-law-like relationship between

463   n and drainage area (DA) (Figure 5), similar to the one assumed in the synthetic case (Figure 3e &3f). The

464   n values were highest (near n=0.04) for smaller DA and declined gradually, approaching 0.015 at the

465   lower end. The change rate of n as a function of DA then became more gentle as DA increased. This

466   distribution agreed well with the general understanding that headwater streams running down ridges

467   (this region is characterized by Ridge and Valley formations) have larger slopes, higher roughness, more

468   vegetation, and thus higher n, while the high-order streams in the valley tend to have smaller slopes and

469   smoother beds, corresponding with lower n. In most hydrologic handbooks (Mays, 2019), a smaller n is

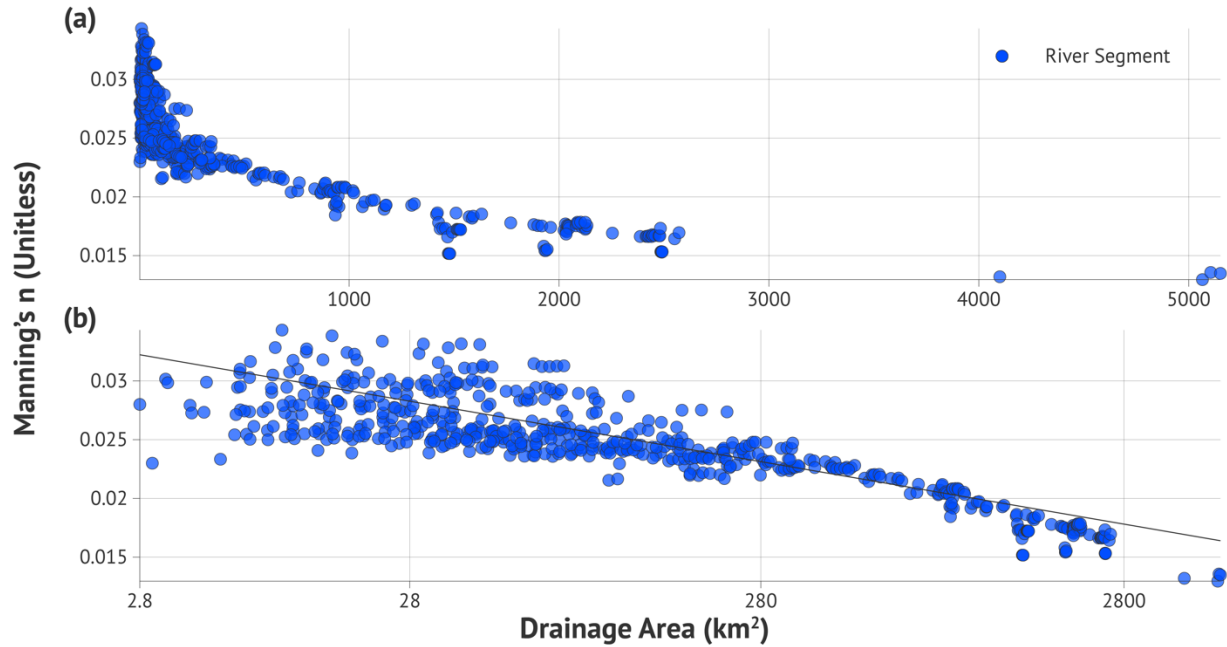470   prescribed for larger rivers.

471

Figure 5: The learned relationship between n and drainage area (square kilometers) for the Juniata River basin according to the trained GNN. (a) The distribution on a linear scale. (b) The distribution on a logarithmic scale. The network was trained for the period of 2001/02/01-2001/03/29. Each dot in the scatter plot represents a 2-km river reach.

3.3. Inner gage evaluation and effects of different training periods

Evaluating the model on the inner, untrained gages showed that the routing scheme became more competitive compared to benchmark levels as for downstream gages (Table 2). As for the benchmarks, the uniform LSTM (the catchment area of each gage is consider a basin and basin-averaged forcing/attributes were used as inputs to the trained LSTM to simulate flow at the gage) already attempts to consider routing internally but does not consider rainfall/attribute spatial heterogeneity, while the summation of Q' (runoffs were simulated from multiple HUC10 basins and added together) considers the spatial heterogeneity but not routing in the stem river. For 2 of the 4 gages with larger than ~2000 km^2 of catchment area, the differentiable routing model performed noticeably better than the uniform LSTM models for them (for the other two, they were about the same). For the three midsized subbasins (500-2000 km^2), the comparisons were mixed. For the small subbasins, and especially gage 01557500 (94.8 km^2), the uniform LSTM was noticeably better. The subbasin for 01557500 is smaller than our runoff-producing unit (HUC10s, with the smallest one ~200 km^2). This means predictions below this threshold can be error-prone. Our model was also better than the

21

492   summation of Q' for 7 of the 8 gages and the gap was larger for downstream gages (Table 2), suggesting

493   the flow convergence process matters more and more as we go downstream.

494

495   When we used multiple internal gages within the NN loss function, results improved very slightly at

496   smaller DA gages, while degraded barely noticeably at larger DA reaches. Overall, the differences are too

497   small to have real-world implications, but we can still observe the pattern that the multi-gage calibration

498   appears to produce a slightly more balanced model that improves simulations at some previously

499   weakly-simulated tributaries, at a (very minor) cost at the most downstream one. This small tradeoff

500   may be due to spatial errors in forcing data. As the model explicitly simulates flows in all modeled

501   reaches, the differentiable model provides a way to absorb data from as many stations as possible, if the

502   ungauged regions are important to the users.

503

504   *Table 2: Internal gage NSE values for the year 2001, with the rows ranked by the size of the subbasin*

505   *from small to large. The differentiable routing model was trained on the period from 2001/02/01-*

506   *2001/03/29 calculating loss from the final gage but the LSTM was trained using >3000 CONUS gages.*

507   *We include the LSTM NSE to show how the use of routing compares to just using LSTM predictions. Bold*

508   *font indicates the top performing model for each gage.*

Edge ID	Gage Number	Basin Drainage Area (km^2)	Uniform LSTM	Q` Runoff NSE (τ = 9)	Differentiable routing model (τ = 9)	Multiple Gage Loss for differentiable routing (τ = 9)
1280	01557500	94.8	**0.8149**	0.5575	0.5623	0.5627
1053	01560000	440.5	**0.7028**	0.6054	0.6578	0.6625
2799	01558000	542.1	**0.8201**	0.7473	0.6963	0.6981
4780	01556000	723.5	0.6624	0.6568	0.6937	**0.6957**
2662	01562000	1943.5	0.7957	0.6857	0.7942	**0.7977**
4801	01559000	2103.0	0.7815	0.7449	0.8136	**0.8172**

| 2689 | 01563200 | 2482.9 | 0.5703 | 0.6497 | **0.7831** | 0.7773 |
| 4809 | 01563500 | 5212.8 | 0.8024 | 0.7563 | **0.857** | 0.8546 |

509

510   The above comparisons informed us of the favorable and unfavorable ranges of applicability for our

511   workflow: the differentiable model found competitive advantages for stem rivers with catchments

512   greater than 2,000 km^2, but may run into issues for scales smaller than the smallest runoff-producing

513   unit (HUC10, around 200 km^2). The issues for the smallest basins could be attributed to the procedure

514   that transfers mass from subbasin to regular grids on the river network, which should be improved in

515   future work. As a result, the smallest headwater basins are best to be directly simulated by the uniform

516   LSTM models. Also, smaller runoff-generating units could be used in the future to mitigate this issue.

517   The advantages of the differentiable routing model over the uniform LSTM for larger basins were due to

518   resolving the heterogeneity in rainfall and basin static attributes as well as better representing routing.

519   The uniform LSTM can internally represent some flow lags but it appears less effective as basin size

520   increases.

521

522   The results imply that the advantages will increase for even larger basins, where currently LSTM does

523   not apply well, along with basins where rainfall heterogeneity makes a big difference. The JRB is situated

524   in the northeastern part of the CONUS; many other regions may exhibit more prominent effects of

525   heterogeneity. For example, past studies have always found it difficult to simulate large basins on the

526   northern and central Great Plains (Feng et al., 2020; Martinez & Gupta, 2010), potentially due to

527   spatially-concentrated rainfall and runoff generation (Fang & Shen, 2017). Also, in the mountainous

528   areas of the CONUS Northwest and Southeast, orographic precipitation could have significant spatial

529   concentration. We hypothesize applying models to smaller basins and incorporating the routing scheme

530   will allow these regions to be better modeled.
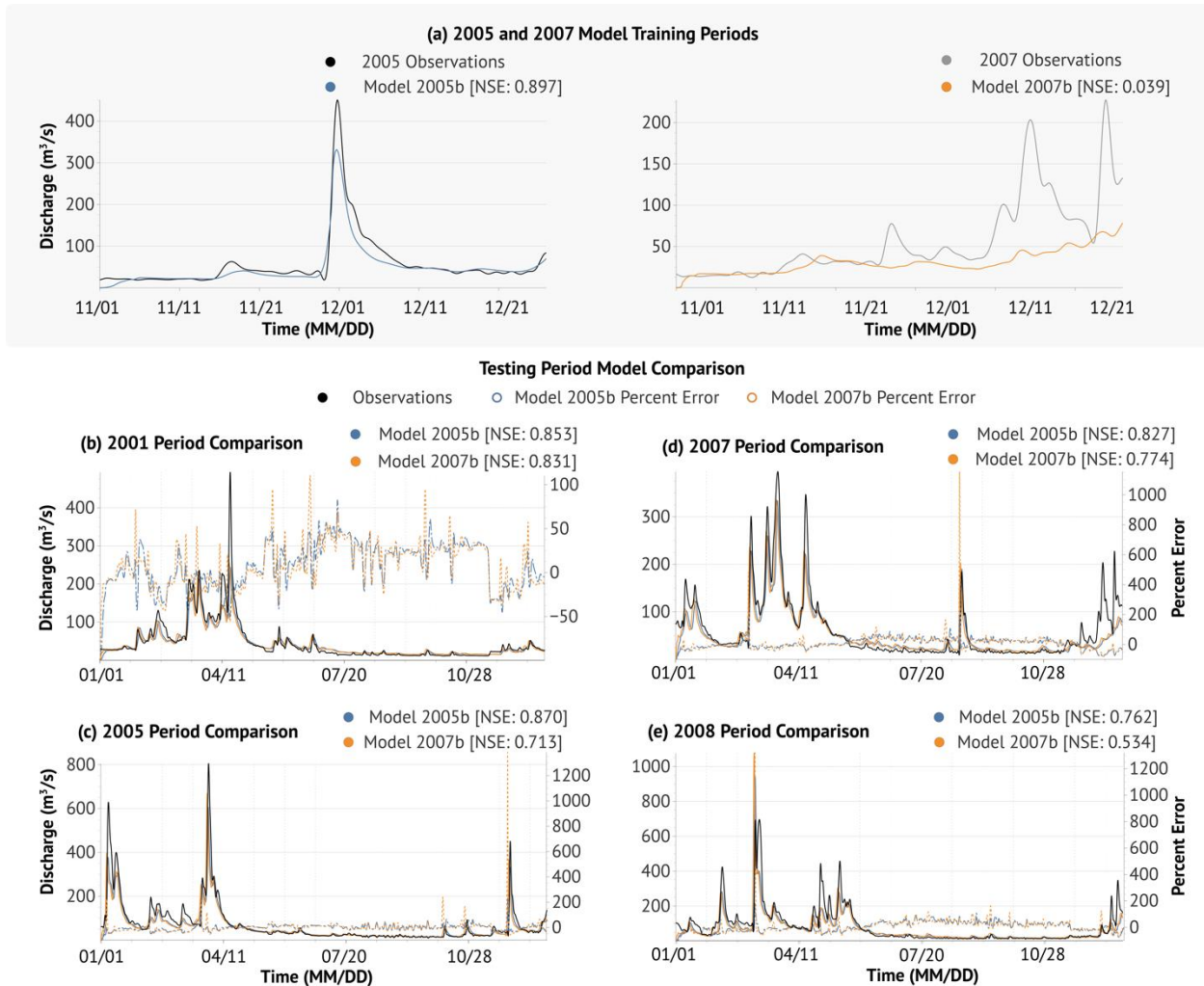
531

532   As expected, the training periods selected can exert an influence on the model, but as long as we used

533   reasonable training periods, the results were acceptable. When the scheme was trained on eight-week

534   periods from different years, it generated somewhat different but mostly functional parameterizations

535   (Figure A2 in the Appendix), unless it was trained in some unreasonable training periods where the

536   LSTM had drastic differences from the observed outflows (Table 3). The maximum achievable NSEs for

537   the years of 2001, 2005, 2007, and 2008 were 0.857, 0.87, 0.827, and 0.787, respectively, with all

538   models outperforming Q` NSE values for their respective periods (Table A3 in the Appendix). We found

539   that if the models were trained on other periods (2001a, 2001b, 2005b, 2007a), the test NSEs were

540   mostly decent, and at least not drastically worse. However, choosing 2007b or 2008a led to notably

541   inferior results (Figure 6b-e). Examining the characteristics of the different training periods, we see that

542   the problematic training periods did not contain full flood rise and recession phases (Figure 6a & 6b). As

543   a result, 2007b and 2008a as training periods led to either the lowest or the highest n values and also

544   had relatively low NSE values (Figure A2 in the Appendix). Similarly, training period 2005a gave relatively

545   large n values which also resulted in suboptimal (although still decent) results in all the years. Hence, we

546   need to pick periods that (i) contain full flood rise and recession phases; and (ii) have high runoff NSEs.

547   In addition, even though the routing simulation can be improved by short training periods, the spread of

548   estimated n again shows that the identification of n via small training periods can be difficult. Future

549   work could employ longer training periods to compromise across different periods and obtain broadly-

550   performant parameterization. However, another possibility is that n itself can vary over time, which

551   would be an orthodoxy but not unthinkable idea.

552

553

554

555   *Table 3. The NSE values correspond to testing differentiable models on different test years. Bold font*

556   *indicates the highest NSE, while underlined metrics indicate the lowest (noticeably worse than obtained*

557   *from other periods) for the testing period.*

558

Testing Period	Training Period							
	2001a 02/01-3/29	2001b 11/01-12/26	2005a 02/01-3/29	2005b 11/01-12/26	2007a 02/01-3/29	2007b 11/01-12/26	2008a 02/01-3/29	2008b 11/01-12/26
2001	**0.857**	0.845	0.850	0.853	0.857	0.831	<u>0.782</u>	0.856
2005	0.797	0.828	0.843	**0.870**	0.816	<u>0.713</u>	0.785	0.785
2007	0.815	0.812	0.821	**0.827**	0.819	0.774	<u>0.753</u>	0.813
2008	0.643	0.715	0.723	0.762	0.676	<u>0.534</u>	**0.787**	0.623
Average	0.778	0.800	0.809	**0.828**	0.792	<u>0.713</u>	0.777	0.769

559
560

Figure 6: (a) Two training periods: 2005 and 2007a. The former contains a full rising-recession cycle while the latter does not have a complete cycle for training, thus leading to larger errors during test. The solid line indicates the training of Model 2005b while the dashed line indicates Model 2007b during the time period of 11/01-12/27 during the years 2005 and 2007, respectively. (b-c) Test periods for these two models: (b) 2001, (c) 2005, (d) 2007, and (e) 2008. For (b-e) the solid line indicates discharge while the dashed line indicates percent error of each model's output compared with the observations.

3.4. Further discussion

Although the estimated n values were both functional for routing streamflow and physically meaningful, the results suggest the downstream discharge only poses a moderate constraint on the n values, and short training periods may not be sufficient to identify the true n values. Hence, while our procedure can

573   obtain *n* parameterization performant for long-term simulations, we do not claim that the procedure

574   retrieved the "true" *n* parameterization. Especially considering there are many input variables to the NN

575   that covary in space, it may be difficult to disentangle causation from correlation. Due to the lack of

576   ground truth for *n* in the real-data case, we leave this evaluation for future effort as we compile more

577   measurement data. Recall that we were able to retrieve the overall pattern of *n* in the synthetic

578   experiments but faced large uncertainties in some areas of the parameter space. This is attributed to the

579   numerous degrees of freedom (a high-dimensional input space for the NN, influencing many reaches)

580   constrained by only one downstream output with a relatively short training period. Nevertheless, this

581   training is valuable because discharge data can be widely available, and we will be able to employ it in

582   conjunction with other constraints, e.g., scattered measurements or expert-specified relationships.

583

584   Regarding other potential recoverable parameters, we suspect the dimensionless MC inflow/outflow

585   weighing parameter X, which indicates the shape of the assumed flood prism, cannot be identified for

586   the same reason as q --- the geometries of the channel do not impact flow rates in a meaningful way.

587   Future work could investigate if learning it produces any benefit. Similarly, linear channel coefficient *p*

588   values were also never recoverable in single parameter tests and decreased resulting NSE values when

589   used as a tunable parameter. Thus, we did not include it in this study. In addition, we hypothesize using

590   more complex MC formula, e.g., the nonlinear form of the Cunge equation (the celerity is defined as

591   *dQ/dA*)*,* which might add to numerical challenges for large-scale simulations, would lead to different *n*

592   values, as the recovered values are inherently linked to the inverse model employed.

593

594   Here we employed a static parameterization scheme for *n*, following the conventional approach.

595   However, the framework allows for the use of a dynamic *n* (likely dependent on Q). It is not clear if we

596   must use a static parameterization as done conventionally, as some previous studies have found a

597   dynamic *n* to offer better results (Ye et al., 2018). In the future, it will be interesting to see if a dynamical

598   *n* parameterization could significantly impact the routing results. On another note, we chose an eight-

599   week time period as our training length as a probe to assess the required training duration and selection

600   criteria for such periods. We trained eight different models (Section 3.3) on different time periods and

601   showed that the choice of training period timing, and LSTM performance for the inputs played

602   important roles. Future effort should include longer training periods to most robustly estimate the

603   parameters.

604

605   When investigating the impact of multiple gages, rather than a single downstream-most gage (in model

606   loss calculation and parameter updates), results were very similar in terms of NSE score and recovered

607   Manning's *n* parameters. We believe this may be because the JRB is a relatively small river network, so

608   internal gage observations are highly correlated in discharge volume (m³/s) and fluctuation (storm event

609   timing). Adding more gages could be useful if flows in different parts of the basin need to be accurately

610   reported, but may be less important if only the downstream gage is of concern.

611

612   Our approach, akin to a classical routing scheme, is modular --- the trained weights of the NN that

613   generates *n* are not tied to a particular runoff model. Our work can be coupled to traditional models in

614   multiple ways. Firstly, the trained network can be used to generate *n* for traditional models. In this way,

615   no change is required on the part of the traditional models. Secondly, the neural network and the

616   trained weights can be ported to other programming environments like Fortran. This makes it possible

617   to use the trained parameterizations as a built-in module in continental-scale models (Greuell et al.,

618   2015; Johnson et al., 2019; Regan et al., 2018). An alternative approach is to lump both the routing and

619   runoff simulations into one problem and optimize them together, as demonstrated in some other

620   studies (Jia et al., 2021). In our case, this would mean that we would train both the runoff LSTM and the

621   routing module together. In many big-data DL case studies, lumped models tend to have higher

622   performance compared to a workflow that separates the tasks into multiple minor tasks. However, in

623   our case here, this leads to coadaptation concerns. Moreover, our approach is modular so it can be

624   easily coupled to other runoff models, e.g., a non-differentiable traditional model, or a differentiable

625   one (Feng, Beck, et al., 2022; Feng, Liu, et al., 2022).

626

627   **4. Conclusions**

628   In this work, we used a combination of a pre-trained LSTM rainfall-runoff model and Muskingum-Cunge

629   routing to create a learnable routing model, or, from the perspective of machine learning, a physics-

630   informed graph neural network. This model predicts streamflow in stem rivers and learn river

631   parameters throughout a river network, which is urgently needed to improve the next-generation large-

632   scale hydrologic models. Because our framework is built on physical principles and estimates widely-

633   used *n* values, it can be easily ported to work with other models. For example, the trained NN and the

634   weights can be loaded into Fortran or C programs to support traditional hydrologic models or routing

635   schemes, e.g. (H. Li et al., 2013; Mizukami et al., 2016). Our synthetic experiments recovered the overall

636   spatial pattern of *n* with moderate accuracy but could not recover the channel cross-sectional geometry

637   parameter (q). Furthermore, our synthetic experiments yielded promising results in recovering synthetic

638   n and drainage area relationships, implying there is potential to learn reach-scale physics in the river

639   network using differentiable modeling.

640

641   With the real-world data, short-term training periods of downstream hydrographs can produce n

642   parameterization that improve long-term routing results, but may be insufficient to constrain the n

643   values more precisely than a general spatial pattern. Eight weeks of real-world data produced decent

644   long-term streamflow routing and improved upon approaches that did not use routing, yet training on

645   different periods could result in somewhat different distributions. When looking at the n vs drainage

646   area distribution attained by our trained model against USGS observations, we found that the n values

647   agreed with the literature bounds for the area, but the absolute magnitudes may fluctuate depending

648   on the training period. Besides using longer training periods to obtain n values that compromise across

649   periods, future work should also consider if n should be treated as dynamic in time. Further work can

650   expand this analysis to other basins with different conditions (streams outside of the Ridge and Valley

651   physiographic division of the CONUS) to see if the model can still identify their trends correctly.

652   Reviewing the internal gage NSE scores over a full year of data showed a correlation between drainage

653   area and the relative advantage of our routing scheme, highlighting the impacts of heterogeneity and

654   flow convergence.

655

656

657   **Open Research**

664

665   **Funding Acknowledgements**

668

669

References

671 Aboelyazeed, D., Xu, C., Hoffman, F. M., Jones, A. W., Rackauckas, C., Lawson, K. E., & Shen,

672   C. (2022). A differentiable ecosystem modeling framework for large-scale inverse

673   problems: demonstration with photosynthesis simulations. *Biogeosciences Discussions*.

674   https://doi.org/10.5194/bg-2022-211

675 Adnan, R. M., Petroselli, A., Heddam, S., Santos, C. A. G., & Kisi, O. (2021). Comparison of

676   different methodologies for rainfall–runoff modeling: machine learning vs conceptual

677   approach. *Natural Hazards*, *105*(3), 2987–3011. https://doi.org/10.1007/s11069-020-

678   04438-2

679 Arcement, G. J., & Schneider, V. R. (1989). *Guide for Selecting Manning's Roughness*

680   *Coefficients for Natural Channels and Flood Plains* (Water-Supply Paper No. 2339). U.S.

681   Geological Survey. Retrieved from https://pubs.usgs.gov/wsp/2339/report.pdf

682 Baydin, A. G., Pearlmutter, B. A., Radul, A. A., & Siskind, J. M. (2018). Automatic differentiation

683   in machine learning: A survey. *Journal of Machine Learning Research*, *18*(153), 1–43.

684   Retrieved from http://jmlr.org/papers/v18/17-468.html

685 Candela, A., Noto, L. V., & Aronica, G. (2005). Influence of surface roughness in hydrological

686   response of semiarid catchments. *Journal of Hydrology*, *313*(3), 119–131.

687   https://doi.org/10.1016/j.jhydrol.2005.01.023

688 Carabajal, C. C., & Harding, D. J. (2006). SRTM C-Band and ICEsat laser altimetry elevation

689   comparisons as a function of tree cover and relief. *Photogrammetric Engineering &*

690   *Remote Sensing*, *72*(3), 287–298. https://doi.org/10/ggj69r

691 Chaney, N. W., Minasny, B., Herman, J. D., Nauman, T. W., Brungard, C. W., Morgan, C. L. S.,

692   et al. (2019). POLARIS Soil Properties: 30-m Probabilistic Maps of Soil Properties Over

693   the Contiguous United States. *Water Resources Research*, *55*(4), 2916–2938.

694   https://doi.org/10/ggj68b

695   Cunge, J. A. (1969). On the subject of a flood propagation computation method (Musklngum

696   method). *Journal of Hydraulic Research*, *7*(2), 205–230.

697   https://doi.org/10.1080/00221686909500264

698   Dottori, F., Szewczyk, W., Ciscar, J.-C., Zhao, F., Alfieri, L., Hirabayashi, Y., et al. (2018).

699   Increased human and economic losses from river flooding with anthropogenic warming.

700   *Nature Climate Change*, *8*(9), 781–786. https://doi.org/10.1038/s41558-018-0257-z

701   Douben, K.-J. (2006). Characteristics of river floods and flooding: a global overview, 1985–

702   2003. *Irrigation and Drainage*, *55*(S1), S9–S21. https://doi.org/10.1002/ird.239

703   Duan, S., Ullrich, P., & Shu, L. (2020). Using convolutional neural networks for streamflow

704   projection in California. *Frontiers in Water*, *2*. https://doi.org/10.3389/frwa.2020.00028

705   Falcone, J. A. (2011). GAGES-II: Geospatial Attributes of Gages for Evaluating Streamflow

706   [Data set]. *GAGES-II: Geospatial Attributes of Gages for Evaluating Streamflow*. USGS

707   Unnumbered Series, Reston, VA: U.S. Geological Survey.

708   https://doi.org/10.3133/70046617

709   Fan, W., Ma, Y., Li, Q., He, Y., Zhao, E., Tang, J., & Yin, D. (2019, November 22). Graph neural

710   networks for social recommendation. arXiv. https://doi.org/10.48550/arXiv.1902.07243

711   Fang, K., & Shen, C. (2017). Full-flow-regime storage-streamflow correlation patterns provide

712   insights into hydrologic functioning over the continental US. *Water Resources Research*,

713   *53*(9), 8064–8083. https://doi.org/10.1002/2016WR020283

714   Fang, K., Shen, C., Kifer, D., & Yang, X. (2017). Prolongation of SMAP to spatiotemporally

715   seamless coverage of continental U.S. using a deep learning neural network.

716   *Geophysical Research Letters*, *44*(21), 11,030-11,039.

717   https://doi.org/10.1002/2017gl075619

718   Fang, K., Pan, M., & Shen, C. (2019). The value of SMAP for long-term soil moisture estimation

719   with the help of deep learning. *IEEE Transactions on Geoscience and Remote Sensing*,

720   *57*(4), 2221–2233. https://doi.org/10/gghp3v

721   Feng, D., Fang, K., & Shen, C. (2020). Enhancing streamflow forecast and extracting insights

722   using long-short term memory networks with data integration at continental scales.

723   *Water Resources Research*, *56*(9), e2019WR026793.

724   https://doi.org/10.1029/2019WR026793

725   Feng, D., Liu, J., Lawson, K., & Shen, C. (2022). Differentiable, learnable, regionalized process-

726   based models with multiphysical outputs can approach state-of-the-art hydrologic

727   prediction accuracy. *Water Resources Research*, *58*(10), e2022WR032404.

728   https://doi.org/10.1029/2022WR032404

729   Feng, D., Beck, H., Lawson, K., & Shen, C. (2022). The suitability of differentiable, learnable

730   hydrologic models for ungauged regions and climate change impact assessment.

731   *Hydrology and Earth System Sciences Discussions*, 1–28. https://doi.org/10.5194/hess-

732   2022-245

733   France-Presse, A. (2022, June 19). At least 59 dead and millions stranded as floods devastate

734   India and Bangladesh. *The Guardian*. Retrieved from

735   https://www.theguardian.com/world/2022/jun/18/at-least-18-dead-and-millions-stranded-

736   as-floods-devastate-india-and-bangladesh

737   François, B., Schlef, K. E., Wi, S., & Brown, C. M. (2019). Design considerations for riverine

738   floods in a changing climate – A review. *Journal of Hydrology*, *574*, 557–573.

739   https://doi.org/10.1016/j.jhydrol.2019.04.068

740   Friedl, M., & Sulla-Menashe, D. (2019). MCD12Q1 MODIS/Terra+Aqua Land Cover Type Yearly

741   L3 Global 500m SIN Grid V006 [Data set].

742   https://doi.org/10.5067/MODIS/MCD12Q1.006

743   Getirana, A. C. V., Boone, A., Yamazaki, D., Decharme, B., Papa, F., & Mognard, N. (2012).

744   The Hydrological Modeling and Analysis Platform (HyMAP): Evaluation in the Amazon

745   Basin. *Journal of Hydrometeorology*, *13*(6), 1641–1665. https://doi.org/10/f4jbcx

746   Gleason, C. J. (2015). Hydraulic geometry of natural rivers: A review and future directions.

747   *Progress in Physical Geography*. https://doi.org/10/f7dsqm

748   Greuell, W., Andersson, J. C. M., Donnelly, C., Feyen, L., Gerten, D., Ludwig, F., et al. (2015).

749   Evaluation of five hydrological models across Europe and their suitability for making

750   projections under climate change. *Hydrology and Earth System Sciences Discussions*,

751   *12*(10), 10289–10330. https://doi.org/10.5194/hessd-12-10289-2015

752   He, M., Wu, S., Huang, B., Kang, C., & Gui, F. (2022). Prediction of total nitrogen and

753   phosphorus in surface water by deep learning methods based on multi-scale feature

754   extraction. *Water*, *14*(10), 1643. https://doi.org/10.3390/w14101643

755   Hochreiter, S. (1998). The vanishing gradient problem during learning recurrent neural nets and

756   problem solutions. *International Journal of Uncertainty, Fuzziness and Knowledge-*

757   *Based Systems*, *06*(02), 107–116. https://doi.org/10.1142/S0218488598000094

758   Hochreiter, S., & Schmidhuber, J. (1997). Long Short-Term Memory. *Neural Computation*, *9*(8),

759   1735–1780. https://doi.org/10.1162/neco.1997.9.8.1735

760   HorizonSystems. (2016). NHDPlus version 2 [Data set]. Retrieved from http://www.horizon-

761   systems.com/nhdplus/NHDplusV2_home.php

762   Hrnjica, B., Mehr, A. D., Jakupović, E., Crnkić, A., & Hasanagić, R. (2021). Application of deep

763   learning neural networks for nitrate prediction in the Klokot River, Bosnia and

764   Herzegovina. In *2021 7th International Conference on Control, Instrumentation and*

765   *Automation (ICCIA)* (pp. 1–6). https://doi.org/10.1109/ICCIA52082.2021.9403565

766   Huscroft, J., Gleeson, T., Hartmann, J., & Börker, J. (2018). Compiling and mapping global

767   permeability of the unconsolidated and consolidated Earth: GLobal HYdrogeology MaPS

768   2.0 (GLHYMPS 2.0). *Geophysical Research Letters*, *45*(4), 1897–1904.

769   https://doi.org/10.1002/2017GL075860

770   International Panel on Climate Change (IPCC). (2012). *Managing the Risks of Extreme Events*

771   *and Disasters to Advance Climate Change Adaptation* (p. 582). Retrieved from

772   https://www.ipcc.ch/report/managing-the-risks-of-extreme-events-and-disasters-to-

773   advance-climate-change-adaptation/

774 Ji, X., Lesack, L., Melack, J. M., Wang, S., Riley, W. J., & Shen, C. (2019). Seasonal and inter-

775   annual patterns and controls of hydrological fluxes in an Amazon floodplain lake with a

776   surface-subsurface processes model. *Water Resources Research*, *55*(4), 3056–3075.

777   https://doi.org/10/gghp4s

778 Jia, X., Zwart, J., Sadler, J., Appling, A., Oliver, S., Markstrom, S., et al. (2021). Physics-Guided

779   Recurrent Graph Model for Predicting Flow and Temperature in River Networks. In

780   *Proceedings of the 2021 SIAM International Conference on Data Mining (SDM)* (pp.

781   612–620). Society for Industrial and Applied Mathematics.

782   https://doi.org/10.1137/1.9781611976700.69

783 Johnson, J. M., Munasinghe, D., Eyelade, D., & Cohen, S. (2019). An integrated evaluation of

784   the National Water Model (NWM)–Height Above Nearest Drainage (HAND) flood

785   mapping methodology. *Natural Hazards and Earth System Sciences*, *19*(11), 2405–

786   2420. https://doi.org/10.5194/nhess-19-2405-2019

787 Kalyanapu, A. J., Burian, S. J., & McPherson, T. N. (2009). Effect of land use-based surface

788   roughness on hydrologic model output. *Journal of Spatial Hydrology*, *9*(2), 51–71.

789   Retrieved from https://scholarsarchive.byu.edu/josh/vol9/iss2/2

790 Khorashadi Zadeh, F., Nossent, J., Sarrazin, F., Pianosi, F., van Griensven, A., Wagener, T., &

791   Bauwens, W. (2017). Comparison of variance-based and moment-independent global

792   sensitivity analysis approaches by application to the SWAT model. *Environmental*

793   *Modelling & Software*, *91*, 210–222. https://doi.org/10.1016/j.envsoft.2017.02.001

794 Kingma, D. P., & Ba, J. (2017, January 29). Adam: A method for stochastic optimization. arXiv.

795   https://doi.org/10.48550/arXiv.1412.6980

796   Koks, E. E., & Thissen, M. (2016). A multiregional impact assessment model for disaster

797   analysis. *Economic Systems Research*, *28*(4), 429–449.

798   https://doi.org/10.1080/09535314.2016.1232701

799   Kratzert, F., Klotz, D., Shalev, G., Klambauer, G., Hochreiter, S., & Nearing, G. (2019). Towards

800   learning universal, regional, and local hydrological behaviors via machine learning

801   applied to large-sample datasets. *Hydrology and Earth System Sciences*, *23*(12), 5089–

802   5110. https://doi.org/10.5194/hess-23-5089-2019

803   Leopold, L. B., & Maddock, T. Jr. (1953). The hydraulic geometry of stream channels and some

804   physiographic implications. *USGS Professional Paper*, *252*. https://doi.org/10/ggj7hw

805   Leshno, M., Lin, V. Ya., Pinkus, A., & Schocken, S. (1993). Multilayer feedforward networks with

806   a nonpolynomial activation function can approximate any function. *Neural Networks*,

807   *6*(6), 861–867. https://doi.org/10/bjjdg2

808   Li, H., Wigmosta, M. S., Wu, H., Huang, M., Ke, Y., Coleman, A. M., & Leung, L. R. (2013). A

809   physically based runoff routing model for land surface and earth system models. *Journal

810   of Hydrometeorology*, *14*(3), 808–828. https://doi.org/10/ggj7ph

811   Li, H.-Y., Tan, Z., Ma, H., Zhu, Z., Abeshu, G. W., Zhu, S., et al. (2022). A new large-scale

812   suspended sediment model and its application over the United States. *Hydrology and

813   Earth System Sciences*, *26*(3), 665–688. https://doi.org/10.5194/hess-26-665-2022

814   Lin, G.-Y., Chen, H.-W., Chen, B.-J., & Yang, Y.-C. (2022). Characterization of temporal PM2.5,

815   nitrate, and sulfate using deep learning techniques. *Atmospheric Pollution Research*,

816   *13*(1), 101260. https://doi.org/10.1016/j.apr.2021.101260

817   Liu, J., Rahmani, F., Lawson, K., & Shen, C. (2022). A multiscale deep learning model for soil

818   moisture integrating satellite and in situ data. *Geophysical Research Letters*, *49*(7),

819   e2021GL096847. https://doi.org/10.1029/2021GL096847

820   Liu, L., Ao, T., Zhou, L., Takeuchi, K., Gusyev, M., Zhang, X., et al. (2022). Comprehensive

821   evaluation of parameter importance and optimization based on the integrated sensitivity

822   analysis system: A case study of the BTOP model in the upper Min River Basin, China.

823   *Journal of Hydrology*, *610*, 127819. https://doi.org/10.1016/j.jhydrol.2022.127819

824   Martinez, G. F., & Gupta, H. V. (2010). Toward improved identification of hydrological models: A

825   diagnostic evaluation of the "abcd" monthly water balance model for the conterminous

826   United States. *Water Resources Research*, *46*(8).

827   https://doi.org/10.1029/2009WR008294

828   Mays, L. W. (2010). *Water Resources Engineering* (2nd edition). Tempe, AZ: Wiley.

829   Mays, L. W. (2019). *Water Resources Engineering* (3rd edition). Tempe, AZ: Wiley. Retrieved

830   from https://www.wiley.com/en-us/Water+Resources+Engineering%2C+3rd+Edition-p-

831   9781119493167

832   Meyal, A. Y., Versteeg, R., Alper, E., Johnson, D., Rodzianko, A., Franklin, M., & Wainwright, H.

833   (2020). Automated cloud based long short-term memory neural network based SWE

834   prediction. *Frontiers in Water*, *2*. https://doi.org/10.3389/frwa.2020.574917

835   Mizukami, N., Clark, M. P., Sampson, K., Nijssen, B., Mao, Y., McMillan, H., et al. (2016).

836   mizuRoute version 1: A river network routing tool for a continental domain water

837   resources applications. *Geoscientific Model Development*, *9*(6), 2223–2238.

838   https://doi.org/10.5194/gmd-9-2223-2016

839   Moore, R. B., & Dewald, T. G. (2016). The road to NHDPlus — Advancements in digital stream

840   networks and associated catchments. *JAWRA Journal of the American Water*

841   *Resources Association*, *52*(4), 890–900. https://doi.org/10.1111/1752-1688.12389

842   Nash, J. E., & Sutcliffe, J. V. (1970). River flow forecasting through conceptual models part I —

843   A discussion of principles. *Journal of Hydrology*, *10*(3), 282–290.

844   https://doi.org/10/fbg9tm

845   O, S., & Orth, R. (2021). Global soil moisture data derived through machine learning trained with

846   in-situ measurements. *Scientific Data*, *8*(1), 170. https://doi.org/10.1038/s41597-021-

847   00964-1

848 Ouyang, W., Lawson, K., Feng, D., Ye, L., Zhang, C., & Shen, C. (2021). Continental-scale

849   streamflow modeling of basins with reservoirs: Towards a coherent deep-learning-based

850   strategy. *Journal of Hydrology*, *599*, 126455.

851   https://doi.org/10.1016/j.jhydrol.2021.126455

852 Pan, M., & Wood, E. F. (2013). Inverse streamflow routing. *Hydrology and Earth System*

853   *Sciences*, *17*(11), 4577–4588. https://doi.org/10/f5k6nq

854 Prein, A. F., Rasmussen, R. M., Ikeda, K., Liu, C., Clark, M. P., & Holland, G. J. (2017). The

855   future intensification of hourly precipitation extremes. *Nature Climate Change*, *7*(1), 48–

856   52. https://doi.org/10.1038/nclimate3168

857 Rahmani, F., Shen, C., Oliver, S., Lawson, K., & Appling, A. (2021). Deep learning approaches

858   for improving prediction of daily stream temperature in data-scarce, unmonitored, and

859   dammed basins. *Hydrological Processes*, *35*(11), e14400.

860   https://doi.org/10.1002/hyp.14400

861 Rahmani, F., Lawson, K., Ouyang, W., Appling, A., Oliver, S., & Shen, C. (2021). Exploring the

862   exceptional performance of a deep learning stream temperature model and the value of

863   streamflow data. *Environmental Research Letters.* https://doi.org/10.1088/1748-

864   9326/abd501

865 Regan, R. S., Markstrom, S. L., Hay, L. E., Viger, R. J., Norton, P. A., Driscoll, J. M., &

866   LaFontaine, J. H. (2018). *Description of the National Hydrologic Model for use with the*

867   *Precipitation-Runoff Modeling System (PRMS)* (No. 6-B9). *Techniques and Methods*.

868   U.S. Geological Survey. https://doi.org/10.3133/tm6B9

869 Rice, D. (2019, May 28). Mississippi River flood is longest-lasting in over 90 years, since "Great

870   Flood" of 1927. *USA Today*. Retrieved from

871   https://www.usatoday.com/story/news/nation/2019/05/28/mississippi-river-flooding-

872   longest-lasting-since-great-flood-1927/1261049001/

873   Saha, G. K., Rahmani, F., Shen, C., Li, L., & Cibin, R. (2023). A deep learning-based novel

874   approach to generate continuous daily stream nitrate concentration for nitrate data-

875   sparse watersheds. *Science of The Total Environment*, *878*, 162930.

876   https://doi.org/10.1016/j.scitotenv.2023.162930

877   Shen, C., & Lawson, K. (2021). Applications of Deep Learning in Hydrology. In *Deep Learning*

878   *for the Earth Sciences* (pp. 283–297). John Wiley & Sons, Ltd.

879   https://doi.org/10.1002/9781119646181.ch19

880   Shen, C., & Phanikumar, M. S. (2010). A process-based, distributed hydrologic model based on

881   a large-scale method for surface–subsurface coupling. *Advances in Water Resources*,

882   *33*(12), 1524–1541. https://doi.org/10/c4r8k5

883   Shen, C., Niu, J., & Phanikumar, M. S. (2013). Evaluating controls on coupled hydrologic and

884   vegetation dynamics in a humid continental climate watershed using a subsurface - land

885   surface processes model. *Water Resources Research*, *49*(5), 2552–2572.

886   https://doi.org/10/f5gcrx

887   Shen, C., Niu, J., & Fang, K. (2014). Quantifying the effects of data integration algorithms on the

888   outcomes of a subsurface–land surface processes model. *Environmental Modelling &*

889   *Software*, *59*, 146–161. https://doi.org/10/ggj7mp

890   Shen, C., Riley, W. J., Smithgall, K. M., Melack, J. M., & Fang, K. (2016). The fan of influence of

891   streams and channel feedbacks to simulated land surface water and carbon dynamics.

892   *Water Resources Research*, *52*(2), 880–902. https://doi.org/10/f8gppj

893   Shen, C., Chen, X., & Laloy, E. (2021). Editorial: Broadening the use of machine learning in

894   hydrology. *Frontiers in Water*, *3*. https://doi.org/10.3389/frwa.2021.681023

895   Shen, C., Fang, K., Feng, D., & Bindas, T. (2021). mhpi/hydroDL: MHPI-hydroDL [Data set].

896   Zenodo. https://doi.org/10.5281/zenodo.5015120

897   Sun, A. Y., Jiang, P., Mudunuru, M. K., & Chen, X. (2021). Explore spatio-temporal learning of

898   large sample hydrology using graph neural networks. *Water Resources Research*,

899   *57*(12), e2021WR030394. https://doi.org/10.1029/2021WR030394

900   Sun, A. Y., Jiang, P., Yang, Z.-L., Xie, Y., & Chen, X. (2022). A graph neural network approach

901   to basin-scale river network learning: The role of physics-based connectivity and data

902   fusion. *Hydrology and Earth System Sciences Discussions*. https://doi.org/10.5194/hess-

903   2022-111

904   Tsai, W.-P., Feng, D., Pan, M., Beck, H., Lawson, K., Yang, Y., et al. (2021). From calibration to

905   parameter learning: Harnessing the scaling effects of big data in geoscientific modeling.

906   *Nature Communications*, *12*(1), 5988. https://doi.org/10.1038/s41467-021-26107-z

907   US Army Corps of Engineers. (2018). National Inventory of Dams (NID) [Data set]. Retrieved

908   from https://nid.sec.usace.army.mil/

909   USGS ScienceBase-Catalog. (2022). National Elevation Dataset (NED). Retrieved September

910   13, 2022, from https://www.sciencebase.gov/catalog/item/4fcf8fd4e4b0c7fe80e81504

911   Virtanen, P., Gommers, R., Oliphant, T. E., Haberland, M., Reddy, T., Cournapeau, D., et al.

912   (2020). SciPy 1.0: fundamental algorithms for scientific computing in Python. *Nature*

913   *Methods*, *17*(3), 261–272. https://doi.org/10.1038/s41592-019-0686-2

914   Winsemius, H. C., Aerts, J. C. J. H., van Beek, L. P. H., Bierkens, M. F. P., Bouwman, A.,

915   Jongman, B., et al. (2016). Global drivers of future river flood risk. *Nature Climate*

916   *Change*, *6*(4), 381–385. https://doi.org/10.1038/nclimate2893

917   Wunsch, A., Liesch, T., & Broda, S. (2022). Deep learning shows declining groundwater levels

918   in Germany until 2100 due to climate change. *Nature Communications*, *13*(1), 1221.

919   https://doi.org/10.1038/s41467-022-28770-2

920   Xia, Y., Mitchell, K., Ek, M., Sheffield, J., Cosgrove, B., Wood, E., et al. (2009). NLDAS Primary

921   Forcing Data L4 Hourly 0.125 x 0.125 degree V002 (NLDAS_FORA0125_H) [Data set].

922   Goddard Earth Sciences Data and Information Services Center (GES DISC).

923   https://doi.org/10.5067/6J5LHHOHZHN4

924   Xia, Y., Mitchell, K., Ek, M., Sheffield, J., Cosgrove, B., Wood, E., et al. (2012). Continental-

925   scale water and energy flux analysis and validation for the North American Land Data

926   Assimilation System project phase 2 (NLDAS-2): 1. Intercomparison and application of

927   model products. *Journal of Geophysical Research: Atmospheres*, *117*(D3).

928   https://doi.org/10.1029/2011JD016048

929   Xiang, Z., Yan, J., & Demir, I. (2020). A rainfall-runoff model with LSTM-based sequence-to-

930   sequence learning. *Water Resources Research*, *56*(1), e2019WR025326.

931   https://doi.org/10.1029/2019WR025326

932   Ye, A., Zhou, Z., You, J., Ma, F., & Duan, Q. (2018). Dynamic Manning's roughness coefficients

933   for hydrological modelling in basins. *Hydrology Research*, *49*(5), 1379–1395.

934   https://doi.org/10.2166/nh.2018.175

935   Zhi, W., Feng, D., Tsai, W.-P., Sterle, G., Harpold, A., Shen, C., & Li, L. (2021). From

936   hydrometeorology to river water quality: Can a deep learning model predict dissolved

937   oxygen at the continental scale? *Environmental Science & Technology*, *55*(4), 2357–

938   2368. https://doi.org/10.1021/acs.est.0c06783

939   Zhu, F., Li, X., Qin, J., Yang, K., Cuo, L., Tang, W., & Shen, C. (2021). Integration of

940   multisource data to estimate downward longwave radiation based on deep neural

941   networks. *IEEE Transactions on Geoscience and Remote Sensing*, 1–15.

942   https://doi.org/10.1109/TGRS.2021.3094321
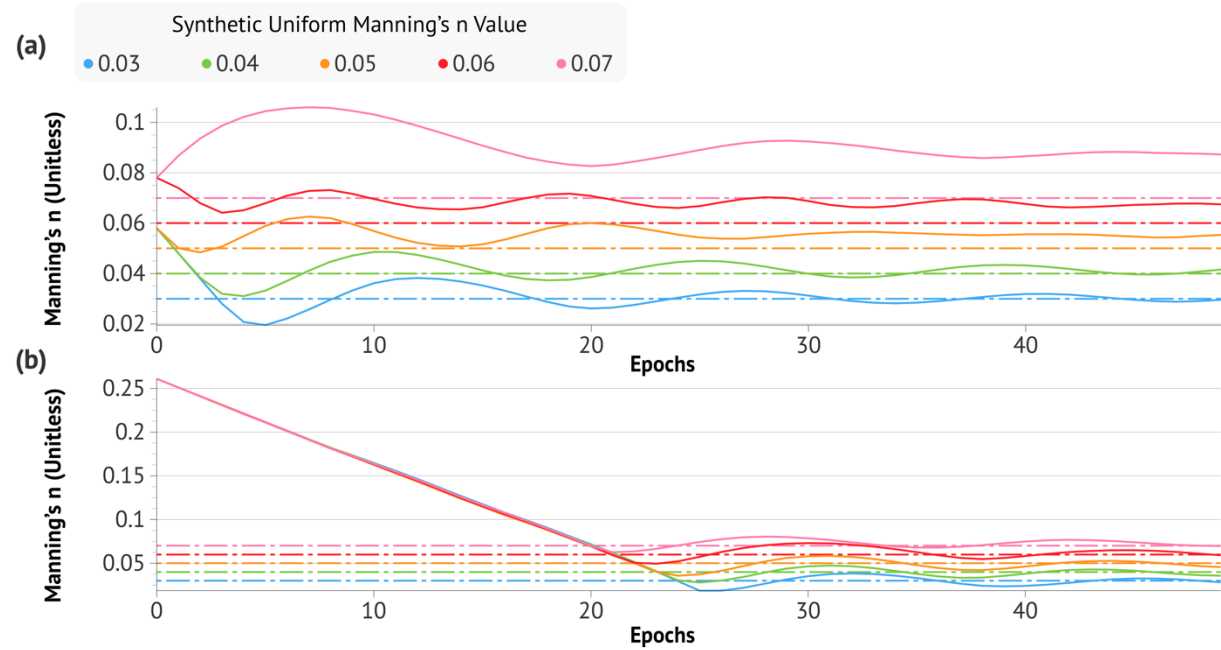
943

Appendix

Figure A1: The synthetic parameter recovery of Manning's *n* after each epoch run, with each colored line representing a different recovered value. (a) The initial value of *n* is set to 0.068 (b) the initial value of *n* is set to 0.271
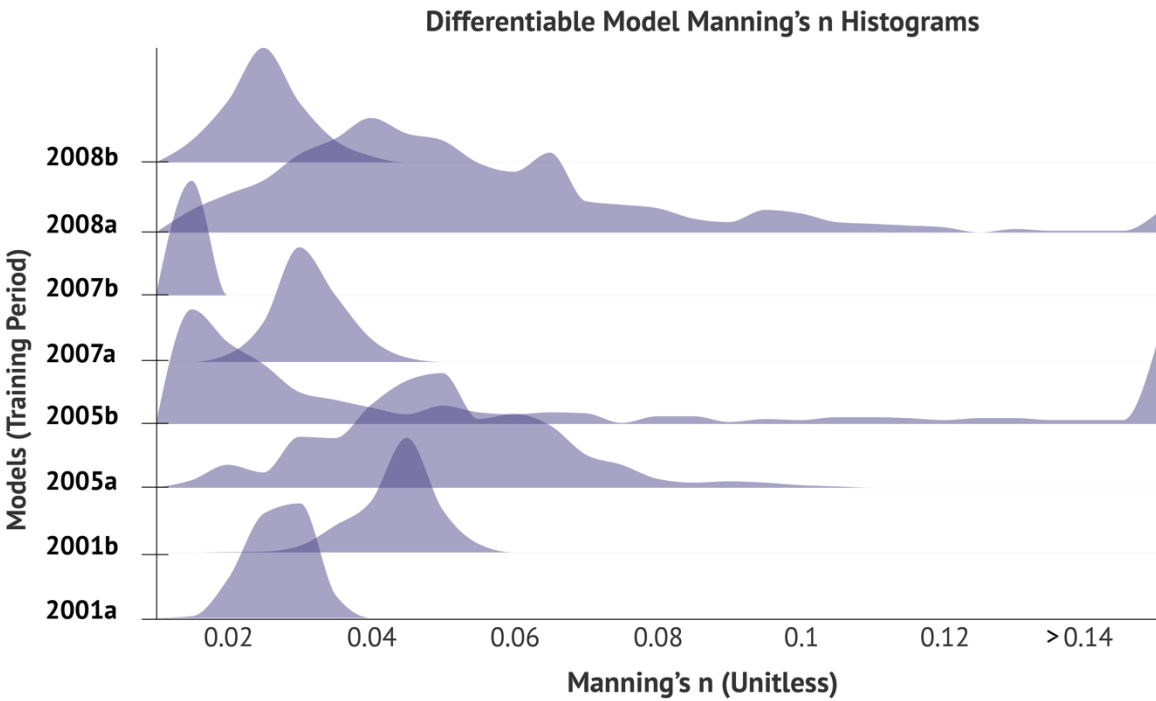
952   Figure A2: Histograms visualizing the frequency, and variability, of Manning's *n* values for all river

953   reaches (582 total) for all eight GNN models. The lower bound is 0.01, while the upper bound contains
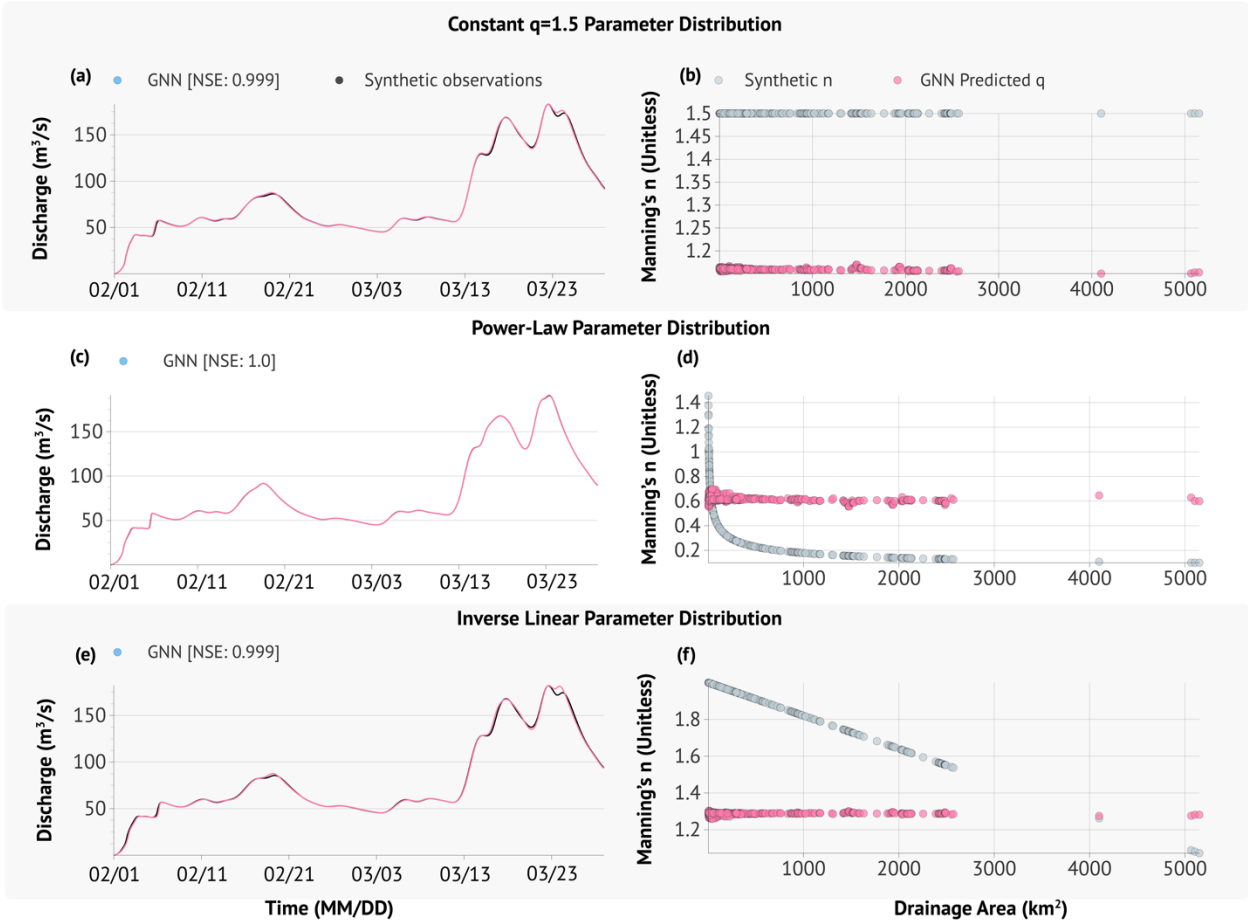
954   all Manning's *n* values >0.14.

955

956

957   Figure A3: Results from *q* parameter recovery experiments. We tried to recover both constant and

958   distributed parameters, but were unable to ever recover the synthetic truth.

959

960   Table A1: The attributes and forcings used by the pre-trained LSTM to predict streamflow. Links to the
961   data can be found below the table

Attribute/Meteorological Forcing	Unit	Dataset	Citation
Mean Elevation	m	SRTMGL1	(Carabajal & Harding, 2006)
Mean Slope	unitless	SRTMGL1	(Carabajal & Harding, 2006)

Basin Area	km^2	SRTMGL1	(Carabajal & Harding, 2006)
Dominant Land Cover	Class	MODIS	(Friedl & Sulla-Menashe, 2019)
Dominant Land Cover Fraction	Percent	MODIS	(Friedl & Sulla-Menashe, 2019)
Forest Fraction	Percent	MODIS	(Friedl & Sulla-Menashe, 2019)
Root Depth (50)	m	MODIS	(Friedl & Sulla-Menashe, 2019)
Soil Depth	m	MODIS	(Friedl & Sulla-Menashe, 2019)
Ksat (0-5)	$\log_{10}$(cm/hr)	POLARIS	(Chaney et al., 2019)
Ksat (5-15)	$\log_{10}$(cm/hr)	POLARIS	(Chaney et al., 2019)
Theta s (0-5)	m^3/m^3	POLARIS	(Chaney et al., 2019)
Theta s (5-15)	m^3/m^3	POLARIS	(Chaney et al., 2019)
Theta r (5-15)	m^3/m^3	POLARIS	(Chaney et al., 2019)
Ksat average (0-15)	$\log_{10}$(cm/hr)	POLARIS	(Chaney et al., 2019)
Ksat e (0-5)	cm/hr	POLARIS	(Chaney et al., 2019)

Ksat e (5-15)	cm/hr	POLARIS	(Chaney et al., 2019)
Ksat average e (0-15)	cm/hr	POLARIS	(Chaney et al., 2019)
Theta average s (0-15)	$e^{m3/m3}$	POLARIS	(Chaney et al., 2019)
Theta average r (0-15)	$e^{m3/m3}$	POLARIS	(Chaney et al., 2019)
Porosity	Percent	GLHYMPS	(Huscroft et al., 2018)
Permeability Permafrost	m^2	GLHYMPS	(Huscroft et al., 2018)
Permeability Permafrost (Raw)	m^2	GLHYMPS	(Huscroft et al., 2018)
Major Number of Dams	Unitless	GAGES-II	(Falcone, 2011)
General Purpose of Dam	Unitless	National Inventory of Dams (NID)	(US Army Corps of Engineers, 2018)
Max of Normal Storage	Acre-ft	National Inventory of Dams (NID)	(US Army Corps of Engineers, 2018)
Standard Deviation of Normal Storage	Unitless	National Inventory of Dams (NID)	(US Army Corps of Engineers, 2018)
Number of dams within river (2009)	Unitless	GAGES-II	(Falcone, 2011)
Normal Storage (2009)	Acre-ft	National Inventory of Dams (NID)	(US Army Corps of Engineers, 2018)
Precipitation hourly total	kg/m^2	NLDAS2	(Xia et al., 2012)
Surface downward longwave radiation	W/m^2	NLDAS2	(Xia et al., 2012)

Surface downward shortwave radiation	W/m^2	NLDAS2	(Xia et al., 2012)
Pressure	Pa	NLDAS2	(Xia et al., 2012)
Air Temperature	K	NLDAS2	(Xia et al., 2012)

962
963 SRTMGL1: https://doi.org/10.14358/PERS.72.3.287
964 MODIS: https://modis.gsfc.nasa.gov/data/dataprod/mod12.php
965 POLARIS: https://doi.org/10.1029/2018WR022797
966 GLHYMPS: https://doi.org/10.5683/SP2/DLGXYO
967 NID: https://nid.usace.army.mil/
968 NLDAS2: https://ldas.gsfc.nasa.gov/nldas/v2/forcing
969
970 Table A2: The constant attributes (c) used by the MLP to predict *n* and *q: n,q = NN(c)*.

Attribute	Unit
Reach Width	m
Average-Reach Elevation	m
Slope	m/m
Reach Area	km^2
Total Drainage Area	km^2
Reach Length	m
Sinuosity	m/m
Bank Elevation	m

971

972 Table A3: The Σ Q` ($\tau = 9$) NSE scores for all eight training time periods for the most downstream gage.
973 Since Q` routing is a pure forward simulation using the trained LSTM, we report the NSE values for each
974 period.
975

	Periods							
	2001a	2001b	2005a	2005b	2007a	2007b	2008a	2008b
NSE	0.5958	0.3534	-0.7868	-0.1687	0.6830	0.0558	-0.4297	0.3792

Figure 1.

(a)

SRB HUC10 Basin Data

GAGES-II Basin Data

Meteorological Forcings

USGS Observations

LSTM

Lateral Reach Inputs

River Graph

River Attributes

NN

River Parameters

Differentiable Muskingum Cunge

(b)

Figure 2.

(a)

01557500
01558000
01559000
01556000
01563200
01563500
01562000
01560000

Legend

Inner USGS Gages

Output USGS Gage

Graph River Network

Juniata River Basin
HUC10s

data.pa.gov, Esri, HERE, Garmin, SafeGraph, FAO, METI/NASA, USGS, EPA, NPS, Esri, CGIAR, USGS

0 8 16   32   48   64
Kilometers

(b)

Frequency

CDF

HUC10 Drainage Area (km²)

Figure 3.

Constant n=0.04 Parameter Distribution

(a) GNN [NSE: 0.999] Synthetic observations

(b) Synthetic n GNN Predicted n

Constant n=0.08 Parameter Distribution

(c) GNN [NSE: 1.0]

(d)

Power-Law Parameter Distribution

(e) GNN [NSE: 1.0]

(f)

Inverse Linear Parameter Distribution

(g) GNN [NSE: 0.999]

(h)

Time (MM/DD)

Drainage Area (km²)

Figure 4.

Model Training

● Observations	● GNN [NSE: 0.832]	● Q` [NSE: 0.596]

(a)

Model Testing

● Observations	● GNN [NSE: 0.856]	● Q` [NSE: 0.756]

(b)

Time (MM/DD)

Figure 5.

(a)

(b)
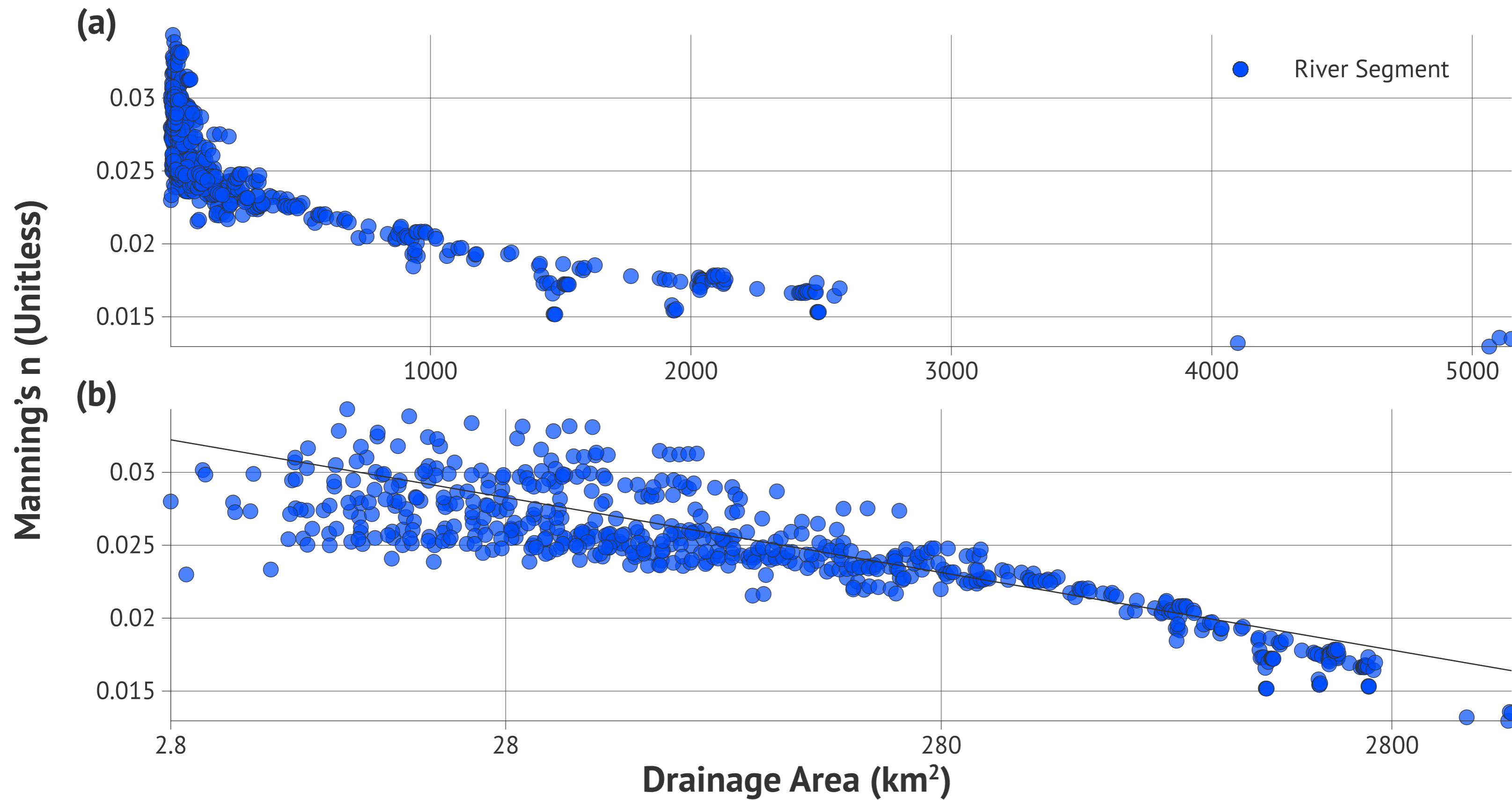
Manning's n (Unitless)

Drainage Area (km²)

River Segment

Figure 6.

(a) 2005 and 2007 Model Training Periods

● 2005 Observations
● Model 2005b [NSE: 0.897]

● 2007 Observations
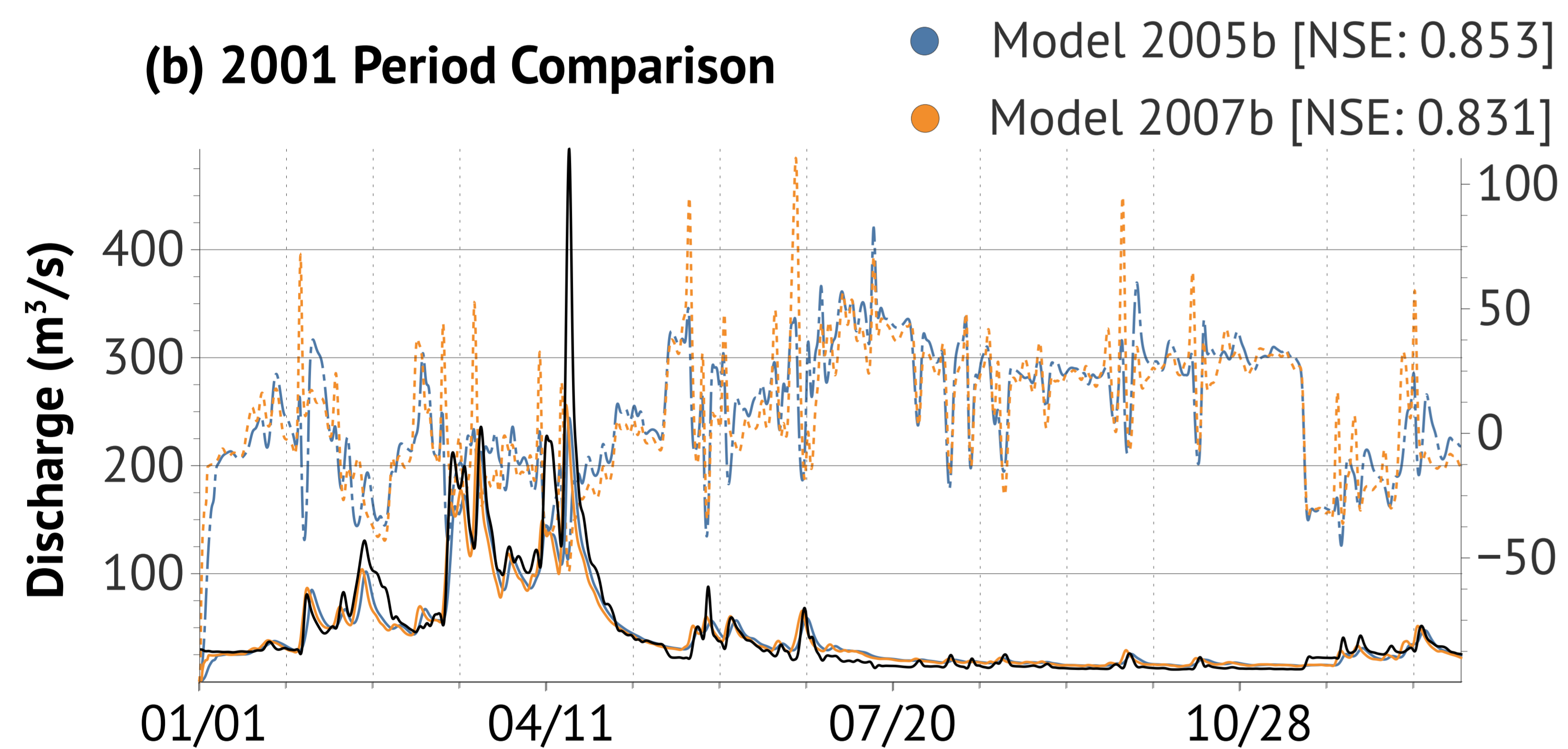● Model 2007b [NSE: 0.039]

Testing Period Model Comparison

● Observations   ○ Model 2005b Percent Error   ○ Model 2007b Percent Error

(b) 2001 Period Comparison
● Model 2005b [NSE: 0.853]
● Model 2007b [NSE: 0.831]

(d) 2007 Period Comparison
● Model 2005b [NSE: 0.827]
● Model 2007b [NSE: 0.774]

(c) 2005 Period Comparison
● Model 2005b [NSE: 0.870]
● Model 2007b [NSE: 0.713]

(e) 2008 Period Comparison
● Model 2005b [NSE: 0.762]
● Model 2007b [NSE: 0.534]

Figure A1.

Figure A2.

Differentiable Model Manning's n Histograms

Figure A3.

Constant q=1.5 Parameter Distribution

(a) GNN [NSE: 0.999] Synthetic observations

(b) Synthetic n GNN Predicted q

Power-Law Parameter Distribution

(c) GNN [NSE: 1.0]

(d)

Inverse Linear Parameter Distribution

(e) GNN [NSE: 0.999]

(f)

Discharge (m³/s)

Manning's n (Unitless)

Time (MM/DD)

Drainage Area (km²)

1 **Improving large-basin river routing using a differentiable Muskingum-Cunge model and physics-**
2 **informed machine learning**
3
4
5 Tadd Bindas[1], Wen-Ping Tsai[2], Jiangtao Liu[1], Farshid Rahmani[1], Dapeng Feng[1], Yuchen Bian[3], Kathryn
6 Lawson[1], Chaopeng Shen*[,1]
7
8 [1] Civil and Environmental Engineering, The Pennsylvania State University, PA
9 [2] Hydraulic and Ocean Engineering, National Cheng Kung University, Tainan City
10 [3] Amazon Search, Palo Alto, CA
11
12 * Corresponding author: Chaopeng Shen, <u>cshen@engr.psu.edu</u>
13
14   **Abstract**
15 Recently, rainfall-runoff simulations in small headwater basins have been improved by methodological
16 advances such as deep neural networks (NNs) and hybrid physics-NN models --- particularly, a genre
17 called differentiable modeling that intermingles NNs with physics to learn relationships between
18 variables. However, hydrologic routing, necessary for simulating floods in stem rivers downstream of
19 large heterogeneous basins, had not yet benefited from these advances and it was unclear if the routing
20 process can be improved via coupled NNs. We present a novel differentiable routing model that mimics
21 the classical Muskingum-Cunge routing model over a river network but embeds an NN to infer
22 parameterizations for Manning's roughness (n) and channel geometries from raw reach-scale attributes
23 like catchment areas and sinuosity. The NN was trained solely on downstream hydrographs. Synthetic
24 experiments show that while the channel geometry parameter was unidentifiable, n can be identified
25 with moderate precision. With real-world data, the trained differentiable routing model produced more
26 accurate long-term routing results for both the training gage and untrained inner gages for larger
27 subbasins (>2,000 km^2) than either a machine learning model assuming homogeneity, or simply using
28 the sum of runoff from subbasins. The n parameterization trained on short periods gave high
29 performance in other periods, despite significant errors in runoff inputs. The learned n pattern was
30 consistent with literature expectations, demonstrating the framework's potential for knowledge
31 discovery, but the absolute values can vary depending on training periods. The trained n
32 parameterization can be coupled with traditional models to improve national-scale flood simulations.
33
34 Main points:
35   1. A novel differentiable routing model can learn effective river routing parameterization,
36   recovering channel roughness in synthetic runs.
37   2. With short periods of real training data, we can improve streamflow in large rivers compared to
38   models not considering routing.
39   3. For basins >2,000 km^2, our framework outperformed deep learning models that assume
40   homogeneity, despite bias in the runoff forcings.

1. Introduction

Riverine floods pose a major risk to human safety and infrastructure (Douben, 2006; François et al., 2019; International Panel on Climate Change (IPCC), 2012; Koks & Thissen, 2016) and are linked to stream channel characteristics. Riverine floods along large stem rivers occur when the peak flow rate exceeds the stem river conveyance capacity. The timing of flood convergence and peak flood rates are influenced by the channel's geometries and flow resistance properties (Candela et al., 2005; Kalyanapu et al., 2009). In recent years, we have witnessed many deadly riverine floods, e.g., in the Mississippi River, USA (Rice, 2019) and India (France-Presse, 2022), with such disasters expected to rise significantly based on future climate projections (Dottori et al., 2018; Prein et al., 2017; Winsemius et al., 2016). The ability to better account for flood convergence and streamflow processes is urgently needed to help us better inform society of stem river flood magnitudes and timing.

In hydrologic modeling, routing describes how the stream network conveys runoff downstream while accounting for mass balances and the speed of flood wave propagation (Mays, 2010). Most routing models are based on the principle of continuity (or mass conservation) but they differ in how the momentum equation or flow velocity is calculated. For example, the widely-applied Muskingum-Cunge (MC) (Cunge, 1969) routing method is a center-in-space center-in-time finite difference solution to the continuity equation, assuming a prismatic flood wave as the constitutive relationship to simplify the momentum equation. In some other cases, the momentum equation is solved in conjunction with the continuity equation (Ji et al., 2019) with a range of simplifying assumptions, e.g., ignoring inertia (Shen & Phanikumar, 2010), ignoring both inertia and pressure gradient (only slope remaining) (Mizukami et al., 2016), or including additional formulations to handle effects of scale, e.g., Li et al. (2013). In each case, these models have parameters that need to be determined from lookup tables or calibration, e.g., roughness parameters that serve as resistance to flow.

Although routing parameters often rank among the important ones for discharge simulation (Khorashadi Zadeh et al., 2017; L. Liu et al., 2022), they been difficult to parameterize at large scales, especially in a way to both sensibly represent basin-internal spatial heterogeneity and adapt to discharge data. Using traditional roughness values tabulated for various land covers (Arcement & Schneider, 1989) requires in-situ scouting, e.g., to determine if channels have pools, weeds, grass, etc., which is currently impractical for large-scale applications. Many calibration exercises (Khorashadi Zadeh et al., 2017; L. Liu et al., 2022;

73   Mizukami et al., 2016) have used only one set of parameters for an entire basin, neglecting fine-scale

74   spatial heterogeneity in river-reach characteristics. Some studies have employed Manning's roughness,

75   *n* (a coefficient representing a channel's resistance to flow), as a linear function of river depth or other

76   characteristics (Getirana et al., 2012; H.-Y. Li et al., 2022), but it is unclear if these relationships

77   accurately represent the available data.

78

79   While the accuracy of basin rainfall-runoff models has improved substantially in recent years with

80   machine learning (ML) (Adnan et al., 2021; Feng et al., 2020; Kratzert et al., 2019; Sun et al., 2022; Xiang

81   et al., 2020), these methods have not been applied to routing modules in order to benefit the simulation

82   of stem river floods. Neural networks (NNs) like long short-term memory (LSTM), GraphWaveNet (Sun et

83   al., 2021), or convolutional networks (Duan et al., 2020) have demonstrated their prowess in learning

84   hydrologic dynamics from big data. They are applicable not only to streamflow hydrology but also to

85   variables across the entire hydrologic cycle (Shen, Chen, et al., 2021; Shen & Lawson, 2021) such as soil

86   moisture (Fang et al., 2017, 2019; J. Liu et al., 2022; O & Orth, 2021), groundwater (Wunsch et al., 2022),

87   snow (Meyal et al., 2020), longwave radiation (Zhu et al., 2021), and water quality parameters like water

88   temperature, dissolved oxygen and nitrogen (He et al., 2022; Hrnjica et al., 2021; Lin et al., 2022;

89   Rahmani, Lawson, et al., 2021; Saha et al., 2023; Zhi et al., 2021). However, these approaches are mostly

90   suitable for relatively homogeneous headwater basins; spatial heterogeneities in forcings and basin

91   characteristics are generally not well represented in these approaches. In our previous studies we

92   observed that large basins often turned out to have poorer performance for LSTM models. The routing

93   module is the key component that allows us to consider how runoff from heterogeneous subbasins

94   converge and contribute to the stem river floods, and could be extended to support reactive transport

95   modeling in the river network.

96

97   A recent development in integrating ML with physical understanding is the use of differentiable, physics-

98   informed machine learning models, which can approach the performance of purely data-driven ML

99   models but also provide interpretable fluxes and states (Feng, Liu, et al., 2022). "Differentiable" models

100   can rapidly and accurately compute the gradients of the model outputs with respect to any input,

101   enabling the combined training of NNs to approximate complex or unknown functions from big data

102   while keeping physical priors. Such models can be simply supported by automatic differentiation (AD),

103   which tracks each elementary operation of tensors through the use of a computational graph, then uses

104   derivative rules to compute the gradient of each tensor operation (Baydin et al., 2018). This enables

105   hybrid frameworks to learn and incorporate complex and potentially unknown functions from big data

106   while retaining physical formulations. By connecting deep networks to reimplemented process-based

107   models (or their NN surrogates), Tsai et al. (2021) developed a NN-based parameterization pipeline that

108   infers physical parameters for process-based models. Differentiable models can also extrapolate better

109   in space and time than purely data-driven deep networks (Feng, Beck, et al., 2022). These methods are

110   also applicable to estimating parameters in ecosystem modeling (Aboelyazeed et al., 2022), and allow us

111   to flexibly discover variable relationships within the model based on big data, enabling improved

112   transparency compared to standard deep learning models.

113

114   Nevertheless, it was unclear if differentiable modeling could effectively learn relationships in a highly

115   complex river network, which convolves and integrates processes over large scales and thus render

116   small-scale processes unidentifiable. The river network forms a hierarchical graph, which is not unlike

117   the graph networks for applications like social recommendations (Fan et al., 2019), but with a

118   predefined spatial topology (due to a fixed river network) and a converging cascade. A complex river

119   graph can have many nodes, which, when coupled with many time steps, could potentially lead to a

120   training issue known as the vanishing gradient (Hochreiter, 1998), where the gradients with respect to

121   the parameters are vanishingly small and the system becomes very difficult to train. Moreover, runoff

122   data (required as an input for routing) are generally not available seamlessly for all subbasins and must

123   be estimated by models, but models for runoff could incur substantial errors. It was unclear if the

124   routing parameters could be learned, given such errors. It was further unclear if downstream discharge

125   data alone has enough information to enable learning of reach-scale relationships. In other words, a

126   reach-scale relationship may or may not be identifiable using downstream observations which integrate

127   the signals from the entire catchment area.

128

129   In this work, we developed a novel differentiable modeling framework to perform routing and to learn a

130   "parameterization scheme" (a systematic way of inferring parameters from more rudimentary

131   information) for routing flows on the river network. Such a physically-based routing method has never

132   been combined with NNs before. A NN-based parameterization scheme for Manning's n and river

133   bathymetry shape (q) is integrated with MC routing and is applied throughout the river network to

134   provide improved understanding of both the model and the modeled system. We designed synthetic

135   and real data experiments to answer the following research questions:

136   1. *Given substantial errors with estimated runoff as inputs to the routing module, can we learn*
137   *effective routing parameterization schemes that can produce reliable results for long-term*
138   *simulations in large river networks?*
139   2. *Does the learned parameterization perform well for both trained and untrained internal gages*
140   *and how does the performance vary as a function of basin area?*
141   3. *Do short periods of downstream discharge contain sufficient information to train a reliable*
142   *parameterization scheme or to identify the parameterization for channel roughness and*
143   *hydraulic geometries?*

144
145   **2. Data and Methods**

146   *2.1 Overview*

147   As an overview, we describe a differentiable model that routes runoff through a river network (or
148   "graph" in the ML terminology) similar to the traditional Muskingum-Cunge (MC) method. But unlike the
149   traditional MC, our differentiable model is able to incorporate and train neural networks to provide
150   reach-scale parameterization. This new routing model can be perceived as a physics-informed graph
151   neural network (GNN) from an ML perspective. The nodes of the graph are spaced ~2000 m apart to
152   ensure stability. We trained an embedded a Multilayer Perceptron (MLP) NN to generate spatially-
153   distributed river parameters for each reach (or "edge" in the GNN terminology) in the river network
154   (Figure 1b). The loss function (the model's goal is to minimize the output of this) was calculated at the
155   furthest downstream node of the graph. To disentangle rainfall-runoff (required information for routing)
156   from the routing processes, lateral inflow of combined overland and groundwater flow was obtained
157   from a pre-trained LSTM streamflow prediction model (reported in previous work). The runoff values
158   were then disaggregated to hourly time steps via interpolation and routed throughout the river network
159   using the proposed differentiable routing model (Figure 1a). We provide the details in the subsections
160   that follow.
161

162

163
164

Figure 1: (a) An abstract overview of how inputs move through our workflow to eventually be run

through the differentiable MC function. MC utilizes lateral flow inputs based on LSTM predictions, NN

predicted river parameters n and q, and other river attributes to generate predictions. (b) An illustration

of how we traverse the graph (dark blue circles) using MC to make a discharge prediction for the final

node (orange circle).

170

171 *2.2 The River Graph*

172 We constructed a river network (or graph) for the Juniata River Basin (JRB) in the northeastern United

173 States (Figure 2), by processing the United States Geological Survey's (USGS's) National Hydrography

174 Dataset (NHDplus v2) (HorizonSystems, 2016; Moore & Dewald, 2016) which provide topology and some

175 attributes of the river reaches such as upstream catchment area. We ensured stability of the MC scheme

176 by discretizing the river network into approximately 2-km reaches, resulting in 544 junction points (or

177 nodes) and 582 river reaches (or edges). These reaches are where the physical parameters like

178 Manning's roughness and channel shape coefficients are defined. To reduce computational demand, we

179 selected a subset of NHDplus v2 river reaches based on a stream density threshold (total stream

180 length/watershed area), choosing rivers with the longest length until a stream density of 0.2 km/km^2

181 was reached. We then calculated slope and sinuosity for the reaches by overlaying NHDplus v2 with 10-

182 m resolution digital elevation data (USGS ScienceBase-Catalog, 2022). Prior work describes the bulk of

183 the extraction procedure that prepares input data for a physically-based surface-subsurface processes

184 model (Ji et al., 2019; Shen et al., 2013, 2014, 2016; Shen & Phanikumar, 2010).

185

186 The hydrograph at the furthest downstream JRB gage, USGS gage 01563500 (node 4809 in our graph) on

187 the Juniata River at Mapleton Depot, PA, was chosen as the training target (Figure 2a). This gage has a

188 catchment area of 5,212 km^2 contributed from the 582 simulated reaches upstream. Seven USGS gages

189 are located upstream of this node which enables further validation of the simulations.

190

191

192
193
194

Figure 2: (a) A map of the Juniata River Basin's (JRB's) river network and HUC10 watersheds. Each eight-
195
digit number corresponds to a USGS gage. (b) A histogram showing the distribution of HUC10
196
watersheds in the JRB. The x-axis shows the distribution of the HUC10 watershed area in square
197
kilometers. The left y-axis shows the number of HUC10s that fall within the area ranges (corresponding
198
with the blue bars), and the right y-axis shows a cumulative density function (CDF) distribution of the
199
areas, corresponding with the red dashed line.
200

201

202   *2.3 Implementing River Routing with Muskingum-Cunge*

203   *2.3.1 Muskingum-Cunge*

204   The Muskingum-Cunge (MC) method is a widely-used flood routing technique that combines the

205   Muskingum storage routing concept with the continuity and momentum equation for a river reach

206   (Cunge, 1969), solved using a center-in-space, center-in-time finite difference scheme for each reach, at

207   time steps *t* and *t+1:*

$$Q_{t+1} = c_1 I_{t+1} + c_2 I_t + c_3 Q_t + c_4 Q' \tag{1}$$

$$c_1 = \frac{\Delta t - 2KX}{2K(1-X) + \Delta t} \tag{2}$$

$$c_2 = \frac{\Delta t + 2KX}{2K(1-X) + \Delta t} \tag{3}$$

$$c_3 = \frac{2K(1-X) - \Delta t}{2K(1-X) + \Delta t} \tag{4}$$

$$c_4 = \frac{2\Delta t}{2K(1-X) + \Delta t} \tag{5}$$

208   Where I_t and Q_t are the inflow and outflow of the reach at time step t, respectively, and I_{t+1} and Q_{t+1}

209   are the inflow and outflow at the next time step, *t+1*. *K* represents travel time based on reach length

210   and wave celerity, *X* is a dimensionless inflow/outflow weighing parameter, and *Q'* represents lateral

211   inflow of the incremental catchment area of the reach, and can also include tributary inflows. We

212   adopted the simple linear form of the Muskingum equation: X is constant and K= $\Delta x / v$ where Δx is

213   length of the reach and v is the discharge velocity (m/s) of the current time step. More complex

214   nonlinear forms of the MC equation could be tested in the future (Mays, 2019). To simulate a river

215   network, we divide the network into a series of reaches to route the flow of water from upstream to

216   downstream. The outflow from a reach is the inflow of the next downstream reach.

217

218   *2.3.2 MC parameter values and variable channel dimensions*

219   To implement MC, we chose an hourly time step (*Δt*) and a weighing coefficient (*X)* of 0.3, which was

220   based on regional expectations, for Equations 2-5. Since discharge velocity *v* and stream top width *w*

221   vary over time, they need to be updated in each time step with respect to discharge *Q*, which was done

222   here with the help of a constitutive relationship used to close the equations. For this, because at-a-site

223 hydraulic geometries (Gleason, 2015; Leopold & Maddock, 1953) leads to a power-law relation between

224 top width (w [m]) and depth (d [m]), we can assume such a relationship:

$$w = pd^q \tag{6}$$

225 where p [m] and q [-] are linear and exponential parameters, respectively, that are potentially spatially

226 heterogeneous and represent the shape of the channel's cross-sectional area. For a rectangular channel,

227 q=0, and for a triangular channel, q=1. The cross-sectional area A_{CS} is the integral of w with respect to d

228 (Equation 7). To simplify the task (and because it is not sensitive based on our observations), we

229 assumed p=21 based on preliminary data fitting to USGS hydraulic geometries from field surveys of

230 gages in the JRB. Note that even though we make this assumption here for model completeness, we do

231 not posit that q is invertible from available data because it may not be that significant for the

232 downstream discharge. Moving forward with these assumptions, we can write these relationships as

233 Equation 7:

$$A_{CS} = \int_0^d w\, \partial d = \int_0^d pd^q\, \partial d = \frac{pd^{q+1}}{q+1} \tag{7}$$

234 Combining Equation 7 with Manning's n Equation, we come up with Equation 8a. Reorganizing, we

235 derive a function that estimates d from Q (Equation 8b). With d, p, and q, we can estimate v and K using

236 the linear form of Muskingum equation as in Equations 7, 8c, and 8d which close the equations.

$$Q = vA_{CS} = \frac{1}{n}R^{2/3}S_0^{\frac{1}{2}}\frac{pd^{q+1}}{q+1} = \frac{pd^{q+\frac{5}{3}}S_0^{\frac{1}{2}}}{n(q+1)} \tag{8a}$$

$$d = \left[\frac{Q_t n(q+1)}{pS_0^{\frac{1}{2}}}\right]^{\frac{3}{5+3q}} \tag{8b}$$

$$v = \frac{Q_t}{A_{CS}} \tag{8c}$$

$$K = \frac{\Delta x}{v} \tag{8d}$$

237 Here, S_0 represents the reach slope, Q_t represents the discharge exiting the reach at time t, and Δx is

238 the reach length.

239

240 *2.3.3 Differentiable modeling*

241   By implementing MC on a differentiable coding platform (PyTorch, Tensorflow, Julia, etc.), we can train a

242   coupled NN in an "online" way to produce physical reach-scale river parameters for the routing model,

243   much like our earlier work in differentiable parameter learning (dPL) (Tsai et al., 2021). Here we include

244   a NN into the MC routing framework to optimize equation parameters based on big data while

245   maintaining physical consistency and mass balances. In this case, a Multilayer Perceptron (MLP) (Leshno

246   et al., 1993) is incorporated. The MLP, featuring two hidden layers and a sigmoid activation function in

247   the output layer, accepts a normalized array of attributes (c) for each reach (Table A2). Based on initial

248   results, we saw no need to add further complexity (additional hidden layers). The network then outputs

249   the Manning's roughness coefficient (n) and channel bathymetry shape coefficient (q):

$$n, q = NN(c) \tag{9}$$

250   where n represents a channel's resistance to flow and q represents the shape of the channel's cross-

251   sectional area. These parameters are inferred for each reach using the attributes of that reach prior to

252   routing, since we assumed n and q to be time-invariant. This produces r number of n and q values

253   specific to each reach for all timesteps where r is the number of river reaches. The weights of the MLP

254   are updated using backpropagation and the Adam optimizer (Kingma & Ba, 2017).

255

256   *2.4 Lateral streamflow inputs*

257   Since spatially-distributed runoff is needed to predict runoff in downstream basins, but there is no such

258   data, we employed a pretrained LSTM (Hochreiter & Schmidhuber, 1997) rainfall-runoff model. This

259   LSTM model was similar to those developed and reported in previous streamflow and water quality

260   studies (Feng et al., 2020; Ouyang et al., 2021; Rahmani, Lawson, et al., 2021; Rahmani, Shen, et al.,

261   2021), and we refer the reader to these publications for a more detailed description of these models.

262   After the initial training was done, we chose not to further update the LSTM in order to disentangle the

263   rainfall-runoff and routing parts of the modeling process, testing the robustness of the methodology in

264   the face of errors with simulated runoff. In addition, the test could tell us if other rainfall-runoff models

265   could be used instead. Updating LSTM further could lead to its co-adaptation with the routing module,

266   making the procedure complex.

267

268   To briefly summarize, the LSTM model used a combination of basin-averaged attributes, daily

269   meteorological forcings, and volumetric streamflow observations as inputs, and output daily basin

270   discharge. Meteorological forcings (total annual precipitation, downward long-wave radiation flux,

271 downward short-wave radiation flux, pressure, temperature) were obtained from the NASA NLDAS-2

272 Forcing Data set (Xia et al., 2009, 2012). We selected 29 basin attributes (Table A1 in the Appendix)

273 similar to those chosen in previous LSTM studies (Ouyang et al., 2021). Consistent with Ouyang et al.

274 (2021), we focused on training the LSTM on 3213 gages selected from the USGS Geospatial Attributes of

275 Gages for Evaluating Streamflow II (GAGES-II) dataset (Falcone, 2011) with input data between

276 1990/01/01 - 1999/12/31. We developed the workflow to obtain forcing data and inputs seamlessly for

277 any small basin in the conterminous United States (CONUS). In this case, we extracted data from HUC8

278 subbasins and HUC10 watersheds to gather inputs to train our LSTM model and predict discharge,

279 respectively.

280

281 When evaluated on the gaging stations in the study area, the model achieved a median daily Nash-

282 Sutcliffe Efficiency (NSE) (Nash & Sutcliffe, 1970) of 0.7849 for the eight gauging stations in the JRB.

283 After training during the period of 1990/01/01 – 1999/12/31, the model was run from 2000/01/01-

284 2009/12/31 to predict discharge for the 17 HUC10 watersheds in the study area:

$$Q' = LSTM(x_{HUC10}, A_{HUC10}) \tag{10}$$

285 where Q' [m^3/s] is the daily runoff for the HUC10 basin, and x_{HUC10} and A_{HUC10} are HUC10-averaged

286 atmospheric forcings and static attribute variables, respectively. Lastly, we computed a mass transfer

287 matrix, which tabulates the fraction of a subbasin draining into a river reach. Each row of the matrix is

288 obtained by dividing the incremental catchment area of reaches inside a subbasin by the total area of

289 that subbasin. Runoff can be distributed to river reaches via a simple matrix multiplication.

290

291 Due to the nature of the data used to train the LSTM, it could produce seamless (having no gaps) runoff

292 estimates for the JRB but only on a daily, not hourly, scale. Because MC routing needs to operate on

293 smaller time steps, we quadratically interpolated (Virtanen et al., 2020) daily data into hourly time steps,

294 where each daily measurement occurs at 12:00 hours. For training and evaluating the routing model, we

295 collected observed discharge data for nodes intersecting USGS GAGES-II monitoring stations. Only some

296 time periods of the most downstream gage station were used for training, and other stations were only

297 used for evaluation. The observed discharge data were similarly disaggregated to hourly data.

298

2.5 Inverse-routing and hyperparameters

300   There are time zone differences between the forcing data (recorded using UTC) and USGS streamflow

301   (recorded in UTC-5). To address this, we first shifted the LSTM-produced runoff outputs by 5 hours.

302   Because LSTM was trained to predict runoff at the outlet of a basin, with catchment area being an

303   impactful input to the model, it already implicitly considers the time of concentration to the outlet.

304   However, as our modeled river network extends into the subbasins and contains smaller rivers, the

305   routing module explicitly simulates the within-basin concentration process. Ideally, we can use an

306   inverse-routing approach to revert LSTM-predicted runoff to the time before it enters the river network.

307   However, as inverse-routing methods (Pan & Wood, 2013) can be quite involved and were not the focus

308   of the study, we opted for a simple approach that shifted the runoff back in time by τ hours. τ is

309   considered a hyperparameter. To avoid overfitting, we used the same τ value for all the subbasins and

310   all experiments, and determined this value by manually tuning based on the training period. We found

311   $\tau = 9$ (hours) to be a good choice. More complicated procedures could be employed in the future, but

312   this straightforward approach proved to be effective in our case.

313

314   Hyperparameters and training period sizes for our differentiable routing model were chosen through

315   repetitive trial and error based on the training period. These trials led us to choose a hidden size of 6 for

316   our MLP, and a training size of eight weeks. Parameters were tuned for 50 epochs for synthetic and real

317   data experiments. Mean Squared Error (MSE) was chosen as our loss function. Since our differentiable

318   model at t=0 assumes no inflow to the river network and relies exclusively on Q' for flow inputs, a period

319   of 72 hours is employed to "warm up" the model states in the river network, and the loss function and

320   NSE are not calculated within this period.

321

322   *2.6 Experiments*

323   *2.6.1 Synthetic Parameter Recovery*

324   We first ran multiple synthetic parameter recovery experiments to check if the dataset and the

325   framework could indeed recover assumed relationships with small training periods of eight weeks. Our

326   first experiment tested if we could correctly recover a single, spatially-constant set of assumed values

327   for both *n* and *q* for the whole river network, resulting in only two degrees of freedom. We assumed

328   ranges from 0.01 – 0.3 and 0-3 for the synthetic values of *n* and *q*, respectively, to give a realistic value

329   range for the MLP to learn parameters. *n* and *q* model parameters were initialized to be at the 90th and

330   20th percentiles for the first and second set of synthetic experiments, respectfully.

331

332 In our second experiment, we assumed constant *n* throughout the reaches but set the trained model as

333 *n,q = NN(c)* (Equation 9) so that the *n, q* values could be different from reach to reach. In this case,

334 ideally, the NN would learn to output a constant value regardless of the inputs.

335

336 Our third synthetic experiment examined if we could retrieve simple assumed relationships within

337 realistic literature bounds (inverse-linear or power-law) [Equation 9-10] between *n, q,* and drainage area

338 (DA), given that the MLP had far more inputs than just DA. The trained model is still utilizing Equation 9,

339 as we assumed we did not know the functional relationship *a priori.*

$$n = 0.06 - 8 \times 10^{-6}(DA) \qquad (11)$$
$$q = 2 - 0.00018(DA)$$

$$n = \frac{0.0915}{(DA)^{0.131}} \qquad (12)$$
$$q = \frac{2.1}{(DA)^{0.357}}$$

340 *2.6.2 Observational Data Experiments.*

341 We trained our differentiable model (updating the weights in NN as in equation 6) against observed

342 USGS data. We utilized eight-week training periods from different years and checked whether the

343 resulting parameters led to satisfactory routing in other years at both the training gage and untrained,

344 inner, gages. Training periods were selected based on times when the LSTM had high accuracy and when

345 there were frequent discharge peaks. Routing frequently fluctuating discharge through a river network

346 introduces more variance into the MLP, allowing it to perform better when testing over a longer time

347 period. Additionally, high LSTM accuracy reduces the noise --- we hypothesize the system has some

348 tolerance to the runoff errors but outsized errors can invalidate the model. Periods of such "high

349 flashiness" in the JRB occurred during both 02/01-03/29 and 11/01-12/26, while the years 2001, 2005,

350 2007, and 2008 had high LSTM accuracy, giving us eight time periods on which to train NN models. We

351 then trained the differentiable routing models on all eight selected time periods to determine the

352 sensitivity of the model performance to the selected training time period.

353

354 When interpreting model performance at inner gages, we compared results with the LSTM that modeled

355 the whole JRB as a uniform basin and a simple summation of the τ-shifted LSTM runoff inputs (Q'). We

356 also explored whether using a combination of inner gages, along with the furthest downstream gage,

357   inside of the loss function would improve model performance on all gages throughout the study area.

358   The gages used were USGS 01560000 (edge 1053) and 01563200 (edge 2689). Internal gages were

359   selected based on NSE metrics when using only the furthest-downstream gage in the loss calculation; we

360   chose basins with middle-level metrics so as to not overfit the model if using highly predictive internal

361   gages.

362

363   **3. Results and Discussion**

364   In the following, we first discuss our synthetic experiments (Section 3.1) which explore our routing

365   framework's potential to retrieve assumed parameters from our differentiable GNN. Next, we show the

366   results of confronting our model with LSTM-simulated runoff as observed streamflow at the furthest

367   downstream gage, expanding the training period to other time ranges, then applying our models to

368   different years for observation (Section 3.2). Furthermore, we discuss the stability of our trained models

369   over several years of testing (Section 3.3). Lastly, we analyze the n parameters recovered for the trained

370   models and discuss their implications (Section 3.4).

371

372   *3.1 Synthetic experiments*

373   Our first synthetic experiment (with constant parameters and only 2 degrees of freedom for the search)

374   recovered the assumed n values with moderate accuracy, but not the channel geometry parameter q

375   (Table 1). Recovered n values were within a small range of the assumed ones, with minor fluctuations,

376   while recovered q values mostly stayed similar the initial guesses, showing slight changes after a number

377   of iterations. This result was consistent across 10 runs, each with different "synthetic truth" values for n

378   and q. The training led n to the assumed values rapidly, typically within 20 epochs (Figure A1). The non-

379   identifiability of q was likely because q has only a small influence on the storage capacity of the stream

380   and the simulated discharge is not sensitive to q, making dL/dq (where L is the loss function) negligible.

381   While it is a pity that hydraulic geometry parameters cannot be estimated, the results also implied that

382   they would not influence the routing results noticeably. Thus, in our efforts, we focused on n.

383   *Table 1: Results from the constant synthetic n and q parameter recovery experiments*

Run	n			q		
	Initial Guess	Synthetic Truth	Recovered Parameter	Initial Guess	Synthetic Truth	Recovered Parameter
1	0.271	0.03	0.028	2.7	2	2.327

2	0.271	0.04	0.035	2.7	2	2.37
3	0.271	0.05	0.046	2.7	2.5	2.390
4	0.271	0.06	0.059	2.7	2.5	2.456
5	0.271	0.07	0.070	2.7	3	2.480
6	0.068	0.03	0.030	0.6	1.0	0.574
7	0.068	0.04	0.042	0.6	1.0	0.592
8	0.068	0.05	0.055	0.6	1.5	0.730
9	0.068	0.06	0.067	0.6	1.5	0.777
10	0.068	0.07	0.087	0.6	2.5	0.690

384

385 Our second synthetic experiment (assuming constant n to be recovered by NN(A)) showed that we were

386 able to recover the constant value that was set using an NN, but there was some scattering for the

387 headwater reaches (Figure 3c, 3f). We noticed trends associated with drainage area (DA), which is

388 correlated with reach positioning in the watershed; small DA often indicates a headwater reach, while

389 large DA often indicates a reach much further downstream. There were some visible differences

390 between the synthetic hydrographs resulting from different assumed n values (comparing Figures 3a

391 and 3c), which allowed the recovered n values to mostly center around the assumed value. However,

392 the scattering of points toward the lower-DA part of Figures 3b and 3d alluded to the fact that the

393 downstream discharge was strong enough to completely constraint on the model. n in different ranges

394 can fluctuate around the mean to generate essentially the same pattern as a constant n value.

395

396 In our third set of synthetic experiments, the simple functions could be roughly recovered for most of

397 the reaches, while there may have been increased uncertainty for the furthest downstream reaches

398 (Figure 3f & 3h). There were again noticeable differences in the hydrographs (Figures 3e & 3g) from

399 previous ones. When the power-law relationship was assumed, the hydrograph matched the synthetic

400 one almost completely (Figure 3e), and the estimated n outputs from the MLP overlapped to a great

401 extent with the value to be retrieved (Figure 3f). The headwater reaches (small-DA) showed a rapid

402 decline in n with respect to increasing DA. In the middle ranges of DA, the curve followed the assumed

403 one almost exactly. Toward the higher range of DA, the recovered values were lower than the assumed

404 relationship, but the deviation was not huge because the power-law formulation became flat in this

405   range. Based on the closeness of hydrographs in all of Figure 3, we do not anticipate that further

406   optimization can bring significant improvement to the estimations. Similar to the two-constant-

407   parameter retrieval experiment, the q parameter was not recoverable and thus is not shown here.

408

409   Based on these simple experiments, it seems training on the river graphs has some promise but also

410   some limitations. It is promising because it is likely that n is related to DA which is, to some extent,

411   recoverable. It is simultaneously challenging because, as a large number of reaches contribute to one

412   gage, it is an underdetermined system. This method was not able to fully reproduce the drastic change

413   in the low-DA range presumably because this sharp slope was inconsistent with the rest of the curve,

414   and NNs generally do not output extreme values. It also ran into difficulty toward the high-DA range

415   because there were simply far fewer reaches with large DA so their roles in routing were relatively

416   minor, making the curve unconstrained in this range. This experiment informed us we should not expect

417   values of reach-scale n, particularly in the high-DA range, to be reliable, but the overall trend may have

418   merit, especially when we also have other constraints. These findings formed the basis for the next

419   stage of the work where we trained n=NN($\mathbf{c}$) for real-world data. We thus expected to extract the overall

420   patterns of n distribution but for the recovered q not to be meaningful.

Figure 3: Synthetic discharge distribution experiments. (a, c, e, g) Synthetic and modeled discharge over time for various assumed relationships between n and drainage area. (b, d, f, h) Synthetic modeled values of n with respect to the reach's total drainage area (km^2). The NN can recover the overall pattern but is not accurate near sharp changes or for reaches with large drainage areas. Each dot in the scatter plots represents a 2-km river reach in the river network.

3.2. Training on eight weeks of real data

The real-world data experiment showed satisfactory streamflow routing in the training period, with improvements compared to approaches that did not employ the routing scheme, even though there

18

432   was significant bias in the rainfall input (Figure 4a). The hydrograph generated by the differentiable

433   routing model is, as expected, smoothed and delayed compared to the summation of runoffs during the

434   training period. Unlike the direct summation of the runoff, which has a timing difference from the

435   observation, the peaks of the routed hydrograph are placed almost exactly under the observed peaks,

436   leading to a high training NSE of 0.834. We noticed a substantial low bias in this training period,

437   witnessed by much lower peaks with the simulated flow compared to the observed flow. This is due to

438   bias in the rainfall-runoff modeling component and the mass-balance dictated by the MC formulation,

439   which prevents the model from adding or removing mass to remove the bias. In traditional hydrologic

440   model calibration, bias can be a significant concern as it can distorts other parameters. In this case, we

441   found the model performed well even with such bias, and appropriately focused on adjusting the timing

442   of the flood waves. This is because the allowable adjustments were limited to routing parameters, which

443   blocked the model from distorting other processes.

444
445

446   *Figure 4: (a) Results from training the differentiable model during an eight-week period (2001) against*

447   *USGS observations compared with the summation of lateral inputs (denoted by Q'). (b) Results from*

448   *testing the trained model from Figure 4(a) over a year period (2001) compared with the summation of*

449   *lateral inputs. A percent error has been overlaid to the graph to show how river routing is more stable*

450   *than using a summation of lateral inputs.*

451

452   The year-long test of the differentiable model yielded high metrics compared to the alternatives (Figure

453   4b), suggesting a short calibration period could yield parameterization suitable for long-term

454   simulations. The differentiable model obtained a year-long NSE of 0.857, which is consistent with the

455   median NSE in the JRB. In contrast, the summation of $Q'(\tau = 9)$ and the whole-basin $LSTM$ were at

456   0.756 and 0.801, respectively. This comparison shows that if we merely added the runoffs together

457   (which already resolved spatial heterogeneity in runoff but not the flow process), the error due to timing

458   could reduce NSE at the downstream gage. While the model had success with correctly timing the peak

459   flows, it could not compensate for LSTM's errors, resulting in significant underestimation of the peak

460   events. By design, the routing module should be detached from the errors in the runoff module.

461

462   Interestingly, without specific instructions, the scheme recovered a power-law-like relationship between

463   n and drainage area (DA) (Figure 5), similar to the one assumed in the synthetic case (Figure 3e &3f). The

464   n values were highest (near n=0.04) for smaller DA and declined gradually, approaching 0.015 at the

465   lower end. The change rate of n as a function of DA then became more gentle as DA increased. This

466   distribution agreed well with the general understanding that headwater streams running down ridges

467   (this region is characterized by Ridge and Valley formations) have larger slopes, higher roughness, more

468   vegetation, and thus higher n, while the high-order streams in the valley tend to have smaller slopes and

469   smoother beds, corresponding with lower n. In most hydrologic handbooks (Mays, 2019), a smaller n is

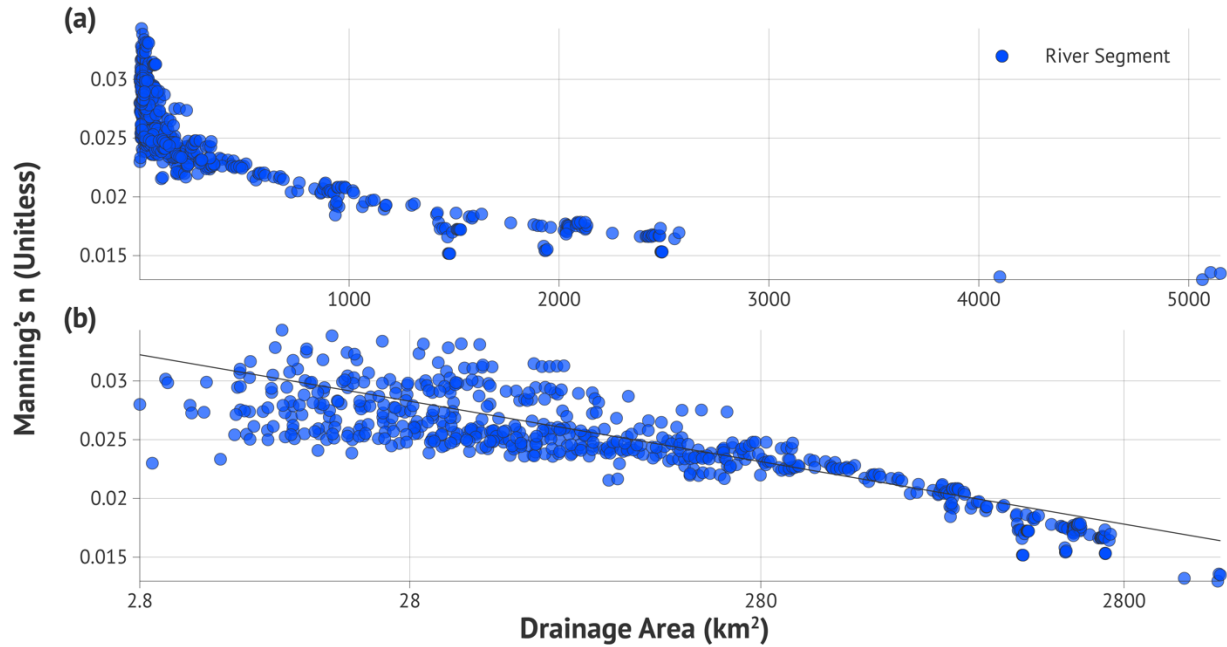470   prescribed for larger rivers.

471

Figure 5: The learned relationship between n and drainage area (square kilometers) for the Juniata River basin according to the trained GNN. (a) The distribution on a linear scale. (b) The distribution on a logarithmic scale. The network was trained for the period of 2001/02/01-2001/03/29. Each dot in the scatter plot represents a 2-km river reach.

3.3. Inner gage evaluation and effects of different training periods

Evaluating the model on the inner, untrained gages showed that the routing scheme became more competitive compared to benchmark levels as for downstream gages (Table 2). As for the benchmarks, the uniform LSTM (the catchment area of each gage is consider a basin and basin-averaged forcing/attributes were used as inputs to the trained LSTM to simulate flow at the gage) already attempts to consider routing internally but does not consider rainfall/attribute spatial heterogeneity, while the summation of Q' (runoffs were simulated from multiple HUC10 basins and added together) considers the spatial heterogeneity but not routing in the stem river. For 2 of the 4 gages with larger than ~2000 km^2 of catchment area, the differentiable routing model performed noticeably better than the uniform LSTM models for them (for the other two, they were about the same). For the three midsized subbasins (500-2000 km^2), the comparisons were mixed. For the small subbasins, and especially gage 01557500 (94.8 km^2), the uniform LSTM was noticeably better. The subbasin for 01557500 is smaller than our runoff-producing unit (HUC10s, with the smallest one ~200 km^2). This means predictions below this threshold can be error-prone. Our model was also better than the

21

492   summation of Q' for 7 of the 8 gages and the gap was larger for downstream gages (Table 2), suggesting

493   the flow convergence process matters more and more as we go downstream.

494

495   When we used multiple internal gages within the NN loss function, results improved very slightly at

496   smaller DA gages, while degraded barely noticeably at larger DA reaches. Overall, the differences are too

497   small to have real-world implications, but we can still observe the pattern that the multi-gage calibration

498   appears to produce a slightly more balanced model that improves simulations at some previously

499   weakly-simulated tributaries, at a (very minor) cost at the most downstream one. This small tradeoff

500   may be due to spatial errors in forcing data. As the model explicitly simulates flows in all modeled

501   reaches, the differentiable model provides a way to absorb data from as many stations as possible, if the

502   ungauged regions are important to the users.

503

504   *Table 2: Internal gage NSE values for the year 2001, with the rows ranked by the size of the subbasin*

505   *from small to large. The differentiable routing model was trained on the period from 2001/02/01-*

506   *2001/03/29 calculating loss from the final gage but the LSTM was trained using >3000 CONUS gages.*

507   *We include the LSTM NSE to show how the use of routing compares to just using LSTM predictions. Bold*

508   *font indicates the top performing model for each gage.*

Edge ID	Gage Number	Basin Drainage Area (km^2)	Uniform LSTM	Q` Runoff NSE (τ = 9)	Differentiable routing model (τ = 9)	Multiple Gage Loss for differentiable routing (τ = 9)
1280	01557500	94.8	**0.8149**	0.5575	0.5623	0.5627
1053	01560000	440.5	**0.7028**	0.6054	0.6578	0.6625
2799	01558000	542.1	**0.8201**	0.7473	0.6963	0.6981
4780	01556000	723.5	0.6624	0.6568	0.6937	**0.6957**
2662	01562000	1943.5	0.7957	0.6857	0.7942	**0.7977**
4801	01559000	2103.0	0.7815	0.7449	0.8136	**0.8172**

| 2689 | 01563200 | 2482.9 | 0.5703 | 0.6497 | **0.7831** | 0.7773 |
| 4809 | 01563500 | 5212.8 | 0.8024 | 0.7563 | **0.857** | 0.8546 |

509

510 The above comparisons informed us of the favorable and unfavorable ranges of applicability for our

511 workflow: the differentiable model found competitive advantages for stem rivers with catchments

512 greater than 2,000 km^2, but may run into issues for scales smaller than the smallest runoff-producing

513 unit (HUC10, around 200 km^2). The issues for the smallest basins could be attributed to the procedure

514 that transfers mass from subbasin to regular grids on the river network, which should be improved in

515 future work. As a result, the smallest headwater basins are best to be directly simulated by the uniform

516 LSTM models. Also, smaller runoff-generating units could be used in the future to mitigate this issue.

517 The advantages of the differentiable routing model over the uniform LSTM for larger basins were due to

518 resolving the heterogeneity in rainfall and basin static attributes as well as better representing routing.

519 The uniform LSTM can internally represent some flow lags but it appears less effective as basin size

520 increases.

521

522 The results imply that the advantages will increase for even larger basins, where currently LSTM does

523 not apply well, along with basins where rainfall heterogeneity makes a big difference. The JRB is situated

524 in the northeastern part of the CONUS; many other regions may exhibit more prominent effects of

525 heterogeneity. For example, past studies have always found it difficult to simulate large basins on the

526 northern and central Great Plains (Feng et al., 2020; Martinez & Gupta, 2010), potentially due to

527 spatially-concentrated rainfall and runoff generation (Fang & Shen, 2017). Also, in the mountainous

528 areas of the CONUS Northwest and Southeast, orographic precipitation could have significant spatial

529 concentration. We hypothesize applying models to smaller basins and incorporating the routing scheme

530 will allow these regions to be better modeled.

531

532 As expected, the training periods selected can exert an influence on the model, but as long as we used

533 reasonable training periods, the results were acceptable. When the scheme was trained on eight-week

534 periods from different years, it generated somewhat different but mostly functional parameterizations

535 (Figure A2 in the Appendix), unless it was trained in some unreasonable training periods where the

536 LSTM had drastic differences from the observed outflows (Table 3). The maximum achievable NSEs for

537 the years of 2001, 2005, 2007, and 2008 were 0.857, 0.87, 0.827, and 0.787, respectively, with all

538   models outperforming Q` NSE values for their respective periods (Table A3 in the Appendix). We found

539   that if the models were trained on other periods (2001a, 2001b, 2005b, 2007a), the test NSEs were

540   mostly decent, and at least not drastically worse. However, choosing 2007b or 2008a led to notably

541   inferior results (Figure 6b-e). Examining the characteristics of the different training periods, we see that

542   the problematic training periods did not contain full flood rise and recession phases (Figure 6a & 6b). As

543   a result, 2007b and 2008a as training periods led to either the lowest or the highest n values and also

544   had relatively low NSE values (Figure A2 in the Appendix). Similarly, training period 2005a gave relatively

545   large n values which also resulted in suboptimal (although still decent) results in all the years. Hence, we

546   need to pick periods that (i) contain full flood rise and recession phases; and (ii) have high runoff NSEs.

547   In addition, even though the routing simulation can be improved by short training periods, the spread of

548   estimated n again shows that the identification of n via small training periods can be difficult. Future

549   work could employ longer training periods to compromise across different periods and obtain broadly-

550   performant parameterization. However, another possibility is that n itself can vary over time, which

551   would be an orthodoxy but not unthinkable idea.

552

553

554

555   *Table 3. The NSE values correspond to testing differentiable models on different test years. Bold font*

556   *indicates the highest NSE, while underlined metrics indicate the lowest (noticeably worse than obtained*

557   *from other periods) for the testing period.*

558

Testing Period	Training Period							
	2001a 02/01-3/29	2001b 11/01-12/26	2005a 02/01-3/29	2005b 11/01-12/26	2007a 02/01-3/29	2007b 11/01-12/26	2008a 02/01-3/29	2008b 11/01-12/26
2001	**0.857**	0.845	0.850	0.853	0.857	0.831	<u>0.782</u>	0.856
2005	0.797	0.828	0.843	**0.870**	0.816	<u>0.713</u>	0.785	0.785
2007	0.815	0.812	0.821	**0.827**	0.819	0.774	<u>0.753</u>	0.813
2008	0.643	0.715	0.723	0.762	0.676	<u>0.534</u>	**0.787**	0.623
Average	0.778	0.800	0.809	**0.828**	0.792	<u>0.713</u>	0.777	0.769

559
560

561

562   *Figure 6: (a) Two training periods: 2005 and 2007a. The former contains a full rising-recession cycle while*

563   *the latter does not have a complete cycle for training, thus leading to larger errors during test. The solid*

564   *line indicates the training of Model 2005b while the dashed line indicates Model 2007b during the time*

565   *period of 11/01-12/27 during the years 2005 and 2007, respectively. (b-c) Test periods for these two*

566   *models: (b) 2001, (c) 2005, (d) 2007, and (e) 2008. For (b-e) the solid line indicates discharge while the*

567   *dashed line indicates percent error of each model's output compared with the observations.*

568

569   *3.4. Further discussion*

570   Although the estimated *n* values were both functional for routing streamflow and physically meaningful,

571   the results suggest the downstream discharge only poses a moderate constraint on the *n* values, and

572   short training periods may not be sufficient to identify the true *n* values. Hence, while our procedure can

573   obtain *n* parameterization performant for long-term simulations, we do not claim that the procedure

574   retrieved the "true" *n* parameterization. Especially considering there are many input variables to the NN

575   that covary in space, it may be difficult to disentangle causation from correlation. Due to the lack of

576   ground truth for *n* in the real-data case, we leave this evaluation for future effort as we compile more

577   measurement data. Recall that we were able to retrieve the overall pattern of *n* in the synthetic

578   experiments but faced large uncertainties in some areas of the parameter space. This is attributed to the

579   numerous degrees of freedom (a high-dimensional input space for the NN, influencing many reaches)

580   constrained by only one downstream output with a relatively short training period. Nevertheless, this

581   training is valuable because discharge data can be widely available, and we will be able to employ it in

582   conjunction with other constraints, e.g., scattered measurements or expert-specified relationships.

583

584   Regarding other potential recoverable parameters, we suspect the dimensionless MC inflow/outflow

585   weighing parameter X, which indicates the shape of the assumed flood prism, cannot be identified for

586   the same reason as q --- the geometries of the channel do not impact flow rates in a meaningful way.

587   Future work could investigate if learning it produces any benefit. Similarly, linear channel coefficient *p*

588   values were also never recoverable in single parameter tests and decreased resulting NSE values when

589   used as a tunable parameter. Thus, we did not include it in this study. In addition, we hypothesize using

590   more complex MC formula, e.g., the nonlinear form of the Cunge equation (the celerity is defined as

591   *dQ/dA),* which might add to numerical challenges for large-scale simulations, would lead to different *n*

592   values, as the recovered values are inherently linked to the inverse model employed.

593

594   Here we employed a static parameterization scheme for *n*, following the conventional approach.

595   However, the framework allows for the use of a dynamic *n* (likely dependent on Q). It is not clear if we

596   must use a static parameterization as done conventionally, as some previous studies have found a

597   dynamic *n* to offer better results (Ye et al., 2018). In the future, it will be interesting to see if a dynamical

598   *n* parameterization could significantly impact the routing results. On another note, we chose an eight-

599   week time period as our training length as a probe to assess the required training duration and selection

600   criteria for such periods. We trained eight different models (Section 3.3) on different time periods and

601   showed that the choice of training period timing, and LSTM performance for the inputs played

602   important roles. Future effort should include longer training periods to most robustly estimate the

603   parameters.

604

605   When investigating the impact of multiple gages, rather than a single downstream-most gage (in model

606   loss calculation and parameter updates), results were very similar in terms of NSE score and recovered

607   Manning's *n* parameters. We believe this may be because the JRB is a relatively small river network, so

608   internal gage observations are highly correlated in discharge volume (m^3/s) and fluctuation (storm event

609   timing). Adding more gages could be useful if flows in different parts of the basin need to be accurately

610   reported, but may be less important if only the downstream gage is of concern.

611

612   Our approach, akin to a classical routing scheme, is modular --- the trained weights of the NN that

613   generates *n* are not tied to a particular runoff model. Our work can be coupled to traditional models in

614   multiple ways. Firstly, the trained network can be used to generate *n* for traditional models. In this way,

615   no change is required on the part of the traditional models. Secondly, the neural network and the

616   trained weights can be ported to other programming environments like Fortran. This makes it possible

617   to use the trained parameterizations as a built-in module in continental-scale models (Greuell et al.,

618   2015; Johnson et al., 2019; Regan et al., 2018). An alternative approach is to lump both the routing and

619   runoff simulations into one problem and optimize them together, as demonstrated in some other

620   studies (Jia et al., 2021). In our case, this would mean that we would train both the runoff LSTM and the

621   routing module together. In many big-data DL case studies, lumped models tend to have higher

622   performance compared to a workflow that separates the tasks into multiple minor tasks. However, in

623   our case here, this leads to coadaptation concerns. Moreover, our approach is modular so it can be

624   easily coupled to other runoff models, e.g., a non-differentiable traditional model, or a differentiable

625   one (Feng, Beck, et al., 2022; Feng, Liu, et al., 2022).

626

627   **4. Conclusions**

628   In this work, we used a combination of a pre-trained LSTM rainfall-runoff model and Muskingum-Cunge

629   routing to create a learnable routing model, or, from the perspective of machine learning, a physics-

630   informed graph neural network. This model predicts streamflow in stem rivers and learn river

631   parameters throughout a river network, which is urgently needed to improve the next-generation large-

632   scale hydrologic models. Because our framework is built on physical principles and estimates widely-

633   used *n* values, it can be easily ported to work with other models. For example, the trained NN and the

634   weights can be loaded into Fortran or C programs to support traditional hydrologic models or routing

635   schemes, e.g. (H. Li et al., 2013; Mizukami et al., 2016). Our synthetic experiments recovered the overall

636   spatial pattern of *n* with moderate accuracy but could not recover the channel cross-sectional geometry

637   parameter (q). Furthermore, our synthetic experiments yielded promising results in recovering synthetic

638   n and drainage area relationships, implying there is potential to learn reach-scale physics in the river

639   network using differentiable modeling.

640

641   With the real-world data, short-term training periods of downstream hydrographs can produce n

642   parameterization that improve long-term routing results, but may be insufficient to constrain the n

643   values more precisely than a general spatial pattern. Eight weeks of real-world data produced decent

644   long-term streamflow routing and improved upon approaches that did not use routing, yet training on

645   different periods could result in somewhat different distributions. When looking at the n vs drainage

646   area distribution attained by our trained model against USGS observations, we found that the n values

647   agreed with the literature bounds for the area, but the absolute magnitudes may fluctuate depending

648   on the training period. Besides using longer training periods to obtain n values that compromise across

649   periods, future work should also consider if n should be treated as dynamic in time. Further work can

650   expand this analysis to other basins with different conditions (streams outside of the Ridge and Valley

651   physiographic division of the CONUS) to see if the model can still identify their trends correctly.

652   Reviewing the internal gage NSE scores over a full year of data showed a correlation between drainage

653   area and the relative advantage of our routing scheme, highlighting the impacts of heterogeneity and

654   flow convergence.

655

656

657   **Open Research**

664

665   **Funding Acknowledgements**

668

669

References

671 Aboelyazeed, D., Xu, C., Hoffman, F. M., Jones, A. W., Rackauckas, C., Lawson, K. E., & Shen,

672   C. (2022). A differentiable ecosystem modeling framework for large-scale inverse

673   problems: demonstration with photosynthesis simulations. *Biogeosciences Discussions*.

674   https://doi.org/10.5194/bg-2022-211

675 Adnan, R. M., Petroselli, A., Heddam, S., Santos, C. A. G., & Kisi, O. (2021). Comparison of

676   different methodologies for rainfall–runoff modeling: machine learning vs conceptual

677   approach. *Natural Hazards*, *105*(3), 2987–3011. https://doi.org/10.1007/s11069-020-

678   04438-2

679 Arcement, G. J., & Schneider, V. R. (1989). *Guide for Selecting Manning's Roughness*

680   *Coefficients for Natural Channels and Flood Plains* (Water-Supply Paper No. 2339). U.S.

681   Geological Survey. Retrieved from https://pubs.usgs.gov/wsp/2339/report.pdf

682 Baydin, A. G., Pearlmutter, B. A., Radul, A. A., & Siskind, J. M. (2018). Automatic differentiation

683   in machine learning: A survey. *Journal of Machine Learning Research*, *18*(153), 1–43.

684   Retrieved from http://jmlr.org/papers/v18/17-468.html

685 Candela, A., Noto, L. V., & Aronica, G. (2005). Influence of surface roughness in hydrological

686   response of semiarid catchments. *Journal of Hydrology*, *313*(3), 119–131.

687   https://doi.org/10.1016/j.jhydrol.2005.01.023

688 Carabajal, C. C., & Harding, D. J. (2006). SRTM C-Band and ICEsat laser altimetry elevation

689   comparisons as a function of tree cover and relief. *Photogrammetric Engineering &*

690   *Remote Sensing*, *72*(3), 287–298. https://doi.org/10/ggj69r

691 Chaney, N. W., Minasny, B., Herman, J. D., Nauman, T. W., Brungard, C. W., Morgan, C. L. S.,

692   et al. (2019). POLARIS Soil Properties: 30-m Probabilistic Maps of Soil Properties Over

693   the Contiguous United States. *Water Resources Research*, *55*(4), 2916–2938.

694   https://doi.org/10/ggj68b

695   Cunge, J. A. (1969). On the subject of a flood propagation computation method (Musklngum

696   method). *Journal of Hydraulic Research*, *7*(2), 205–230.

697   https://doi.org/10.1080/00221686909500264

698   Dottori, F., Szewczyk, W., Ciscar, J.-C., Zhao, F., Alfieri, L., Hirabayashi, Y., et al. (2018).

699   Increased human and economic losses from river flooding with anthropogenic warming.

700   *Nature Climate Change*, *8*(9), 781–786. https://doi.org/10.1038/s41558-018-0257-z

701   Douben, K.-J. (2006). Characteristics of river floods and flooding: a global overview, 1985–

702   2003. *Irrigation and Drainage*, *55*(S1), S9–S21. https://doi.org/10.1002/ird.239

703   Duan, S., Ullrich, P., & Shu, L. (2020). Using convolutional neural networks for streamflow

704   projection in California. *Frontiers in Water*, *2*. https://doi.org/10.3389/frwa.2020.00028

705   Falcone, J. A. (2011). GAGES-II: Geospatial Attributes of Gages for Evaluating Streamflow

706   [Data set]. *GAGES-II: Geospatial Attributes of Gages for Evaluating Streamflow*. USGS

707   Unnumbered Series, Reston, VA: U.S. Geological Survey.

708   https://doi.org/10.3133/70046617

709   Fan, W., Ma, Y., Li, Q., He, Y., Zhao, E., Tang, J., & Yin, D. (2019, November 22). Graph neural

710   networks for social recommendation. arXiv. https://doi.org/10.48550/arXiv.1902.07243

711   Fang, K., & Shen, C. (2017). Full-flow-regime storage-streamflow correlation patterns provide

712   insights into hydrologic functioning over the continental US. *Water Resources Research*,

713   *53*(9), 8064–8083. https://doi.org/10.1002/2016WR020283

714   Fang, K., Shen, C., Kifer, D., & Yang, X. (2017). Prolongation of SMAP to spatiotemporally

715   seamless coverage of continental U.S. using a deep learning neural network.

716   *Geophysical Research Letters*, *44*(21), 11,030-11,039.

717   https://doi.org/10.1002/2017gl075619

718   Fang, K., Pan, M., & Shen, C. (2019). The value of SMAP for long-term soil moisture estimation

719   with the help of deep learning. *IEEE Transactions on Geoscience and Remote Sensing*,

720   *57*(4), 2221–2233. https://doi.org/10/gghp3v

721 Feng, D., Fang, K., & Shen, C. (2020). Enhancing streamflow forecast and extracting insights

722   using long-short term memory networks with data integration at continental scales.

723   *Water Resources Research*, *56*(9), e2019WR026793.

724   https://doi.org/10.1029/2019WR026793

725 Feng, D., Liu, J., Lawson, K., & Shen, C. (2022). Differentiable, learnable, regionalized process-

726   based models with multiphysical outputs can approach state-of-the-art hydrologic

727   prediction accuracy. *Water Resources Research*, *58*(10), e2022WR032404.

728   https://doi.org/10.1029/2022WR032404

729 Feng, D., Beck, H., Lawson, K., & Shen, C. (2022). The suitability of differentiable, learnable

730   hydrologic models for ungauged regions and climate change impact assessment.

731   *Hydrology and Earth System Sciences Discussions*, 1–28. https://doi.org/10.5194/hess-

732   2022-245

733 France-Presse, A. (2022, June 19). At least 59 dead and millions stranded as floods devastate

734   India and Bangladesh. *The Guardian*. Retrieved from

735   https://www.theguardian.com/world/2022/jun/18/at-least-18-dead-and-millions-stranded-

736   as-floods-devastate-india-and-bangladesh

737 François, B., Schlef, K. E., Wi, S., & Brown, C. M. (2019). Design considerations for riverine

738   floods in a changing climate – A review. *Journal of Hydrology*, *574*, 557–573.

739   https://doi.org/10.1016/j.jhydrol.2019.04.068

740 Friedl, M., & Sulla-Menashe, D. (2019). MCD12Q1 MODIS/Terra+Aqua Land Cover Type Yearly

741   L3 Global 500m SIN Grid V006 [Data set].

742   https://doi.org/10.5067/MODIS/MCD12Q1.006

743 Getirana, A. C. V., Boone, A., Yamazaki, D., Decharme, B., Papa, F., & Mognard, N. (2012).

744   The Hydrological Modeling and Analysis Platform (HyMAP): Evaluation in the Amazon

745   Basin. *Journal of Hydrometeorology*, *13*(6), 1641–1665. https://doi.org/10/f4jbcx

746   Gleason, C. J. (2015). Hydraulic geometry of natural rivers: A review and future directions.

747   *Progress in Physical Geography*. https://doi.org/10/f7dsqm

748   Greuell, W., Andersson, J. C. M., Donnelly, C., Feyen, L., Gerten, D., Ludwig, F., et al. (2015).

749   Evaluation of five hydrological models across Europe and their suitability for making

750   projections under climate change. *Hydrology and Earth System Sciences Discussions*,

751   *12*(10), 10289–10330. https://doi.org/10.5194/hessd-12-10289-2015

752   He, M., Wu, S., Huang, B., Kang, C., & Gui, F. (2022). Prediction of total nitrogen and

753   phosphorus in surface water by deep learning methods based on multi-scale feature

754   extraction. *Water*, *14*(10), 1643. https://doi.org/10.3390/w14101643

755   Hochreiter, S. (1998). The vanishing gradient problem during learning recurrent neural nets and

756   problem solutions. *International Journal of Uncertainty, Fuzziness and Knowledge-*

757   *Based Systems*, *06*(02), 107–116. https://doi.org/10.1142/S0218488598000094

758   Hochreiter, S., & Schmidhuber, J. (1997). Long Short-Term Memory. *Neural Computation*, *9*(8),

759   1735–1780. https://doi.org/10.1162/neco.1997.9.8.1735

760   HorizonSystems. (2016). NHDPlus version 2 [Data set]. Retrieved from http://www.horizon-

761   systems.com/nhdplus/NHDplusV2_home.php

762   Hrnjica, B., Mehr, A. D., Jakupović, E., Crnkić, A., & Hasanagić, R. (2021). Application of deep

763   learning neural networks for nitrate prediction in the Klokot River, Bosnia and

764   Herzegovina. In *2021 7th International Conference on Control, Instrumentation and*

765   *Automation (ICCIA)* (pp. 1–6). https://doi.org/10.1109/ICCIA52082.2021.9403565

766   Huscroft, J., Gleeson, T., Hartmann, J., & Börker, J. (2018). Compiling and mapping global

767   permeability of the unconsolidated and consolidated Earth: GLobal HYdrogeology MaPS

768   2.0 (GLHYMPS 2.0). *Geophysical Research Letters*, *45*(4), 1897–1904.

769   https://doi.org/10.1002/2017GL075860

770   International Panel on Climate Change (IPCC). (2012). *Managing the Risks of Extreme Events*

771   *and Disasters to Advance Climate Change Adaptation* (p. 582). Retrieved from

772   https://www.ipcc.ch/report/managing-the-risks-of-extreme-events-and-disasters-to-

773   advance-climate-change-adaptation/

774   Ji, X., Lesack, L., Melack, J. M., Wang, S., Riley, W. J., & Shen, C. (2019). Seasonal and inter-

775   annual patterns and controls of hydrological fluxes in an Amazon floodplain lake with a

776   surface-subsurface processes model. *Water Resources Research*, *55*(4), 3056–3075.

777   https://doi.org/10/gghp4s

778   Jia, X., Zwart, J., Sadler, J., Appling, A., Oliver, S., Markstrom, S., et al. (2021). Physics-Guided

779   Recurrent Graph Model for Predicting Flow and Temperature in River Networks. In

780   *Proceedings of the 2021 SIAM International Conference on Data Mining (SDM)* (pp.

781   612–620). Society for Industrial and Applied Mathematics.

782   https://doi.org/10.1137/1.9781611976700.69

783   Johnson, J. M., Munasinghe, D., Eyelade, D., & Cohen, S. (2019). An integrated evaluation of

784   the National Water Model (NWM)–Height Above Nearest Drainage (HAND) flood

785   mapping methodology. *Natural Hazards and Earth System Sciences*, *19*(11), 2405–

786   2420. https://doi.org/10.5194/nhess-19-2405-2019

787   Kalyanapu, A. J., Burian, S. J., & McPherson, T. N. (2009). Effect of land use-based surface

788   roughness on hydrologic model output. *Journal of Spatial Hydrology*, *9*(2), 51–71.

789   Retrieved from https://scholarsarchive.byu.edu/josh/vol9/iss2/2

790   Khorashadi Zadeh, F., Nossent, J., Sarrazin, F., Pianosi, F., van Griensven, A., Wagener, T., &

791   Bauwens, W. (2017). Comparison of variance-based and moment-independent global

792   sensitivity analysis approaches by application to the SWAT model. *Environmental*

793   *Modelling & Software*, *91*, 210–222. https://doi.org/10.1016/j.envsoft.2017.02.001

794   Kingma, D. P., & Ba, J. (2017, January 29). Adam: A method for stochastic optimization. arXiv.

795   https://doi.org/10.48550/arXiv.1412.6980

796   Koks, E. E., & Thissen, M. (2016). A multiregional impact assessment model for disaster

797   analysis. *Economic Systems Research*, *28*(4), 429–449.

798   https://doi.org/10.1080/09535314.2016.1232701

799   Kratzert, F., Klotz, D., Shalev, G., Klambauer, G., Hochreiter, S., & Nearing, G. (2019). Towards

800   learning universal, regional, and local hydrological behaviors via machine learning

801   applied to large-sample datasets. *Hydrology and Earth System Sciences*, *23*(12), 5089–

802   5110. https://doi.org/10.5194/hess-23-5089-2019

803   Leopold, L. B., & Maddock, T. Jr. (1953). The hydraulic geometry of stream channels and some

804   physiographic implications. *USGS Professional Paper*, *252*. https://doi.org/10/ggj7hw

805   Leshno, M., Lin, V. Ya., Pinkus, A., & Schocken, S. (1993). Multilayer feedforward networks with

806   a nonpolynomial activation function can approximate any function. *Neural Networks*,

807   *6*(6), 861–867. https://doi.org/10/bjjdg2

808   Li, H., Wigmosta, M. S., Wu, H., Huang, M., Ke, Y., Coleman, A. M., & Leung, L. R. (2013). A

809   physically based runoff routing model for land surface and earth system models. *Journal

810   of Hydrometeorology*, *14*(3), 808–828. https://doi.org/10/ggj7ph

811   Li, H.-Y., Tan, Z., Ma, H., Zhu, Z., Abeshu, G. W., Zhu, S., et al. (2022). A new large-scale

812   suspended sediment model and its application over the United States. *Hydrology and

813   Earth System Sciences*, *26*(3), 665–688. https://doi.org/10.5194/hess-26-665-2022

814   Lin, G.-Y., Chen, H.-W., Chen, B.-J., & Yang, Y.-C. (2022). Characterization of temporal PM2.5,

815   nitrate, and sulfate using deep learning techniques. *Atmospheric Pollution Research*,

816   *13*(1), 101260. https://doi.org/10.1016/j.apr.2021.101260

817   Liu, J., Rahmani, F., Lawson, K., & Shen, C. (2022). A multiscale deep learning model for soil

818   moisture integrating satellite and in situ data. *Geophysical Research Letters*, *49*(7),

819   e2021GL096847. https://doi.org/10.1029/2021GL096847

820   Liu, L., Ao, T., Zhou, L., Takeuchi, K., Gusyev, M., Zhang, X., et al. (2022). Comprehensive

821   evaluation of parameter importance and optimization based on the integrated sensitivity

822   analysis system: A case study of the BTOP model in the upper Min River Basin, China.

823   *Journal of Hydrology*, *610*, 127819. https://doi.org/10.1016/j.jhydrol.2022.127819

824   Martinez, G. F., & Gupta, H. V. (2010). Toward improved identification of hydrological models: A

825   diagnostic evaluation of the "abcd" monthly water balance model for the conterminous

826   United States. *Water Resources Research*, *46*(8).

827   https://doi.org/10.1029/2009WR008294

828   Mays, L. W. (2010). *Water Resources Engineering* (2nd edition). Tempe, AZ: Wiley.

829   Mays, L. W. (2019). *Water Resources Engineering* (3rd edition). Tempe, AZ: Wiley. Retrieved

830   from https://www.wiley.com/en-us/Water+Resources+Engineering%2C+3rd+Edition-p-

831   9781119493167

832   Meyal, A. Y., Versteeg, R., Alper, E., Johnson, D., Rodzianko, A., Franklin, M., & Wainwright, H.

833   (2020). Automated cloud based long short-term memory neural network based SWE

834   prediction. *Frontiers in Water*, *2*. https://doi.org/10.3389/frwa.2020.574917

835   Mizukami, N., Clark, M. P., Sampson, K., Nijssen, B., Mao, Y., McMillan, H., et al. (2016).

836   mizuRoute version 1: A river network routing tool for a continental domain water

837   resources applications. *Geoscientific Model Development*, *9*(6), 2223–2238.

838   https://doi.org/10.5194/gmd-9-2223-2016

839   Moore, R. B., & Dewald, T. G. (2016). The road to NHDPlus — Advancements in digital stream

840   networks and associated catchments. *JAWRA Journal of the American Water*

841   *Resources Association*, *52*(4), 890–900. https://doi.org/10.1111/1752-1688.12389

842   Nash, J. E., & Sutcliffe, J. V. (1970). River flow forecasting through conceptual models part I —

843   A discussion of principles. *Journal of Hydrology*, *10*(3), 282–290.

844   https://doi.org/10/fbg9tm

845   O, S., & Orth, R. (2021). Global soil moisture data derived through machine learning trained with

846   in-situ measurements. *Scientific Data*, *8*(1), 170. https://doi.org/10.1038/s41597-021-

847   00964-1

848   Ouyang, W., Lawson, K., Feng, D., Ye, L., Zhang, C., & Shen, C. (2021). Continental-scale

849   streamflow modeling of basins with reservoirs: Towards a coherent deep-learning-based

850   strategy. *Journal of Hydrology*, *599*, 126455.

851   https://doi.org/10.1016/j.jhydrol.2021.126455

852   Pan, M., & Wood, E. F. (2013). Inverse streamflow routing. *Hydrology and Earth System*

853   *Sciences*, *17*(11), 4577–4588. https://doi.org/10/f5k6nq

854   Prein, A. F., Rasmussen, R. M., Ikeda, K., Liu, C., Clark, M. P., & Holland, G. J. (2017). The

855   future intensification of hourly precipitation extremes. *Nature Climate Change*, *7*(1), 48–

856   52. https://doi.org/10.1038/nclimate3168

857   Rahmani, F., Shen, C., Oliver, S., Lawson, K., & Appling, A. (2021). Deep learning approaches

858   for improving prediction of daily stream temperature in data-scarce, unmonitored, and

859   dammed basins. *Hydrological Processes*, *35*(11), e14400.

860   https://doi.org/10.1002/hyp.14400

861   Rahmani, F., Lawson, K., Ouyang, W., Appling, A., Oliver, S., & Shen, C. (2021). Exploring the

862   exceptional performance of a deep learning stream temperature model and the value of

863   streamflow data. *Environmental Research Letters*. https://doi.org/10.1088/1748-

864   9326/abd501

865   Regan, R. S., Markstrom, S. L., Hay, L. E., Viger, R. J., Norton, P. A., Driscoll, J. M., &

866   LaFontaine, J. H. (2018). *Description of the National Hydrologic Model for use with the*

867   *Precipitation-Runoff Modeling System (PRMS)* (No. 6-B9). *Techniques and Methods*.

868   U.S. Geological Survey. https://doi.org/10.3133/tm6B9

869   Rice, D. (2019, May 28). Mississippi River flood is longest-lasting in over 90 years, since "Great

870   Flood" of 1927. *USA Today*. Retrieved from

871   https://www.usatoday.com/story/news/nation/2019/05/28/mississippi-river-flooding-

872   longest-lasting-since-great-flood-1927/1261049001/

873   Saha, G. K., Rahmani, F., Shen, C., Li, L., & Cibin, R. (2023). A deep learning-based novel

874   approach to generate continuous daily stream nitrate concentration for nitrate data-

875   sparse watersheds. *Science of The Total Environment*, *878*, 162930.

876   https://doi.org/10.1016/j.scitotenv.2023.162930

877   Shen, C., & Lawson, K. (2021). Applications of Deep Learning in Hydrology. In *Deep Learning*

878   *for the Earth Sciences* (pp. 283–297). John Wiley & Sons, Ltd.

879   https://doi.org/10.1002/9781119646181.ch19

880   Shen, C., & Phanikumar, M. S. (2010). A process-based, distributed hydrologic model based on

881   a large-scale method for surface–subsurface coupling. *Advances in Water Resources*,

882   *33*(12), 1524–1541. https://doi.org/10/c4r8k5

883   Shen, C., Niu, J., & Phanikumar, M. S. (2013). Evaluating controls on coupled hydrologic and

884   vegetation dynamics in a humid continental climate watershed using a subsurface - land

885   surface processes model. *Water Resources Research*, *49*(5), 2552–2572.

886   https://doi.org/10/f5gcrx

887   Shen, C., Niu, J., & Fang, K. (2014). Quantifying the effects of data integration algorithms on the

888   outcomes of a subsurface–land surface processes model. *Environmental Modelling &*

889   *Software*, *59*, 146–161. https://doi.org/10/ggj7mp

890   Shen, C., Riley, W. J., Smithgall, K. M., Melack, J. M., & Fang, K. (2016). The fan of influence of

891   streams and channel feedbacks to simulated land surface water and carbon dynamics.

892   *Water Resources Research*, *52*(2), 880–902. https://doi.org/10/f8gppj

893   Shen, C., Chen, X., & Laloy, E. (2021). Editorial: Broadening the use of machine learning in

894   hydrology. *Frontiers in Water*, *3*. https://doi.org/10.3389/frwa.2021.681023

895   Shen, C., Fang, K., Feng, D., & Bindas, T. (2021). mhpi/hydroDL: MHPI-hydroDL [Data set].

896   Zenodo. https://doi.org/10.5281/zenodo.5015120

897 Sun, A. Y., Jiang, P., Mudunuru, M. K., & Chen, X. (2021). Explore spatio-temporal learning of

898   large sample hydrology using graph neural networks. *Water Resources Research*,

899   *57*(12), e2021WR030394. https://doi.org/10.1029/2021WR030394

900 Sun, A. Y., Jiang, P., Yang, Z.-L., Xie, Y., & Chen, X. (2022). A graph neural network approach

901   to basin-scale river network learning: The role of physics-based connectivity and data

902   fusion. *Hydrology and Earth System Sciences Discussions*. https://doi.org/10.5194/hess-

903   2022-111

904 Tsai, W.-P., Feng, D., Pan, M., Beck, H., Lawson, K., Yang, Y., et al. (2021). From calibration to

905   parameter learning: Harnessing the scaling effects of big data in geoscientific modeling.

906   *Nature Communications*, *12*(1), 5988. https://doi.org/10.1038/s41467-021-26107-z

907 US Army Corps of Engineers. (2018). National Inventory of Dams (NID) [Data set]. Retrieved

908   from https://nid.sec.usace.army.mil/

909 USGS ScienceBase-Catalog. (2022). National Elevation Dataset (NED). Retrieved September

910   13, 2022, from https://www.sciencebase.gov/catalog/item/4fcf8fd4e4b0c7fe80e81504

911 Virtanen, P., Gommers, R., Oliphant, T. E., Haberland, M., Reddy, T., Cournapeau, D., et al.

912   (2020). SciPy 1.0: fundamental algorithms for scientific computing in Python. *Nature*

913   *Methods*, *17*(3), 261–272. https://doi.org/10.1038/s41592-019-0686-2

914 Winsemius, H. C., Aerts, J. C. J. H., van Beek, L. P. H., Bierkens, M. F. P., Bouwman, A.,

915   Jongman, B., et al. (2016). Global drivers of future river flood risk. *Nature Climate*

916   *Change*, *6*(4), 381–385. https://doi.org/10.1038/nclimate2893

917 Wunsch, A., Liesch, T., & Broda, S. (2022). Deep learning shows declining groundwater levels

918   in Germany until 2100 due to climate change. *Nature Communications*, *13*(1), 1221.

919   https://doi.org/10.1038/s41467-022-28770-2

920 Xia, Y., Mitchell, K., Ek, M., Sheffield, J., Cosgrove, B., Wood, E., et al. (2009). NLDAS Primary

921   Forcing Data L4 Hourly 0.125 x 0.125 degree V002 (NLDAS_FORA0125_H) [Data set].

922   Goddard Earth Sciences Data and Information Services Center (GES DISC).

923   https://doi.org/10.5067/6J5LHHOHZHN4

924 Xia, Y., Mitchell, K., Ek, M., Sheffield, J., Cosgrove, B., Wood, E., et al. (2012). Continental-

925   scale water and energy flux analysis and validation for the North American Land Data

926   Assimilation System project phase 2 (NLDAS-2): 1. Intercomparison and application of

927   model products. *Journal of Geophysical Research: Atmospheres*, *117*(D3).

928   https://doi.org/10.1029/2011JD016048

929 Xiang, Z., Yan, J., & Demir, I. (2020). A rainfall-runoff model with LSTM-based sequence-to-

930   sequence learning. *Water Resources Research*, *56*(1), e2019WR025326.

931   https://doi.org/10.1029/2019WR025326

932 Ye, A., Zhou, Z., You, J., Ma, F., & Duan, Q. (2018). Dynamic Manning's roughness coefficients

933   for hydrological modelling in basins. *Hydrology Research*, *49*(5), 1379–1395.

934   https://doi.org/10.2166/nh.2018.175

935 Zhi, W., Feng, D., Tsai, W.-P., Sterle, G., Harpold, A., Shen, C., & Li, L. (2021). From

936   hydrometeorology to river water quality: Can a deep learning model predict dissolved

937   oxygen at the continental scale? *Environmental Science & Technology*, *55*(4), 2357–

938   2368. https://doi.org/10.1021/acs.est.0c06783

939 Zhu, F., Li, X., Qin, J., Yang, K., Cuo, L., Tang, W., & Shen, C. (2021). Integration of

940   multisource data to estimate downward longwave radiation based on deep neural

941   networks. *IEEE Transactions on Geoscience and Remote Sensing*, 1–15.

942   https://doi.org/10.1109/TGRS.2021.3094321
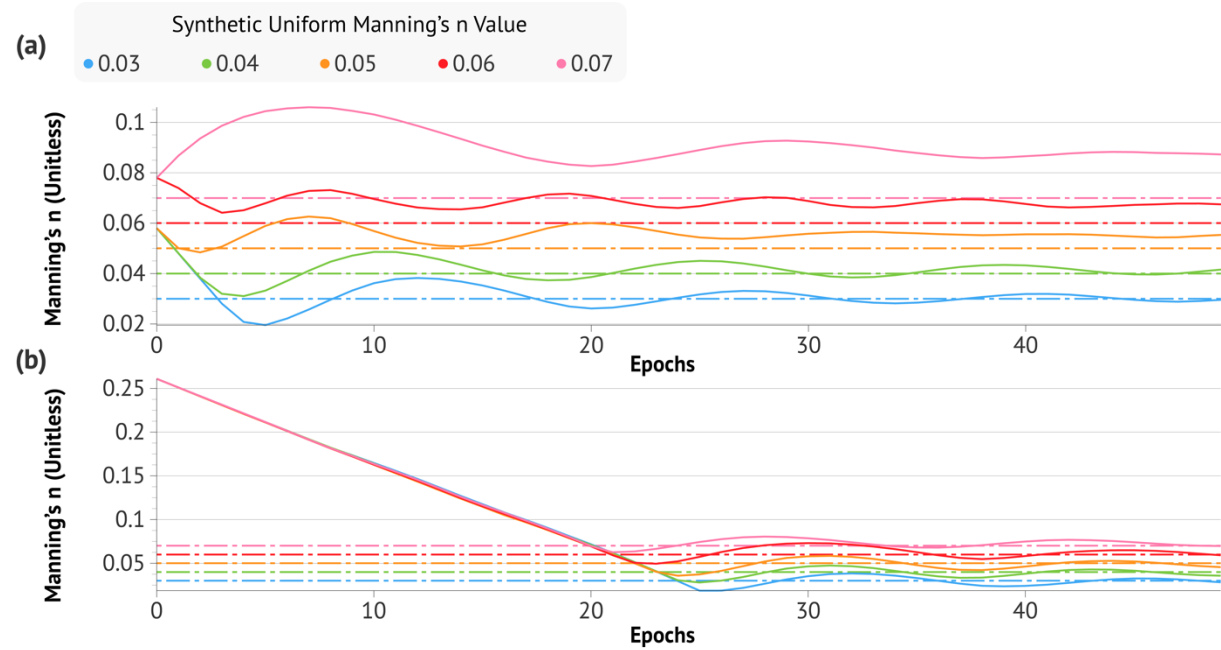
943

944 **Appendix**

945
946

947 Figure A1: The synthetic parameter recovery of Manning's *n* after each epoch run, with each colored line

948 representing a different recovered value. (a) The initial value of *n* is set to 0.068 (b) the initial value of *n*
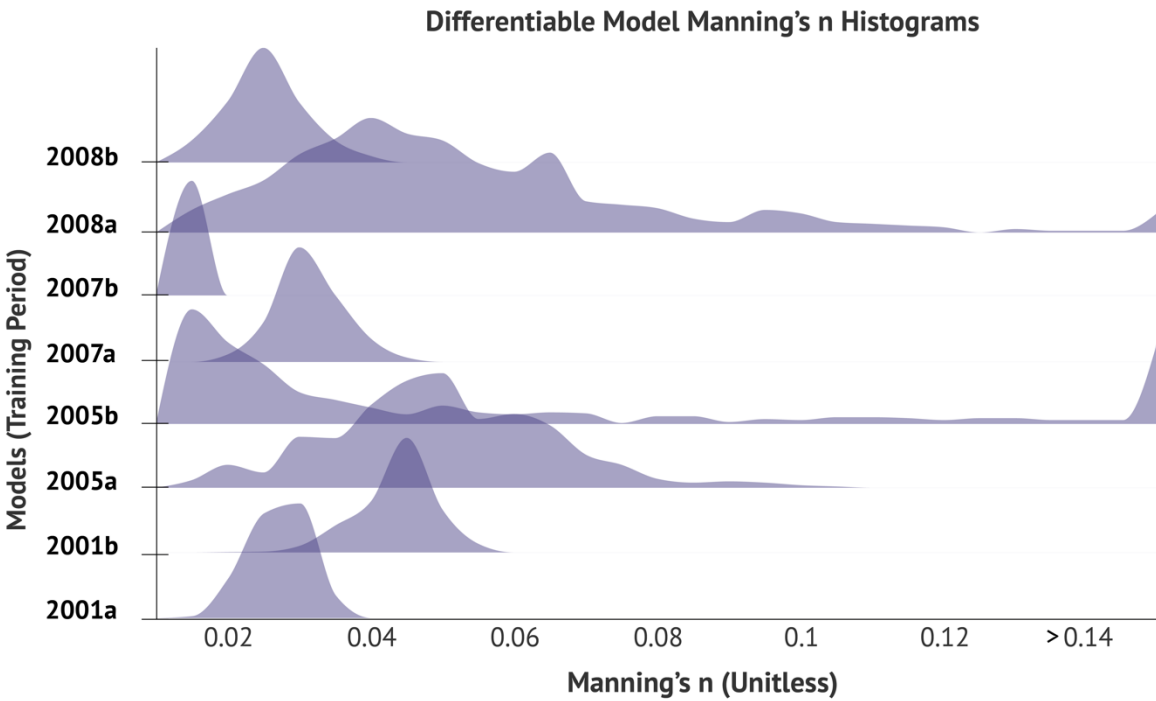
949 is set to 0.271

950

951

952 Figure A2: Histograms visualizing the frequency, and variability, of Manning's *n* values for all river

953 reaches (582 total) for all eight GNN models. The lower bound is 0.01, while the upper bound contains

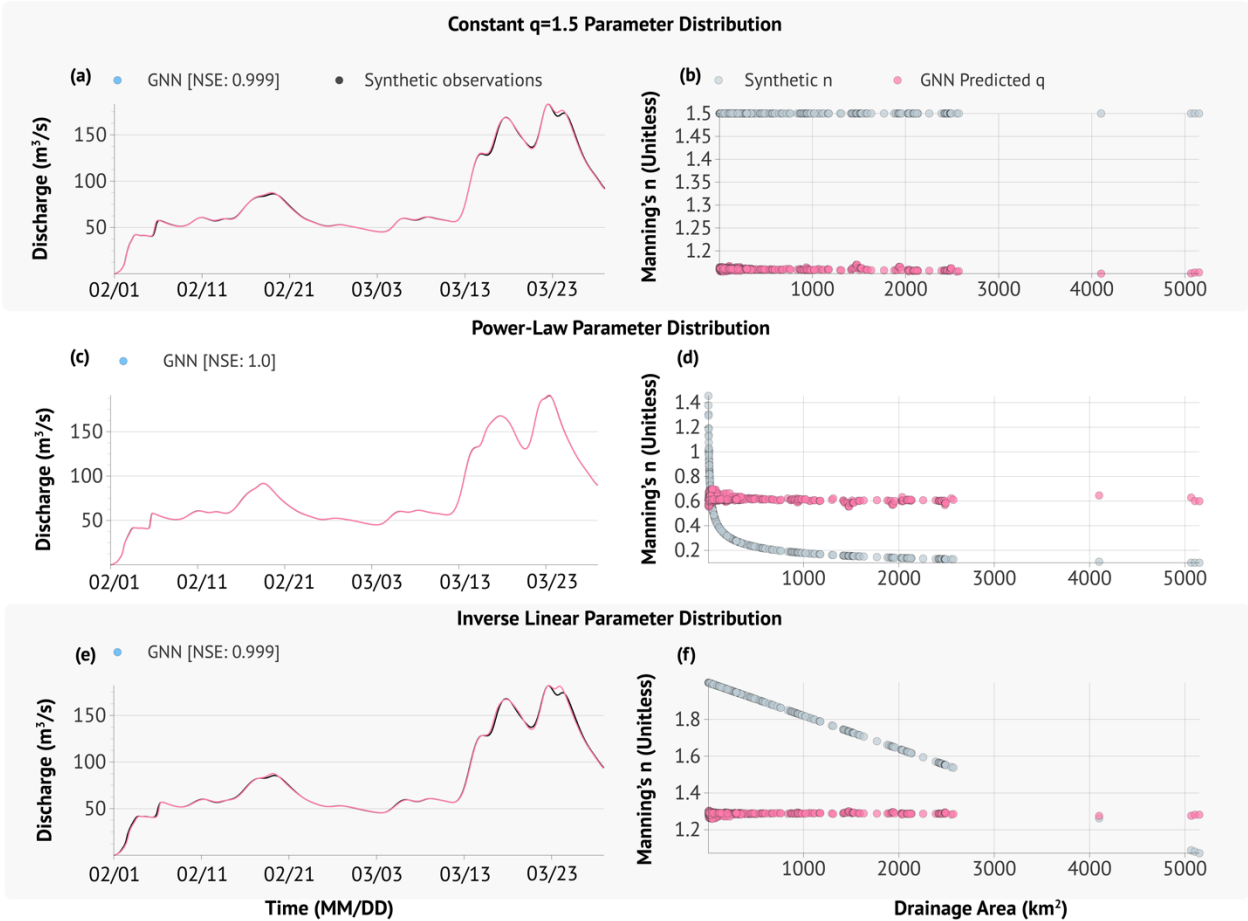954 all Manning's *n* values >0.14.

955

956

957 Figure A3: Results from *q* parameter recovery experiments. We tried to recover both constant and

958 distributed parameters, but were unable to ever recover the synthetic truth.

959

960 Table A1: The attributes and forcings used by the pre-trained LSTM to predict streamflow. Links to the
961 data can be found below the table

Attribute/Meteorological Forcing	Unit	Dataset	Citation
Mean Elevation	m	SRTMGL1	(Carabajal & Harding, 2006)
Mean Slope	unitless	SRTMGL1	(Carabajal & Harding, 2006)

Basin Area	km^2	SRTMGL1	(Carabajal & Harding, 2006)
Dominant Land Cover	Class	MODIS	(Friedl & Sulla-Menashe, 2019)
Dominant Land Cover Fraction	Percent	MODIS	(Friedl & Sulla-Menashe, 2019)
Forest Fraction	Percent	MODIS	(Friedl & Sulla-Menashe, 2019)
Root Depth (50)	m	MODIS	(Friedl & Sulla-Menashe, 2019)
Soil Depth	m	MODIS	(Friedl & Sulla-Menashe, 2019)
Ksat (0-5)	log$_{10}$(cm/hr)	POLARIS	(Chaney et al., 2019)
Ksat (5-15)	log$_{10}$(cm/hr)	POLARIS	(Chaney et al., 2019)
Theta s (0-5)	m^3/m^3	POLARIS	(Chaney et al., 2019)
Theta s (5-15)	m^3/m^3	POLARIS	(Chaney et al., 2019)
Theta r (5-15)	m^3/m^3	POLARIS	(Chaney et al., 2019)
Ksat average (0-15)	log$_{10}$(cm/hr)	POLARIS	(Chaney et al., 2019)
Ksat e (0-5)	cm/hr	POLARIS	(Chaney et al., 2019)

Ksat e (5-15)	cm/hr	POLARIS	(Chaney et al., 2019)
Ksat average e (0-15)	cm/hr	POLARIS	(Chaney et al., 2019)
Theta average s (0-15)	$e^{m3/m3}$	POLARIS	(Chaney et al., 2019)
Theta average r (0-15)	$e^{m3/m3}$	POLARIS	(Chaney et al., 2019)
Porosity	Percent	GLHYMPS	(Huscroft et al., 2018)
Permeability Permafrost	m^2	GLHYMPS	(Huscroft et al., 2018)
Permeability Permafrost (Raw)	m^2	GLHYMPS	(Huscroft et al., 2018)
Major Number of Dams	Unitless	GAGES-II	(Falcone, 2011)
General Purpose of Dam	Unitless	National Inventory of Dams (NID)	(US Army Corps of Engineers, 2018)
Max of Normal Storage	Acre-ft	National Inventory of Dams (NID)	(US Army Corps of Engineers, 2018)
Standard Deviation of Normal Storage	Unitless	National Inventory of Dams (NID)	(US Army Corps of Engineers, 2018)
Number of dams within river (2009)	Unitless	GAGES-II	(Falcone, 2011)
Normal Storage (2009)	Acre-ft	National Inventory of Dams (NID)	(US Army Corps of Engineers, 2018)
Precipitation hourly total	kg/m^2	NLDAS2	(Xia et al., 2012)
Surface downward longwave radiation	W/m^2	NLDAS2	(Xia et al., 2012)

Surface downward shortwave radiation	W/m^2	NLDAS2	(Xia et al., 2012)
Pressure	Pa	NLDAS2	(Xia et al., 2012)
Air Temperature	K	NLDAS2	(Xia et al., 2012)

962
963 SRTMGL1: https://doi.org/10.14358/PERS.72.3.287
964 MODIS: https://modis.gsfc.nasa.gov/data/dataprod/mod12.php
965 POLARIS: https://doi.org/10.1029/2018WR022797
966 GLHYMPS: https://doi.org/10.5683/SP2/DLGXYO
967 NID: https://nid.usace.army.mil/
968 NLDAS2: https://ldas.gsfc.nasa.gov/nldas/v2/forcing
969
970 Table A2: The constant attributes (c) used by the MLP to predict *n* and *q: n,q = NN(c).*

Attribute	Unit
Reach Width	m
Average-Reach Elevation	m
Slope	m/m
Reach Area	km^2
Total Drainage Area	km^2
Reach Length	m
Sinuosity	m/m
Bank Elevation	m

971
972 Table A3: The Σ Q` ($\tau = 9$) NSE scores for all eight training time periods for the most downstream gage.
973 Since Q` routing is a pure forward simulation using the trained LSTM, we report the NSE values for each
974 period.
975

	Periods							
	2001a	2001b	2005a	2005b	2007a	2007b	2008a	2008b
NSE	0.5958	0.3534	-0.7868	-0.1687	0.6830	0.0558	-0.4297	0.3792